RECEIVED BY TIC NOV 15 197

LBL-9840

Lawrence Berkeley Laboratory

UNIVERSITY OF CALIFORNIA

CHEMICAL BIODYNAMICS DIVISION

MASTER

X-RAY ABSORPTION STUDIES OF GRAPHITE INTERCALATES AND METAL-AMMONIA SOLUTIONS

Alan Spence Robertson
(Ph. D. thesis)

September 1979

Prepared for the U.S. Department of Energy under Contract W-7405-ENG-48

DISTRIBUTION OF THIS DOCUMENT IS UNLIMITED

X-Ray Absorption Studies of Graphite Intercalates and Metal-Ammonia Solutions

Alan Spence Robertson

B.S. (University of Illinois) 1970

Abstract

X-Ray absorption spectroscopy (XAS) has been used to study two different systems in this work. The first system studied is the arsenic fluorocomplexes, including the AsF_5 and AsF_6^- intercalates of graphite. The second system studied is rubidium metal-ammonia solutions.

The features in the region near the onset of the K-shell absorption edge, which has been termed X-Ray Absorption Edge Spectroscopy (XAES), are transitions into the unoccupied molecular orbitals or metallic bands of the element being studied. On the high energy side of the absorption edge, the oscillatory portion of the absorption coefficient, which has been labelled Extended X-Ray Absorption Fine Structure (EXAFS), can be analyzed to provide a local radial distribution function around the element being studied. XAES and EXAFS data provided information about both systems studied in this work.

The As-F distances obtained for AsF_3 and AsF_5 gas are both in excellent agreement with electron diffraction data (within 0.004 Å). A superior measurement which is significantly shorter than the accepted value of the bond distance in an undistorted

DISCLAIMER

DISTRIBUTION OF THIS DOCUMENT IS UNLIMITED

AsF_6^- octahedra is reported. Both the XAES and EXAFS data presented support the hypothesis that the AsF_5 oxidizes graphite upon intercalation to produce AsF_6^- and AsF_3 intercalant species.

Changes in the Rb K-edge features which are consistent with the known properties of Rb-NH_3 are correlated with conductivity and delocalization of the solvated electrons. In the XAES region, intensity and position changes of absorption transitions are explained. In the EXAFS region, the Rb-N bond distance and the relative number of nitrogen atoms in the first shell are measured. XAS has been shown to provide unique information about the nature of the metal-ammonia phase separation, phase transition, and density fluctuations.

A discussion of the data analysis methodology is included. Special attention is paid to the initial preparation of the data for analysis. Positions and intensities of the XAES features are compared. Although several different EXAFS analysis techniques were used, only the superior results which employed calculations of Teo and Lee (J. Am. Chem. Soc. (1979), 101, 2815) are reported.

CONTENTS

CONTENTS i

ACKNOWLEDGEMENTS ii

I. INTRODUCTION 1
A. X-Ray Absorption Spectroscopy 3
B. Graphite Intercalates 5
C. Metal Ammonia Solutions 9
Figure Captions 13
Figures 14
References 17

II. XAS THEORY AND EXPERIMENT 20
A. XAES Theory 20
B. EXAFS Theory 23
C. XAS Experiment 27
Figure Captions 32
Figures 33
References 37

III. XAS DATA ANALYSIS METHODS 39
A. Initial Data Preparation 39
B. XAES Analysis 49
C. EXAFS Analysis 52
Figure Captions 71
Figures 74
References 94

IV. AS K-EDGE XAS EXPERIMENTS 97
A. Sample Preparation and Experiment 97
B. XAES Analysis 103
C. EXAFS Analysis 111
D. Conclusions 123
Tables 131
Figure Captions 144
Figures 147
References 173

V. RB K-EDGE XAS EXPERIMENTS 175
A. Sample Preparation and Experiment 175
B. XAES Analysis 183
C. EXAFS Analysis 190
D. Conclusions 198
Tables 203
Figure Captions 210
Figures 214
References 242

Acknowledgements

The support and encouragement of Dr. Melvin P. Klein during the course of this work are gratefully acknowledged.

The X-Ray absorption data could not have been collected nor analyzed without extensive assistance from Jon Kirby. I was also assisted by Joseph Smith and Barry McQuillan in the analysis of the data.

I would like to thank Professors Juana Acrivos and Neil Bartlett for their collaboration in these experiments.

Timothy Walker, Kevin Hathaway, Al Thompson, Ninon Kafka and Richard Biagioni assisted in the data collection efforts.

J. C. Thompson kindly allowed me to use figures he had prepared for other publications in this work.

Members of Professors Acrivos' and Bartlett's research groups supplied me with samples for use in this research effort.

This work was supported in part by the United States Department of Energy. Synchrotron radiation facilities were provided by the Stanford Synchrotron Radiation Laboratory which is supported by NSF grant DMR-07692-A02.

Chapter I

INTRODUCTION

X-ray absorption spectroscopy (XAS) has been used to study two different systems in this work. The first system studied is the arsenic fluorocomplexes, including the AsF_5 and AsF_6^- intercalates of graphite. The second system studied is rubidium metal-ammonia solutions. Analysis of the arsenic and rubidium XAS spectra has provided a better understanding of the nature of the environment surrounding the arsenic and rubidium atoms.

XAS has recently become a powerful tool for providing local structural and chemical state information about the atom being studied. XAS spectra can be divided into two regions. X-ray absorption edge spectroscopy (XAES) is determined by the chemical state of the atom being studied and the type and arrangement of the nearby ligands. The extended X-ray absorption fine structure (EXAFS) is determined by the distance, number and type of atoms surrounding the atom being studied.

Reports have been published of a planar conductivity in intercalated AsF_5 graphite as high as the conductivity in silver. This has inspired much research on the nature of the intercalated

species and the reason for the high conductivity. This XAS study on intercalated graphite provides information about the local environment around the arsenic atom.

Solutions of alkali metals dissolved in liquid ammonia undergo a metal-insulator phase transition as a function of concentration and temperature. In the neighborhood of a critical point there is a phase separation between the metal and insulator phases. An understanding of the structure of atoms surrounding the rubidium atom is important to a complete description of this system. This XAS study provides a measurement of the density of the rubidium metal in solution as well as information about the local environment around the rubidium atom versus temperature and concentration.

Section A of this chapter provides an introduction to XAS. Sections B and C discuss the nature of the two systems being studied, describe the results of previous studies on these systems and explain what type of information XAS can provide. Section B covers graphite intercalates and Section C covers metal ammonia solutions.

Chapter II summarizes XAS theory and experimental method. Chapter III describes in detail the data analysis methods which extract information from the spectra. Chapters IV and V discuss the experiments performed and results obtained on the graphite intercalates and metal ammonia solutions. The data analysis methods are also reviewed in Chapters IV and V. A copy of the computer programs written for data analysis and an operations

manual explaining their use have not been included due to their excessive length.

A. X-Ray Absorption Spectroscopy

For the two systems studied, XAS has been used to probe the local environment around the arsenic and rubidium sites. A representative As spectrum is shown in Figure I-1. The XAS spectrum is recorded by measuring a sample's attenuation while the energy of a monochromatic X-ray beam is increased. X-ray photons above a characteristic energy will be able to excite the most deeply bound or K-shell electrons of arsenic or rubidium. Near the onset of this excitation, the absorption edge, the electron can be excited into empty molecular orbitals or metallic bands of the material being studied, in addition to the transition into the continuum of outgoing free electrons. The position of this absorption edge, and the intensity and position of the transitions to the empty states in the material, are affected by the absorbing atom's oxidation state or metallic character, the type of surrounding ligands, and the ligand's arrangement around the absorbing atom. This is the XAES region of the spectrum, which is indicated in Figure I-1. The transitions evident here are to empty molecular orbitals of AsF_6^-.

Above the edge there is a gradual decline in the absorption cross-section as the X-ray energy is increased. This transition of electrons to the continuum region where free outgoing electrons exist is modulated by a sinusoidal oscillation in cross-section which has been named EXAFS. The liberated K-shell electron is now

an outgoing free electron which can scatter off nearby atoms. The backscattered electron wave can interfere with the original outgoing wave constructively or destructively. As the energy of the photon is increased, the electron's energy is also increased and its wavelength decreases which leads to a changing interference pattern in the electron's final state wavefunction. This modulates the transition matrix element of the initial absorption process. Thus the X-ray absorption spectrum provides an indirect measurement of the electron interference process. The frequency of this oscillation is proportional to the distance the electron travels or twice the distance to the nearby atoms. The shape of the envelope of the absorption modulation depends on the kind of the backscattering atoms and the temperature dependent thermal motion of the atoms. The size of the modulation depends on the number of backscattering atoms and their distance from the absorbing atoms. The EXAFS region is indicated in Figure I-1. The primary oscillation seen here results from the first shell of six fluorines around the arsenic atom in AsF_6^-.

In addition to the detailed information which can be obtained from the XAES and EXAFS regions of the data, the concentration of the absorbing atom can be obtained from the size of the edge jump in absorption as the characteristic energy for the element of interest is traversed. This quantity is useful in analyzing the rubidium metal-ammonia solutions.

B. Graphite Intercalates

Studies of XAS spectroscopy of various As-F compounds are described in this work. The bulk of the results describe the AsF_5 and AsF_6^- graphite intercalation compounds.

A wide variety of compounds have been synthesized in which substances are diffused into the interlayer spaces or galleries of a compounds such as graphite (1,2) and the layered dichalcogenides (2).

Graphite is the simplest example of a layered lattice. Its structure is shown in Figure I-2a. The carbon bonds in each sheet are 1.42 Å long. The sp^2 hybrid orbitals form bonds with 120° angles in the plane while the remaining p electrons form a resonating π-bonding system. The layers are held together by weak van der Walls forces with a separation distance of 3.35 Å. Weak interlayer interactions are responsible for the formation of electrons and hole bands. Graphite is a semimetal with a planar conductivity $\sigma_a = 2 \times 10^4\ (\Omega cm)^{-1}$ and an anisotropy in conductivity of $\sigma_c/\sigma_a = 3000$. A wide variety of compounds have been intercalated into graphite (1,2,3,4,5,6,7). These have included alkali metals (K, Rb, Cs), halogens (Br_2, Cl_2), metal halides (AsF_5, $FeCl_3$) and acid salts (NO_3^-, HSO_4^-).

Upon intercalation the layers of graphite expand to allow the insertion of the intercalant species into galleries between the host layers. The structure of the graphite planes is largely unaffected by the intercalates. A stage 2 compound is illustrated in Figure I-2b. The crosses represent an intercalant M. The stage

of a compound is defined as the ratio of the number of host layers to the number of guest layers. In many cases, long range order exists in the c-direction such that stages as high or higher than n = 7 can be meaningfully discussed as ordered compounds with every seventh gallery filled.

As an example, AsF_5 graphite has been shown (8) to have c-axis repeat distances of 8.10, 11.40, 14.81, 18.31, and 21.51 Å for stages n = 1, 2, 3, 4, and 5. The structure of the intercalant within the galleries is often ordered with respect to the graphite. Figure I-3 shows the projections of two possible structures MC_8 and MC_6 where M is the intercalant species. First stage compounds of LiC_6 (2) and KC_8 (1,9) are known. In many cases, the guest layers may have a phase in which the intercalant species is a disordered structure or even a two-dimensional liquid.

Salts of graphite such as NO_3^- have been shown by Ubbelohde et al. (10) to be excellent conductors. In addition, K-graphite is an excellent conductor with $\sigma_a = 2 \times 10^5$ and $\sigma_a/\sigma_c = 60$. Donation of electrons to or acceptance of electrons from the carbon layers is one of the factors which contributes to the conductivity of these compounds. Within this context, Vogel et al. (11) expected that planar conductivity σ_a would be large for the intercalants of the strong oxidizers SbF_5 and AsF_5. The reaction $C_n + 3AsF_5 \rightarrow C_n^{7+} + 2AsF_6^- + AsF_3$ could have been expected. The compound $C_{10}AsF_5$ had been made by Selig et al. (12). The planar conductivities in certain materials were found (11) to exceed the conductivity of copper. The stage 2 intercalant, $C_{16}AsF_5$, has a

reported conductivity $\sigma_c = 6 \times 10^5 (\Omega cm)^{-1}$ and an unusually large anisotropy $\sigma_a/\sigma_c = 2 \times 10^6$. Similar results have been reported for SbF_5 graphite (13,14,15). Conductivity measurements for samples with high anisotropy have been described elsewhere (16).

Coworkers of the author synthesized $C_8^+OsF_6^-$, $C_8^+IrF_6^-$, $C_{12}^{++}PtF_6^=$ and $C_8^+AsF_6^-$ (17,18,19). All of these have conductivities similar to C_8AsF_5. X-ray crystallographic studies (17,18), magnetic susceptibility studies (19) and conductivity studies (19) indicated that these intercalants oxidized the graphite in the manner indicated above.

However, the AsF_5 and SbF_5 graphite compounds were interpreted by many to be intercalants of molecular AsF_5 and SbF_5. Wide line fluorine nuclear magnetic resonance (20,21,22) experiments showed only one peak indistinguishable from AsF_5 and AsF_6^-. Some amount of AsF_3 could however be present since chemical exchange of F from AsF_3 to AsF_6^- would be fast enough relative to the chemical shift so that only the average peak would be detected. Mass spectrometry (23) has indicated that AsF_5 was either the intercalant species or immediately created in the process of de-intercalation. Theoretical calculations (24,25) based on optical and thermo-reflectance (14,26,27) indicated that 0.02 to 0.20 electrons per AsF_5 or SbF_5 were withdrawn from the graphite π-orbitals upon intercalation.

The mechanisms which have been proposed to describe the AsF_5 and SbF_5 intercalation for AsF_5 are summarized in equations I.1 to I.3:

$$C_n + AsF_5 \rightleftarrows C_n^{\delta+} + AsF_5^{\delta-} \qquad (I.1)$$

$$C_n + AsF_5 \rightleftarrows C_n^{+} + AsF_5^{-} \qquad (I.2)$$

$$C_n + 3AsF_5 \rightleftarrows C_n^{++} + 2AsF_6^{-} + AsF_3 \qquad (I.3)$$

The measurements reported above suggested that either I.1 or I.2 was correct. The arsenic pentafluoride radical anion proposed by equation I.2 is paramagnetic. In order to explain the diamagnetic nature of graphite AsF_5, the unreported dimer $As_2F_{10}^{=}$ could be proposed. However, if oxidation of the graphite occurs as in equation I.3, AsF_5 would be following a common half reaction of AsF_5 : $2e^- + 3AsF_5 \rightleftarrows 2(AsF_6^-) + AsF_3$.

Equations I.4 and I.5 are examples of two such reactions which have been reported (28,29):

$$3Br_2 + 3AsF_5 \rightarrow 2\ \{(Br_3)^+(AsF_6^-)\} + AsF_3 \qquad (I.4)$$

$$\frac{1}{4}\ S_8 + 3Br_2 + 3AsF_5 \rightarrow 2\ \{(SBr_3) + AsF_6^-\} + AsF_3 \qquad (I.5)$$

Furthermore, Mossbauer studies of graphite SbF_5 (which should be similar to graphite AsF_5) showed the clear presence of Sb^{+5} and Sb^{+3} in a 2 to 1 ratio (30). This is evidence suggesting that equation I.3 is correct, although in reference 30, the Sb^{+3} peaks were attributed to fluorination of the graphite. The belief that the AsF_5 was the intercalant was so strong that the data were

not interpreted in the simplest manner of equation I.3 which is unlikely to occur. Furthermore, AsF_3 gas has been detected in the atmosphere above the graphite (12) and mass spectroscopy has shown the presence of AsF_3 at high temperatures (23). The fluorine nuclear magnetic resonance study could also show one line fairly near the AsF_5 position even if equation I.3 were valid due to fast exchange of F atoms from one As to another.

It is in this context that the XAS spectroscopy on AsF_5 graphite and AsF_6^- graphite was begun. The main hypothesis was that equation I.3 describes the intercalation and de-intercalation process. XAES spectroscopy would enable distinguishing between As^{+3} and As^{+5} due to their different oxidation states. The structural differences of AsF_6^- (octahedral) and AsF_5 (trigonal bi-pyramidal) should also dictate different edge structures. Furthermore, since the bond distances in these three components are different, the EXAFS spectrum should indicate what the intercalant species is. XAS should be an excellent technique for this purpose since the high energy of the x-rays used ($\sim$ 12 keV) dictates that the experiment is not affected by the high conductivity or possible fast exchange of F atoms. Furthermore, XAS is a bulk effect and not a skin or surface effect, as are other measurements.

C. Metal Ammonia Solutions

Alkali, alkaline earth and various rare earth metals dissolve in liquid ammonia. Because their absorption edges are in a useable range, XAS studies of Rb and Rb were done. The bulk of the work

involved Rb-NH_3 solutions.

Concentrated solutions, above 7 MPM (mole per cent metal), have a metallic bronze color and a high electrical conductivity ($10^4 (\Omega cm)^{-1}$). Dilute solutions have a bright blue color and below 10^{-3} MPM behave as electrolytes. Between 1 MPM and 7 MPM these solutions undergo a phase transition from insulator to metal. This transition can be described in terms of present theories of disordered metal systems presented by Mott (31). The present literature on metal ammonia solutions is reviewed by Thompson (32) and by the latest international conference on metal ammonia solutions, Colloque Weyl IV (33).

The metal ion and electron are both solvated in the ammonia solution. The source of the blue color is a broad optical absorption band. It is caused by the cavity which the solvated electron creates (34,35). The solvated electron accounts for nearly all of the conductivity of the solution.

A phase separation region for the transition from metal to insulator exists for most solutions in the temperature region T = 200 - 280 K. The hypothesis here is that the transition in this region is a transition of band crossing or Mott type (36). But a controversy surrounds the nature of the metal insulator transition above the consulute point of the phase diagram.

Mott has proposed (36) a qualitative band theory description of the transition in which the solution is one homogeneous, though disordered, phase, The transition occurs when the product of the mean free path of the electron times its wave vector is of the order of 1.

As in doped semiconductors, the one electron centers are randomly distributed. Two Hubbard bands overlap to give a pseudogap. If the Mott g-ratio described by equation I.6

$$g \equiv N(E_F) \ / \ N_{f.e.} \ (E_F) \qquad (I.6)$$

falls below 1/3, the states in the gap will be localized or in an insulator phase. For values of g above 1/3, the states are delocalized or in a metallic phase. $N(E_F)$ is the density of states at the Fermi level E_F for the sample relative to the density $N_{f.e.}$ obtained from a free electron approximation. Various experimental facts support this qualitative theory (36,37).

Cohen and Jortner (38) have proposed a theory for this region based on the classical percolation theory. In the transition region, they propose that there is a microscopic mixture of two different phases of the solution which coexist. In moving across the transition region, the proportion of these different phases, metal and insulator, changes, leading to the phase transition. They have proposed a detailed theory which is consistent with many experimental results. (38).

XAS studies were performed in order to distinguish these two models. One basic difference is the homogeneous or inhomogeneous nature of the solution. If the Cohen-Jortner theory is corrrect, then the superposition of two different edge structures which change relative proportions would be evident. This would not be the case for the Mott theory. In addition, one would expect to see two different EXAFS patterns around the Rb if two different phases were

in microscopic coexistence.

Finally, the structure of the metal-ammonia solution at any concentration is not known. X-ray scattering has not been successful (39) and neutron scattering data are available only for $Li(ND_3)_4$ (40). Structural data, such as that provided by EXAFS, would aid in the understanding of the metal-ammonia solutions. Theories have been proposed for various concentrations including simple hard sphere approximations (41,41) and metal-ammonia dimers (43). XAS would provide the first direct structural information allowing the structural facets of these models to be compared to experiment.

Figure Captions
Chapter I

I-1 X-Ray absorption spectrum of a representative AsF_6^- salt. Three regions are indicated: Pre-edge, XAES and EXAFS.

I-2 Three-dimensional structure of (a) graphite and (b) a stage-2 graphite intercalate.

I-3 Structure in the ab plane for intercalates with the stoichiometry MC_8 and MC_6. The dashed lines show the unit cell of the graphite layers while the solid lines show the unit cell of the intercalated species.

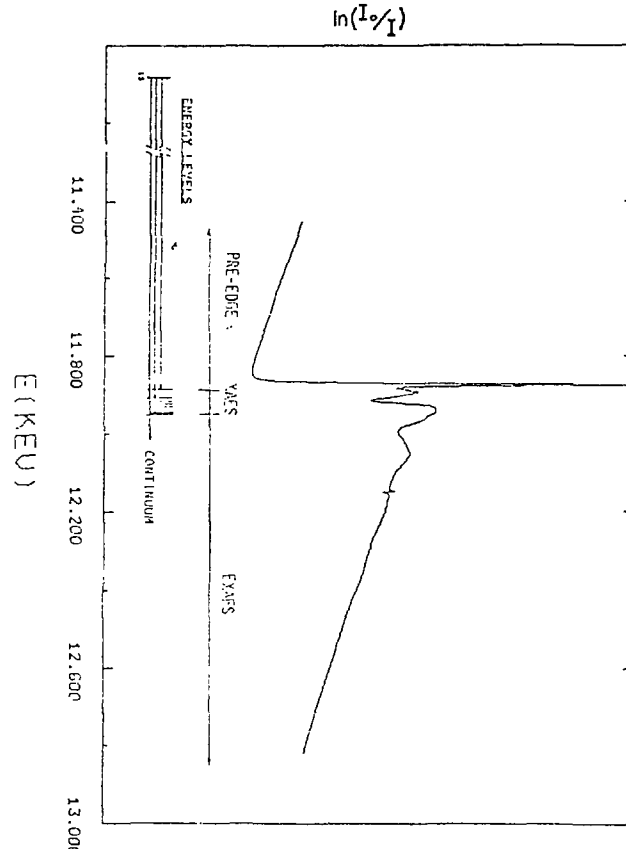
ln(I₀/I)
PRE-EDGE
XANES
EXAFS
ENERGY LEVELS
CONTINUUM
11.400
11.800
12.200
12.600
13.000
E(KEV)

Figure I-1

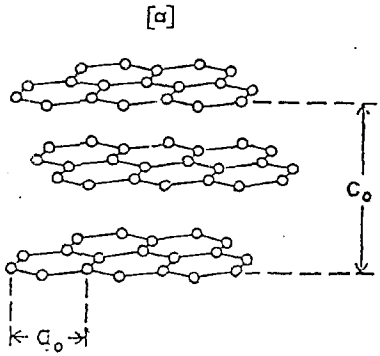

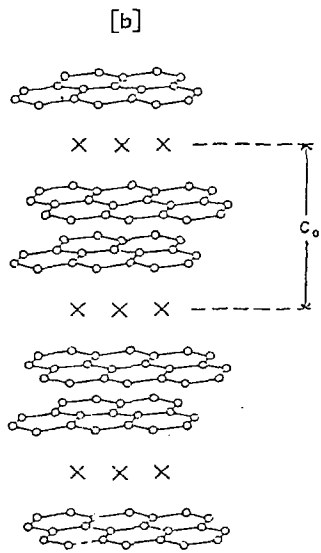

Figure I-2

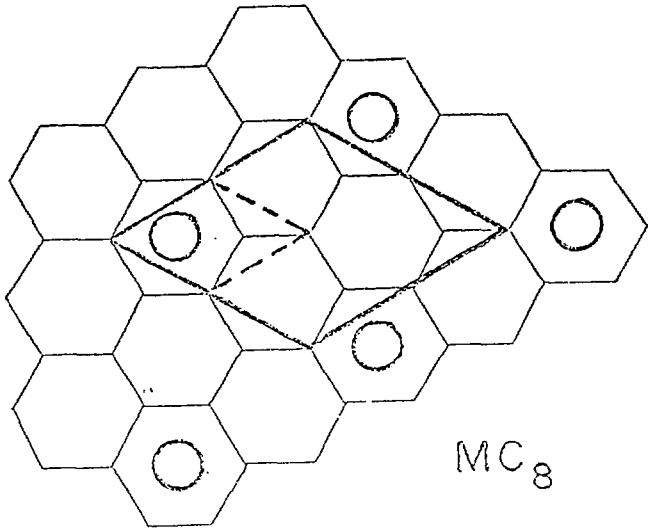

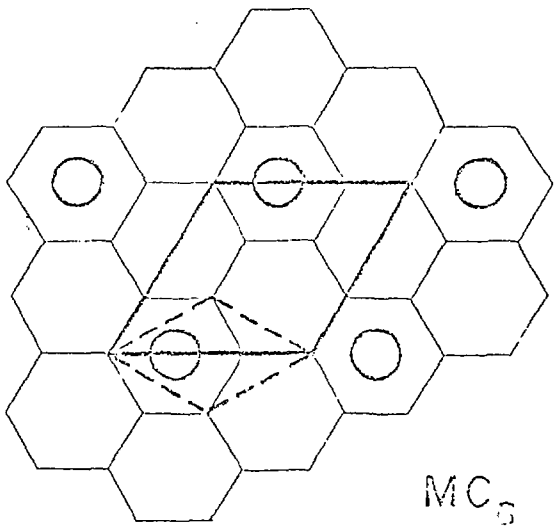

Figure I-3

References
Chapter I

1. L. B. Ebert; Annual Review of Material Science, (1976) 6, 181.

2. F. R. Gamble and T. H. Geballe; "Inclusion Compounds," Treatise on Solid State Chemistry, ed., N. B. Hannay, Plenum Press, N.Y. (1976) 3, 89.

3. G. R. Hennig; Progr. Inorg. Chem. (1959) 1, 125-205.

4. W. Rudorff; Adv. Inorg. Chem. Radiochem. (1959) 1, 223-66.

5. J. Fischer; Physics and Chemistry of Materials with Layered Structures, Intercalation Compounds, (to be published).

6. Riley; Fuel (1945) 24, 8-15, 24-53.

7. Lin Chun-Hsu, et al.; Inorg. Nucl. Chem. Letters (1975) 11, 601-603.

8. E. R. Falardeau, L. R. Hanlon and T. E. Thompson; Inorg. Chem. (1978) 17, 301.

9. Yu. N. Novikov and M. E. Vol'pin; Russian Chem. Rev. (1971) 40, 733-746.

10. A. R. Ubbelohde; Nature (1966) 210, 404; M. J. Bottomley, G. S. Parry, A. R. Ubbelohde, and D. A. Young; J. Chem. Soc. (1963), 5674; A. R. Ubbelohde; Proc. Roy. Soc. A. (1969) 309, 297.

11. E. R. Falardeau, G. M. T. Foley, C. Zeller and F. L. Vogel; J. C. S. Chem. Comm. (1977), 389.

12. Lin Chun-Hsu, et al.; Inorg. Nucl. Chem. Lett. (1975) 11, 601.

13. F. L. Vogel, et al.; Material. Science and Eng. (1977) 31, 231.

14. T. E. Thompson, E. R. Falardeau and L. R. Hanlon; Carbon (1977) 15, 39-43.

15. H. Fuzelher, J. Melin and A. Herold; Carbon (1977) 15, 45-46

16. C. Zeller, G. M. T. Foley, E. R. Falardeau and F. L. Vogel; Material Science and Eng. (1977) 31, 255.

References, Chapter I, continued

17. N. Bartlett, R. N. Biagioni, B. W. McQuillan, A. S. Robertson, and A. C. Thompson; J. C. S. Chem. Comm (1978), 200.

18. N. Bartlett, B. McQuillan, and A. S. Robertson; Mat. Res. Bull. (1978) 13, 1259-1264.

19. N. Bartlett, E. M. McCarron, B. W. McQuillan and T. E. Thompson; submitted to Synthetic Metals.

20. L. B. Ebert and H. Selig; Mat. Sci. and Eng. (1977) 31, 177-181.

21. B. R. Weinberger, et al.; submitted to Sol. St. Comm.

22. L. B. Ebert, R. A. Huggins and J. I. Brauman; J. C. S. Chem. Comm. (1974), 924-925.

23. H. Selig, M. J. Vasile, F. A. Stevie and W. A. Sunder; J. of Fluorine Chem. (1977) 10, 299-318.

24. J. E. Fischer; Mat. Sci. and Eng. (1977) 31.

25. J. E. Fischer; "Electronic Properties of Graphite Intercalation Compounds," Physics and Chemistry of Materials with Layered Structures, ed. F. Levy, D. Reidel, Dordrecht, Holland (1977), Vol. 6 in press.

26. L. R. Hanlon, E. R. Falardeau, and J. E. Fischer; Solid State Comm. (1977) 24, 377-381.

27. J. E. Fischer, T. E. Thompson and F. L. Vogel, in Petroleum Derived Carbons, ed., M. L. Deviney and T. M. O'Grady, (1975) ACS Symposium Series #21, 418.

28. O. Glemser and A. Smalc; Angew. Chem., Int. Ed. (1969) 8, 517.

29. J. Passmore, E. K. Richardson, and P. Taylor; Inorg. Chem. (1978) 17, 1681.

30. J. Ballard and T. Birchall, J. Chem. Soc. Dalton (1976) 18, 1859.

31. N. F. Mott; Metal-Insulator Transitions, Barnes & Noble, N.Y., 1974.

32. J. C. Thompson; Electrons in Liquid Ammonia, Clarendon Press, Oxford, 1976.

References, Chapter I, continued

33. Colloque Weyl IV; The J. of Phys. Chem. (1975) 79.

34. D. F. Burow and J. J. Lagowski; Adv Chem (1965) 50, 125.

35. J. Jortner; J. Chem. Phys. (1959) 30, 839.

36. N. F. Mott; J. Phys. Chem. (1979) 79, 2915.

37. J. V. Acrivos and H. F. Mott; Phil. Mag. (1971) 24, 19;
J. V. Acrivos; Phil. Mag. (1972) 25, 757

38. M. H. Cohen and J. Jortner; J. Phys. Chem. (1975) 26, 2900.

39. J. E. Enderby, D. M. North and P. A. Egelstaff; Phil. Mag. (1966) 14, 961.

40. P. Chieux; J. Phys. Chem. (1975) 79, 289.

41. N. W. Ashcroft and J. Lekner; Phys. Rev. (1966) 145, 83.

42. N. W. Ashcroft and D. C. Langreth; Phys Rev. (1967a), 156, 685.

43. M. Gold and K. S. Pitzer; J. Am. Chem. Soc. (1962) 84, 2264.

Chapter II

XAS THEORY AND EXPERIMENT

The absorption coefficient is $\mu = \mu_P + \mu_I$. μ_I is the photoelectric absorption coefficient of the element being studied. μ_P is the pre-edge absorption coefficient of the other absorption edges which have a lower energy than the edge of interest, as well as Compton and Thompson scattering from the elements in the sample. μ_I may be written as:

$$\mu_I = \mu_E + \mu_S + \mu_o \chi(k) \qquad \text{(II.1)}$$

where μ_E contains the edge rise caused by the onset of the continuum and transitions to unoccupied states near the edge onset; μ_S is the smooth monotonic absorption beyond the edge of the element being studied; μ_o is the free atom absorption beyond the edge; and $\chi(k)$ is the EXAFS. A method of experimental extraction of this formula from XAS data, as well as discussions of the region beyond the edge, will be presented in subsequent sections.

A. XAES Theory

This section discusses the μ_E, the XAES or edge region of the

data. The XAES region of the data contains transitions of an inner shell electron to unoccupied bound orbitals (1). For ionic and molecular compounds, these transitions are promotions of the electron into empty atomic and molecular orbitals. For metal and semiconductors, these transitions are promotions of the 1s electron into partially filled or empty conduction bands, into excitonic, or hole states. In all cases, as the energy of the incident photon which creates the photoelectron is increased, different states are reached until finally, the discrete states or bands merge with a continuum band of unoccupied free electron states (2,3).

To date, the understanding of the nature of the XAES data is mostly qualitative. A good review of this understanding as applied to coordination chemistry was presented by Srivastava and Nigam (4). A qualitative classification of the types of spectra was presented by Van Nordstrand (5,6). The edge shape was correlated with the known local environment and symmetry around the absorber being studied.

Correlations of the position and shape of the edge features have been made with the oxidation state of the absorber. The edge width (7), the inflection point in the absorption edge (8), the position of the main absorption maximum (9), as well as the position of other peaks (10), have been used for this purpose. The inflection point E_i where $\left(\frac{\partial^2\mu}{\partial E^2}\right) E_i = 0$ is a valuable piece of information only if inflection points of the same feature are used in all cases. The inflection point of an edge in one compound which does not have a certain peak because the transition is not allowed cannot be compared

with the inflection point of another compound in which that transition is allowed. Since broadening of the data exists, these problems do affect the accuracy of the correlations.

In a recent paper, Shulman et al.(10) have extended and refined this qualitative understanding. Highly ionic model systems with fluorine ligands were studied. The approach of using the completely relaxed core approximation and the corresponding atomic states worked well, e.g., consider a transition from the K shell of As^{+5}. The one electron transition is from 1s to n'ℓ' or

$$(As)^{+5}\{1s^2 2s^2 2p^6 3s^2 3p^6 3d^{10}\} \rightarrow (As^*)^{+5}\{1s 2s^2 2p^6 3s^2 3p^6 3d^{10}\}n'\ell' \qquad \text{(II.2)}$$

Shulman et al. treat the excited state n'ℓ' as atomic in character and localized on the metal ion. Since the 1s hole is close to the nucleus, the final state of the outer shell of an ion having atomic number Z can be approximated by the atomic states of the element Z + 1 but with a $1s^2$ core. Thus:

$$(As^*)^{+5}\{1s 2s^2 2p^6 3s^2 3p^6 3d^{10}\}n'\ell' \equiv (Se)^{+5}\{1s^2 2s^2 2p^6 3s^2 3p^6 3d^{10}\}n'\ell' \qquad \text{(II.3)}$$

The transition is from As^+ to $Se^+(n'\ell')$ in this approximation. The spectroscopic tables (11) of the (Z + 1) ion (Se^{+5}) can be used. Figures II-1 and II-2 show the spectra of $Cs^+AsF_6^-$ and AsF_3 and the appropriate ionic states as illustrations of how this works for two highly ionic compounds which were studied in this work.

For their highly ionic compounds, Shulman et al. (10) were able to identify 1s → 3d, 1s → 4s, 1s → 4p transitions in the iron

fluorides and predict their intensity in agreement with optical transitions.

For a detailed comparison of these spectra, calculations of the molecular orbitals with an ionized absorbing atom must be made. Such calculations are not available. Note that 1s → 3d and 1s → 4s transitions are allowed only by vibronic mixing of states as required by the symmetry of the local environment. In a tetrahedral environment, a 1s → 3d transition is allowed while in an octahedral, it is not allowed.

Ab initio calculations of various metal spectra which agree well with XAES spectra have been made (12). The $\ell = 1$ projected density of final states was computed by the linear augmented plane-wave (APW) method. In addition the Ti emission and absorption spectra of various oxides of Ti have been compared favorably with theoretical calculations (13).

Therefore for all compounds a great deal is understood about the nature of the edge region. However, there is still need for the qualitative approach reviewed by Srivastava and Nigam (4). The identity and nature of the absorption site affect the spectra. When these are unknown, interpretation of the edge spectra is often at a qualitative level.

B. EXAFS Theory

Above the edge onset, as the energy is increased, there is a gradual decline in the absorption cross section μ_S of equation II.1. Simple theory predicts only this smooth decrease. The transition

of electrons into this continuum region of free electrons is modulated by an oscillatory structure, $\mu_o\chi(k)$ of equation II.1, which has been called EXAFS.

The early theories of the EXAFS modulations were reviewed in 1963 by Azaroff. The theories can be divided into two basic types: long range order (LRO) and short range order (SRO). Kronig (15,16) described the modulations in terms of a change in the density of states due to the diffraction of final state electrons off periodic planes of atoms. This LRO theory was modified by Hayasi (17,18).

Kronig (19) and Petersen (20,21) also first introduced the SRO theory as an explanation for the fine structure in the absorption spectra of a diatomic molecule. Kostarev (22) criticized Kronig's original theory because it did not explain features of non-crystalline materials. He developed a short range order theory (22,23) in which scattering from nearby neighbors caused the EXAFS modulation. In support of an SRO theory, Shiraiwa et al. (24,25) pointed out that the ejected photoelectron travels only a few lattice spacings before the amplitude of its wave becomes zero. In 1961, Kozlenkov (26) reviewed the SRO theories.

The SRO theoretical approach has proven to be the most accurate description. The greatest advancement of EXAFS theory was presented by Sayers et al. (27,28). Further refinement of the theory (29) showed excellent agreement with the data. This showed that the interference of the wave backscattered by nearby atoms with the original outgoing electron wave is the basis of the EXAFS modulations. The basic theoretical equation derived is:

$$\chi(k) = \sum_j \frac{N_j}{kR_j^2} |f_j(k,\pi)| \, e^{-2\sigma_j k^2} e^{-R_j/\lambda(k)} \sin\{2kR_j + \alpha_j(k)\} \qquad \text{(II.4)}$$

where the sum is over all shells and types of atoms, N_j is the number of atoms at a distance R_j from the absorber of interest, k is the photoelectron wavevector (defined by $k = \frac{1}{\hbar}\sqrt{2m(E - E_o)}$, where E is the X-ray photon energy and E_o is the threshold at which the electron becomes free), $|f_j(k,\pi)|$ is the magnitude of the scattering through π radians off nearby atoms, $\alpha_j(k)$ is a sum of the phase shifts due to the scattering process of nearby atoms and the potential well around the absorber of interest, σ_j is the mean square relative displacement of the atom j along the line from absorber to scatterer and $\lambda(k)$ is the mean free path of the electron.

Figure II-3 demonstrates a qualitative description of the EXAFS effect. An x-ray photon of energy $E = h\nu$ liberates a photoelectron from the absorber A which can be represented as a free outgoing spherical wave (solid lines on Figure II-3). This wave has a probability for backscattering from nearby atoms B. This backscattered wave (dashed lines on Figure II-3) can interfere constructively (Figure II-3a) or destructively (Figure II-3b) with the original outgoing electron wave. As the energy of the photon is increased, the electron's energy is correspondingly increased. Its wavelength decreases and the constructive and destructive interference of Figures II-3a and II-3b alternate. This changing interference pattern modulates the transition matrix element of the photon absorption process.

Note that the shape of the backscattering envelope $|f_j(k,\pi)|$ depends on the nature of the scattering B. $\alpha_j(k)$ depends on the type of both the absorber atoms A and B. It can be separated into the component parts contributed by atoms A and B. To a limited extent, these parameters are also dependent on the oxidation state of atoms A and B.

Sayers et al. (17,18) made a simple calculation using muffin tin potentials and point scatterers which agreed well with the experiment. More sophisticated calculations followed. Kincaid used the Hartree-Fock approximation to calculate EXAFS theoretically (30,31). His major discrepancy was that the theoretical values were twice the size of the experiment.

Ashley and Doniach (32,33), Hayes and Sen (34,35), and Lee and Pendry (36) expanded and generalized the theory. Multiple scattering (33) of the electron can occur. Focusing (36) of the electron occurs when the first and second shells around the absorber are colinear. Under most circumstances, these effects are negligible and the single scattering theory of Sayers et al. in equation II.4 provides an excellent description of the EXAFS spectra (33,36).

Recently Lee and Beni (37) and Teo and Lee (38) have made ab initio calculations of the absorber and scatterer phase shifts and scatterer amplitude using Herman-Skillman and Clementi Rossi wave functions. The agreement of these calculations with experiment is excellent (37,38). Therefore it is not always necessary to have

known model compounds to provide these parameters in order to analyze an unknown system. Teo's calculations are used in the analysis of the data in this work.

C. XAS Experiment

X-ray absorption spectroscopy experiments are conceptually simple. The X-rays from a broadband X-ray source are passed through a tunable monochromator. The intensity of the beam in front of the sample (I_o) and behind the sample (I) are measured as the monochromator is swept through the energy range of interest. From Lambert-Beer's law, $I = I_o e^{-\mu x}$, the absorption coefficient for a give sample thickness x can be calculated, $\mu = \ln(I_o / I) / x$ $\mu = \mu_I + \mu_p$ where μ_I is the photoelectric cross section of the absorption edge of interest and μ_p is the slowly varying absorption due to other edges and scatter.

The excitation of the photoelectron creates an inner shell vacancy which may relax via a radiative transiton from a higher occupied state. The probability of this fluorescence is proportional to the original absorption probability. Therefore fluorescence is a direct measure of the photoelectric cross section μ_I . In practice, for thin or dilute samples, if the fluorescence intensity F is measured, then $\mu = k\frac{F}{I_o}$ where k is a slowly varying number which depends on the fluorescence efficiency, the detector solid angle, sample thickness and total crosssection μ . The fluorescent technique is mentioned because it was first used by our research group (39).

The synchrotron radiation source and XAS experimental equipment at the Stanford Synchrotron Radiation Laboratory (SSRL) were used to perform these experiments. The experimental apparatus is described below and elsewhere (30).

The intense broadband continuous synchrotron spectrum is created by the acceleration of the electrons in the bending magnets of the SPEAR storage ring at the Stanford Linear Accelerator Center (SLAC). Experiments were not performed using X-ray tubes because they have less intensity. A 20 minute experiment at SSRL would require 10 days with a standard X-ray tube. The synchrotron radiation beam exits the SPEAR vacuum through a thin beryllium window and travels 15 to 20 meters through a beam pipe to the monochromator.

The monochromator consists of two parallel crystals which diffract the beam via Braggs law:

$$n\lambda_{hk\ell} = 2\, d_{hk\ell} \sin \theta_B \qquad \text{(II.5)}$$

where $\lambda_{hk\ell}$ is the wavelength of the x-rays diffracted by the (hkℓ) plane of d-spacing $d_{hk\ell}$ through angle $2\theta_B$, and n is the harmonic order. Since the beam is diffracted once by each crystal, the beam exits the monochromator parallel to the incident beam displaced by the height

$$H = 2D \cos \theta_B \qquad \text{(II.6)}$$

where D is the distance between the crystal faces. By turning the entire monochromator assembly, the X-ray wavelength can be changed

and swept across the energy range of interest. A diagram of the XAS experiment is shown in Figure II-4.

The high intensities of typical operating conditions dictate the usage of ion chambers for the measurement of I_o and I for the absorption experiments. In order to fully use the high intensity, the continuously monitoring front I_o ion chamber is necessary to correct the erratic time and spatial dependence of the SPEAR beam. Solid state ion chambers have been built for use at SSRL. Under low intensity conditions. a NaI scintillator can be substituted for the rear ion chamber. However, under normal conditions, the front chamber I_o is a 6" long gas flow chamber and the rear chamber is a 12" long gas flow chamber. Typically, the front chamber gas is adjusted so that it absorbs about 10% of the beam and the rear chamber is adjusted so as to absorb most of the beam. If harmonics of the fundamental beam are large, the gas in the rear chamber may have to be adjusted to minimize the effects of these undesirable energies in the beam. The current generated by the passage of the X-ray beam through the ion chamber is amplified by a Keithly electrometer to a voltage which is then converted to a frequency proportional to that voltage. This voltage is then counted by a computer-interfaced scalar for each ion chamber. The fluorescence detection equipment used was either a Si solid state detector or a NaI detector which creates a pulse whenever a photon is detected. These are counted by another computer-interfaced scalar. The dark current of each input is measured with the beam off before the start of the experimental scan. This value is subtracted from each data point.

A PDP-11 computer was used to control the experiment. A complete description of the software package is described by J. Kirby (40). Computer-controlled stepping motors change the energy and wavelength of the beam by changing the angular orientation of the monochromator according to equation II.5 and change the height of the table supporting the detector and sample array according to equation II.6. The computer-controlled counters count the signals I_o, I and F for a time preset by the user. Five regions of variable size with different distances between points and variable measurement times can be specified. The data are written onto floppy disks which are later transferred to magnetic tape which can be read by our analysis programs. The software package at SSRL can also perform some on-line data analysis.

Typically several XAS spectra, each requiring 10 to 25 minutes, were obtained for each sample. Several short scans which can be added later are preferable to one long scan due to the time instabilities of the beam. After injection of electrons into the SPEAR storage ring, the beam intensity slowly decays until the beam unexpectedly loses intensity due to technical difficulties or until the SPEAR operators inject more electrons into the ring. Data collection must cease in any case. This occurs quite frequently. If many short scans are obtained, the few bad scans can be discarded.

Two different types of partial loss of intensity can occur. First, technical difficulties in the operation of SPEAR can cause

a partial loss of beam resulting in a level shift in the data because of the non-linearity of the ion chamber detector system. Second, at certain angles the wavelength of another set of crystal diffracting planes (h'k'ℓ') can equal that of the primary beam (hkℓ). This causes a large decrease in the intensity of the hkℓ beam which is not compensated for by the ion chamber detector system. A so-called "glitch" of limited range is created in the data.

Two different kinds of monochromator energy calibration changes can occur. The first is caused by the new operating conditions each time new electrons are injected into the SPEAR ring. New steering conditions produce a different source point for the synchrotron beam which means that the X-rays impinge on the monochromator at a slightly different angle changing the calibration. A standard compound was run for calibration during each beam fill. The second change is caused by poor design and maintenance of the monochromator system. For several years, with varying degrees of severity on different beam lines, the monochromator calibration has continuously slipped in one direction from scan to scan. Once the data have been obtained, it is difficult or impossible to adequately compensate for the problem. Most of our data was not affected by this problem.

Figure Captions
Chapter II

II-1 Normalized K-shell absorbance of AsF_3. (a) is a scale plot; (b) is expanded to an arbitrary scale. For comparison, these Se^{+3} atomic states (11), calibrated such that the $4s^2p$ state is coincident with the white peak, are plotted. Se^{+3} states approximate the $(As^*)^{+3}$ states if the relaxed core approximation is assumed.

II-2 Normalized K-shell absorbance of AsF_5. (a) is a scale plot; (b) is expanded to an arbitrary scale. For comparison, these Se^{+5} atomic states (11), calibrated such that the 4p state is coincident with the white peak, are plotted. Se^{+5} states approximate the $(As^*)^{+5}$ states if the relaxed core approximation is assumed.

II-3 A schematic drawing which shows the electron interference patterns which cause the EXAFS modulations. The atom A absorbs the photon while the atom B backscatters the "ejected" photoelectron. For energy E_1, the electron wave interferes constructively while for energy E_2, it interferes destructively which causes an absorbance modulation.

II-4 Schematic drawing of the XAS measurement apparatus.

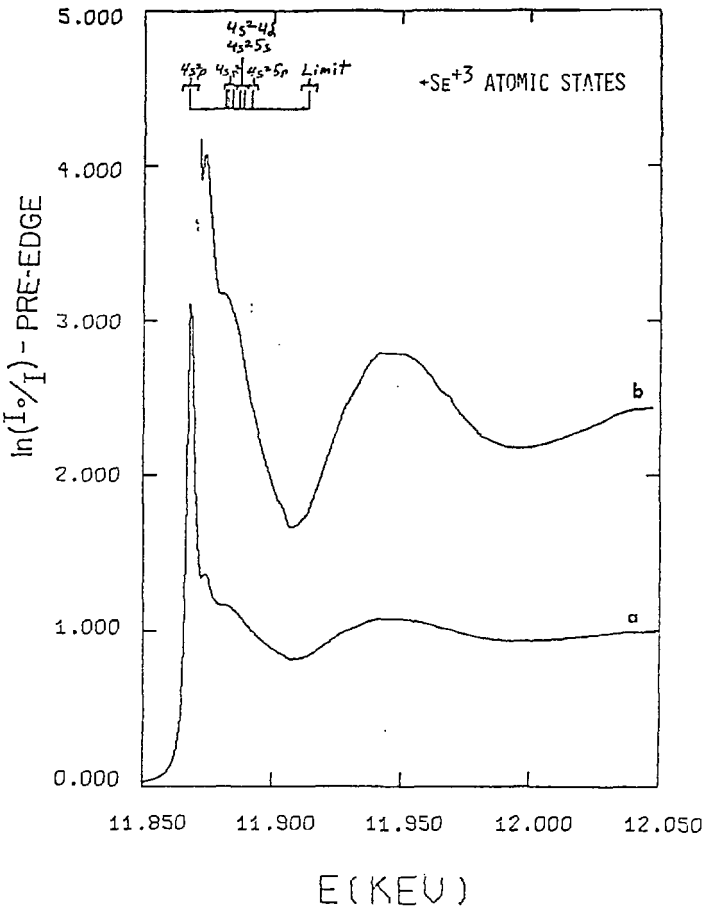
5.000
4.000
3.000
2.000
1.000
0.000
ln(I°/I) - PRE-EDGE
11.850
11.900
11.950
12.000
12.050
E(KEV)
+SE+3 ATOMIC STATES
Limit
b
a

Figure II-1

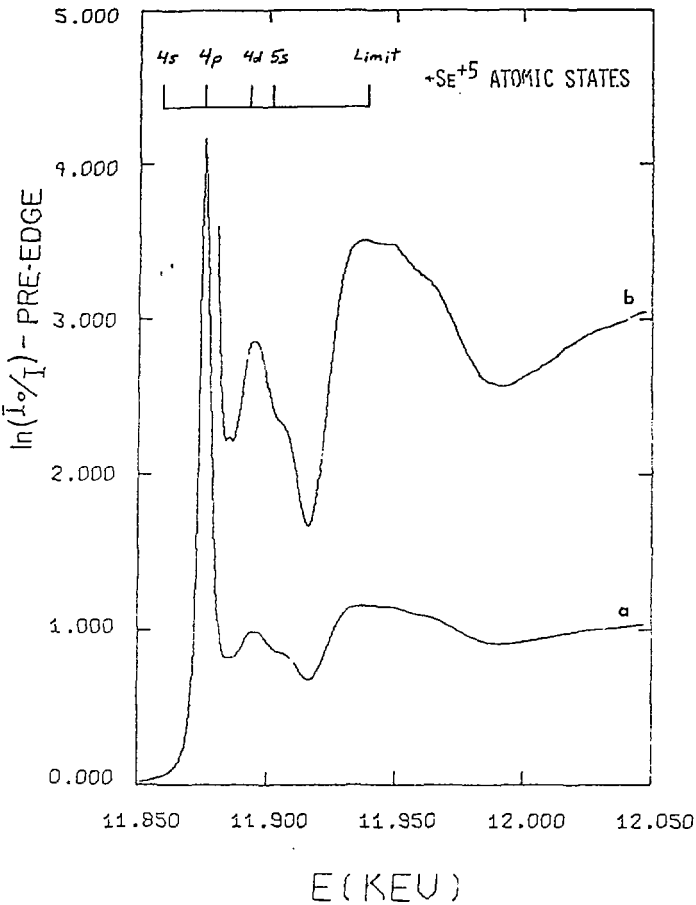
4s 4p 4d 5s Limit
+Se+5 ATOMIC STATES
5.000
4.000
3.000
2.000
1.000
0.000
ln(I°/I) - PRE-EDGE
b
a
11.850
11.900
11.950
12.000
12.050
E(KEV)

Figure II-2

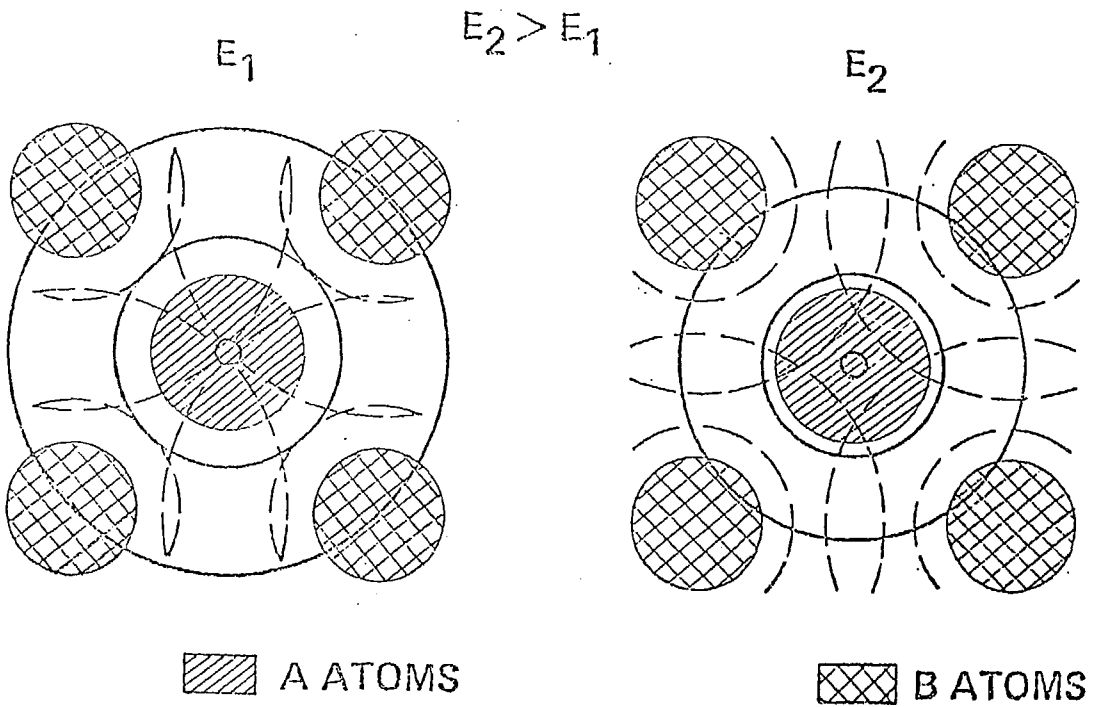

Figure II-3

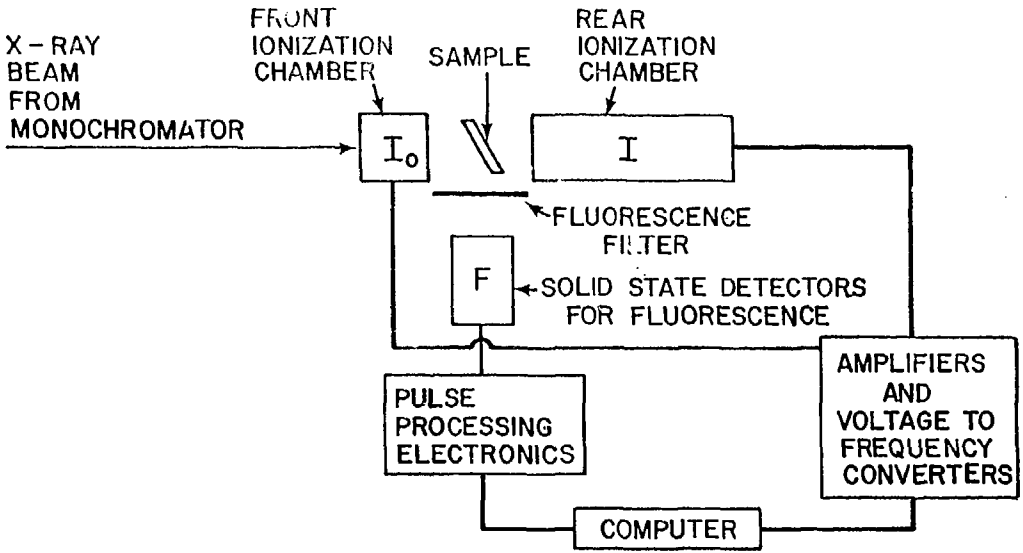

APPARATUS FOR EXAFS MEASUREMENT

XBL778-4525

Figure II-4

References
Chapter II

1. W. Kossel; Z. Phys. (1920) 1, 119-134.

2. R. de L. Kronig; Physik (1931) 70, 317-323.

3. L. G. Parratt; Rev. Mod. Phys. (1959) 31, 616-645.

4. U. C. Srivastava and H. L. Nigam; Coord. Chem. Rev. (1972-1973) 9, 275-310.

5. R. A. Van Nordstrand; Non-Crystalline Solids, ed. V. D. Frechette, J. Wiley & Sons, N.Y. (1958), 168-198.

6. R. A. Van Nordstrand; Handbook of X-Rays, ed. E. F. Kaeble, Mc-Graw Hill Book Co., N.Y. (1967), 43-1 - 43-18.

7. E. Vainshtein, R. Ovrutskaya, B. Kotlyar and U. R. Linde; Soviet Physics: Solid State (1964) 5, 2150-2153.

8. S. Cramer, T. Eccles, F. Kutsler, K. Hodgson and L. Mortenson; J. Am. Chem. Soc. (1976) 98, 1286-1287.

9. H. L. Nigam and U. C. Srivastava; Chem. Comm. (1971) 14, 761-763.

10. R. G. Shulman, Y. Yafet, P. Eisenberger and W. Blumberg; Proc. Nat'l. Acad. Sci.-USA (1976) 73, 1384-1388.

11. C. E. Moore; Atomic Energy Levels, Vol. II, (1952) National Bureau of Standards (U.S.) Circular 467.

12. J. E. Muller, O. Jepsen, O. I. Andersen, and J. W. Wilkins; Phys Rev. Lett. (1978) 40, 720-722.

13. K. Tsutsumi, O. Aita, and K. Ichikawa; Phys. Rev. B (1977) 15, 4638-4643.

14. L. V. Azaroff, Rev. Mod. Phys. (1963) 35, 1012.

15. R. de L. Kronig, Z. Physik (1931) 70, 317.

16. R. de L. Kronig, Z. Physik (1932) 75, 191.

17. T. Hayasi, Sci. Repts. Tohoku Univ. (1949) 33, 123.

18. T. Hayasi, Sci. Repts. Tohoku Univ. (1949) 33, 183.

References, Chapter II, continued

19. R. de L. Kronig; Z. Physik (1932) 75, 468.

20. H. Petersen; Z. Physik (1933) 80, 258.

21. D. R. Hartree, R. de L. Kronig, and H. Petersen, Physica (1934) 1, 895.

22. A. I. Kostarev; Zh. Eksperim. I Teor. Fiz. (1941) 11, 60.

23. A. I. Kostarev; Zh. Eksperim. i Teor. Fiz. (1949) 19, 413.

24. T. Shiraiwa, T. Ishimura, and J. Sawada, J. Phys. Soc. Japan (1958) 13, 847.

25. T. Shiraiwa, J. Phys. Soc. Japan (1960) 15, 240.

26. A. I. Kozlenkov, Izv. Akad. Nauk SSSR (1961) 25, 957.

27. D. E. Sayers; Ph. D. Thesis, University of Washington (1971).

28. D. E. Sayers, F. W. Lytle and E. A. Stern, Advances in X-Ray Analysis, Vol. 13, Plenum Press (1970).

29. E. A. Stern; Phys. Rev. B (1971) 10, 3027-3037.

30. B. M. Kincaid; Ph. D. Thesis, Stanford University (1975).

31. B. M. Kincaid and P. Eisenberger, Phys. Rev. Lett. (1975) 34, 1361-1363.

32. C. A. Ashley; Ph. D. Thesis, Stanford University (1974).

33. C. A. Ashley and S. Doniach, Phys. Rev. B (1975) 11, 1279-1288.

34. T. M. Hayes and P. N. Sen; Phys. Rev. Lett. (1975) 34, 956.

35. T. M. Hayes, P. N. Sen, and S. H. Hunter; J. Phys. C: Solid State Phys. (1976) 9, 4357-4364.

36. P. A. Lee and J. B. Pendry; Phys. Rev. B (1975) 11 2795.

37. P. A. Lee and G. Beni; Phys Rev. B (1977) 15, 2862-2883.

38. B. Teo and P. A. Lee; J. Am. Chem. Soc. (1979) 101, 2815.

39. J. Jaklevic, J. A. Kirby, M. P. Klein, and A. S. Robertson; Solid State Comm. (1977) 23, 679-682.

40. J. A. Kirby; Manual for EXAFS Program, LBL Report No. UCID-3952. (1977).

Chapter III

XAS DATA ANALYSIS METHODS

This chapter contains a general explanation of the data analysis methods. Specific examples of the analysis methodology are contained in Chapters IV and V.

A. Initial Data Preparation

The 9-track ASCII magnetic tapes containing the data taken at SSRL were read on the CDC 6600 at Lawrence Berkeley Laboratory and translated into CDC display code by executing the system routine CODE9. The program SSRP eliminated the header and trailer files on these files on these tapes, keeping only the first 60 characters of each, unblocked the tape files, eliminated all non-interpretable characters and inserted end of line marks in the place of the carriage return/line feed at the end of each line of data. The format or contents of the data were not changed by these two steps. The output files of this program were stored as master files.

The next step of the analysis was to translate each file into a standard format which could be read by any of our data analysis programs. This was done with the program TRANSL run on the CDC 7600 at LBL. The data files written at SSRL and output by the program SSRP

had each input channel listed separately, the front ionization chamber I_o, the rear ionization chambers I_i or the fluorescent counters F_j where i and j represent separate input channels. Each output file of TRANSL was a single channel of information, i.e., I_o/I_i, F_j/I_o or F_j. The purpose of the unnormalized fluorescence output is described in theses by J. P. Smith (1) and J. A. Kirby (2). For the experiments performed for this thesis only absorption data were used.

Removal of Glitches

The data files were first translated by TRANSL which provided both microfiche plots and tape output. The files were then carefully studied to look for crystal "glitches," level shifts, and other "glitches." In addition to the microfiche plots generated by TRANSL, a special program was written to plot various regions of the data. The final determination of the position of the "glitches" was done using an interactive program on a Xerox Sigma 2 computer at LBL. Almost all the problems with the files occurred because of changes in the incident flux. The origins of the crystal "glitches" has been discussed by other researchers (3,4) and in Chapter II, Section C. The problems which only occurred in individual files were due to changes in the operating conditions of the SPEAR accelerator during the scan. Sometimes a scan was aborted due to a SPEAR dump.

For nearly all the runs the only localized "glitches" were crystal "glitches" which always occurred at the same place in each

scan. These "glitch" regions were removed from the data after adding the scans of the same sample. An example of a typical crystal "glitch" is shown in Figure III-1. A level shift, which often occurred shortly before a beam dump, was due to a sudden change in incident flux. This discontinuous change in the data terminated the useable portion of the data.

Adding Data

If enough data were obtained before a beam dump or level shift, the part of the data lower in energy than the point where the problem occurred was used in the adding of the file. The files which were good beyond this cut point were normalized to account for this. As a result no discontinuity in the added file can be noticed. A beam dump, level shift, or an instability in flux through the scan made some scans unuseable.

Both the batch mode TRANSL and interactive program can perform these adds. The TRANSL program was most appropriate when a large number of files were added while the interactive program was best when only a few files were added. For the data collected for this thesis, fewer than ten scans were added for each sample analyzed and the interactive program was used. If only complete files were added, no problems were encountered. However, if the background function changed from one scan to the next and a file was cut short because of one of the above problems a discontinuity or slope change could develop at the cut point. An option in the program adjusted the slope and intercept of the shortened input file so that this problem did not occur.

Shifting Data

In order to obtain the optimum signal-to-noise ratio and to use data which were obtained when the spectrometer calibration slipped additional procedures were used on some files.

First, a few extra "glitches" which looked very much like the crystal "glitches" shown in Figure III-1 occurred in random locations in several scans. They were removed before adding by substituting up to five points by a linear interpolation between the two good points just outside the region. This point substitution was limited to one day's experimental run and was limited in extent on that day.

Second, when the monochromator energy calibration changed, the position of the data points had to be shifted before adding. This was essential for the edge region where the features are quite narrow.

In order to determine whether shifting was required before adding, derivatives of the edge data were taken. By comparing the position of inflection points and peaks in the data, the required shift was determined.

Two shifting programs were used for this purpose. One program was an integral part of the TRANSL program while the other program, SHIFTEM, ran on the Sigma 2. Both programs created a shifted output array by using a linear interpolation between the points of the input array. Before shifting and adding, all "glitches," including the crystal "glitches," were changed using the point substitution described in the previous paragraph. This was done even on crystal "glitches" so that the extent of the "glitch" was not made to cover a larger range of the data by the shifting and linear interpolation

procedures.

This effect can be seen clearly if one assumes, for example, that a given "glitch" extends over the same 3 data points 50 steps apart in all the files. If the shift which covers a range of $\pm$ 10 steps around a central reference file is needed then the added file would have a "glitch" which covered 5 points instead of the original 3. By using a point substitution before adding, these 2 additional points are not contaminated by the "glitch." The shifting was only needed for two sets of experimental scans, one each of Rb and As.

After the adding was completed, the crystal "glitch" regions and the bad points at the beginning and end of the data files were removed from the file by deleting these points from the set of points.

Other researchers have smoothed the data to remove "glitches" (5). Tom Eccles fit a polynomial in the region just outside the "glitch" (6). This may seem similar to the straight line used for our data analysis but it is not. None of the "glitches" which exist in every one of the data files was kept for data analysis. Only the few scattered "glitches," which were corrected on individual files before adding, were left in the data for analysis. The deletion of bad points maintained the statistical independence of each of the data points used for analysis. Our analysis method proceeds as if these bad points were never obtained.

In order the check the point substitution, shifting and adding, the summed file was carefully checked. Also analyses were done of

individual files and of sums of a few files. Except for signal-to-noise changes, no differences in the data were evident.

Furthermore, individual files were processed so that an error bar could be established on the parameters obtained from the inflection points, peak positions, peak heights and other factors which describe the edge region.

Angle to Energy Conversion

By comparison with a standard Cu foil, the energy calibration of the monochromator was determined in the first experiment. The energy value of the main absorption peak of a standard compound was determined from one set of data. The standard compounds were As_2O_3 for the As K-edge and RbBr for the Rb K-edge. For each subsequent experiment the spectrometer was calibrated by making the absorption peak energy of the standard compound the same as had been determined in the first experiments. The absolute accuracy of this energy scale was about 5 eV. However, for experiments which had no monochromator slippage, the internal accuracy of the calibration was better than 0.3 eV. When monochromator slippage occurred, positions of features could not determined with this same accuracy. But after shifting the data, a comparison of both edge and EXAFS features could be made. Corrections accurate to 1.0 eV were made on these data. EXAFS features are so slightly affected by this slippage in the energy calibration that it does not affect the analysis. For XAES analysis, the calibration is critical. However, the features can be compared even if the absolute energy calibration is not accurate.

The X-axis values of the data were the steps of the stepping motor which turned the monochromator crystal through a given angle. The energy calibration procedure described above determined the stepping motor position which corresponded to zero angle. As described in Chapter II, Section C, the energy which corresponds to a given angle is $E = hc/\lambda$ where the photon wave length $\lambda = 2d \sin \theta$, where d is the distance between the diffracting planes of the crystal and θ is the Bragg angle.

Description of the Data

The following discussion pertains to absorption data. The logarithm step was eliminated for fluorescence data analysis. The signal originally detected was $S = \frac{I_o}{I}$ versus the energy of the incident photon. Since we wanted to analyze the absorption coefficient μ, the natural logarithm was taken. The measured quantity

$$M = \ln \frac{I_o}{I} = \mu x + B \qquad \text{(III.1)}$$

was obtained where x was the thickness of the sample and B was the background of the detector. The measured current of each ion chamber was proportional to the true flux of the beam. The current obtained depended upon the x-ray energy as well as the ion chamber length and gas content. In addition, the ion chamber measurement system was only linear over a limited range of intensities. As discussed by J. P. Smith (1) and S. H. Hunter (3), an additional background function exists which contributes to the absorption coefficient. Additional background arises from any additional material such as sample cell windows which are between the two ion

chambers.

This background, B, is a function of energy which varies if the samples or the operating conditions are changed. The photon flux changes both with photon energy and with time as the SPEAR operating conditions change. Therefore, B is a slowly varying experimental artifact which is removed empirically.

The absorption coefficient $\mu = \mu_P + \mu_I$ where μ_I is the photoelectric absorption coefficient due to the absorber edge of interest. μ_I can be further separated as follows: $\mu_I = \mu_E + \mu_o + \mu_C + \mu_o\chi(k)$ where μ_E is the absorption coefficient of the edge features, μ_o is the monotonic free atom absorption coefficient above the edge which follows the Victoreen formula (7) and the McMaster tables (8), μ_C is the monotonic correction to the absorption coefficient just above the edge because the atoms are in a condensed state (9,10) and $\chi(k)$ is the EXAFS modulation (9) which begins just above the edge. k is the wavevector of the free photoelectron ejected from the atom of interest

$$k = \hbar^{-1} (2m(E - E_o))^{\frac{1}{2}}$$

or use $k = \sqrt{2m(E - E_o)} / \hbar$ where E is the photon energy and E_o is the energy at which the photoelectron becomes free. $E - E_o$ is the energy of the photoelectron. μ_P is the pre-edge absorption coefficient which is due to the other absorption edges which have a lower energy than the edge of interest as well as Compton and Thompson scattering from the elements in the sample. This pre-edge background and the detector background B extend above the onset of the edge of interest.

Pre-Edge Background Removal

Other researchers have used differing methods to remove this background for analysis. A Victoreen formula (7) ($C\lambda^3 + D\lambda^4$, where λ is the photon wave length) can adequately describe the background absorption coefficient μ_p. Lytle et al. (9) have used this functional form to subtract the pre-edge background.

Other researchers (3,6) pointed out that this functional form could not necessarily be expected to fit the detector background B. Thus a general polynomial was used. Our pre-edge strip was done with a polynomial function of ln(E) where E was the photon energy. This functional form was chosen because the most recent x-ray cross-section tables (8) were tabulated using this functional form. The fit was done from 350-500 eV to 50 eV below the onset of the edge. The quadratic fit, $a_o + a_1 \ln(E) + a_2(\ln(E))^2$ was found to be the functional form. A representative pre-edge fit is shown overplotted with data in figure III-2.

Other researchers have used polynomials in E and Tschebychev polynomials in E^{-n} (3). S. H. Hunter (3) and T. M. Hayes (11) noticed that a general polynomial function would sometimes turn upwards when extrapolated above the absorption edge. Since they wished to make the background function 1000 eV above the edge meaningful and use this background function to normalize their EXAFS data, an elaborate procedure to eliminate this upturn was devised.

We realized that for many of our systems, particularly fluorescent data, the background function below the edge could not be extrapolated to approximate the background function 300 to 1500 eV

above the edge. Thus, in our analysis methodology we did not use the post-edge background function for EXAFS normalization in the same manner as others have done (3,4,6,9,11). It was only used to normalize to 1.0 the observed edge jump at the energy where the photoelectron becomes free. The pre-edge strip was necessary for this normalization but it did not need to be extrapolated far above the edge onset for data analysis. In fact the form of this strip affected the shape of the features only in the XAES region of the data. A quadratic fit over the limited range of 350 eV to 50 eV below the edge could be extrapolated to 50 eV above the edge beyond the XAES region of data. The advantages of our stripping method are its independence of sample thickness, data taking method, and differing background problems.

Post-Edge Normalization

After the pre edge had been subtracted the data now had the form $M' = \mu_I x + B'$ where B' was the residual background which was small in the pre-edge and edge region. (The superscript ' is used to signify that a pre-edge strip has been performed.) A general polynomial was fit over the pre-edge region of the data, extrapolated across the entire range of the data and then subtracted from the data. A quadratic polynomial was fit from 200 to 1000 eV above the edge. The edge jump was normalized to 1.0 by multiplying the inverse of the value of this function at the edge.

The data were transformed to an absorption coefficient μ_I* in which the height of the edge jump was 1.0 for the element of interest

$$\mu_I^* = \mu_E^* + \mu_S^* + \mu_o^* \chi(k) \qquad \text{(III.2)}$$

where $\mu_S^* = \mu_o^* + \mu_C^* + B^*$ was a slowly varying background function above the edge onset. The XAES features were contained in μ_E^* which was restricted to a 50 eV region of data around the edge onset. Useable EXAFS modulation $\chi(k)$ started at 50 eV above the edge. These files were used as the standards for both the edge and EXAFS analysis. (The superscript * is used to signify that the data have been normalized such that the edge jump in the absorption coefficient has the value 1.0.) Figure III-3 shows the normalized data with the normalization polynomial overplotted.

Fluorescence Detection

Note that a similar discussion could be made for fluorescence data except that the source of the detector background function is different and there is no pre-edge absorption coefficient μ_P. If one either uses dilute or thin samples then the detection equation for fluorescence reduces (12) to an equation similar to equation III.1 $M = c\mu + B$ where c is a proportionality constant for fluorescent detection efficiency and B is a slowly varying background function. Thus the analysis methodology described will result in an expression for fluorescence experiments which is identical to equation III.2.

B. XAES Analysis

The standard preparation of the data for edge analysis results is described by equation III.2 in the last section. In the region just below the onset of the edge to about 50 eV above the edge the

background is negligible and the EXAFS does not follow the high energy approximation, $\chi(k)$ calculated from theory. In this region, the data $\mu_I^* \approx \mu_E^*$.

Because of the difficulty of an exact calculation of the transitions to molecular orbitals or bands, most of the analysis done on edges involved qualitative comparisons of different samples (4,6,13).

It has been shown that the following quantities are qualitatively related to the chemical oxidation state of the absorber for K-edges of elements:

- absorption edge energy as measured by the inflection point of the absorption onset.
- the edge width as measured by the energy difference between the initial inflection point and position of the main transition peak.
- The energy of any transition as measured by its peak position or the inflection point of its onset.

The relative intensity of transitions can indicate coordination environment. Also, if the compound contains a mixture of different types of the atom of interest and if the edge structure is significantly different for each type, one can determine the relative amounts of each type.

The first method of analysis is merely a visual comparison of the data. Lists of different types of spectra which can be correlated with known structures have been compiled for several elements (14). Unfortunately for this analysis, the greatest variety of spectra exist for the transition metal K edges, and not for As and Rb. However, the spectra recorded contain useful information. Figures III-4, III-5, and III-6 show representative As and Rb spectra.

Derivative Analysis

Derivatives of these spectra were calculated to determine the parameters which were listed above, and provide more information regarding the presence of small transitions. As previously described (6), the calculation of the derivative is done by fitting a polynomial of some order, usually between n = 1, a straight line, and n = 5. A cubic or quadratic was generally used in this analysis. The derivative of this function was used as an estimate of the derivative at the central point of the fit. The derivative at each point was calculated separately. The choice of the order of the polynomial and the energy range over which the data were fit affected the amount of noise and the resolution of the derivative. We adjusted these parameters so that the noise level was small and the resolution adequate for analysis. For a variety of fitting parameters, Figure III-7 shows first derivatives of Figure III-5c and Figure III-8 shows second derivatives of Figure III-5c. Cubic polynomial fits over the energy ranges 1.3, 2.2, 3.1, 4.4, and 6.6 eV were used to calculate the derivatives a, b, c, d, and e plotted in Figures III-7 and III-8. The parameters which generated Figures III-7c and III-8c provided a compromise between signal-to-noise ratio and resolution.

From these plots, qualitative comparisons of files can be made. One can also measure the positions and sizes of various features (4,6).

Fitting Analysis

Other researchers (4,15) have fitted a set of Lorenzian lines and an

edge rise modelled according to the arctangent function to the data to obtain positions and intensities of peaks. With the proper understanding of the compound, this analysis would prove useful if the XAES features were well understood. Hu et al. (16) estimated the position of peaks smaller than the main transition by subtracting a fitted quadratic function which approximated the main transition. This method gave some qualitative results for our data.

For the As compounds, we predicted that there would be a mixture of AsF_3 and AsF_6^- in Graphite AsF_5. A fitting program was written to synthesize the spectrum of an unknown compound from those of two or more model compounds. The results of one of these fits are shown in Figure III-9.

Density Calculation

Finally, the area density of the element of interest, and the density if the sample thickness is known, can be calculated from the size of the edge jump via this equation

$$\rho_A = \frac{\Delta(\mu x)}{\Delta\sigma}$$

where $\Delta(\mu x)$ is measured from the absorption spectra, equation III.1, and $\Delta\sigma$ is the change in the cross section published in the McMaster tables (6). $\Delta(\mu x)$ is the constant used to normalize the edge height to 1.0 in obtaining μ_I^* in equation III.2.

C. EXAFS Analysis

This section discusses the EXAFS analysis of the data. The data have been prepared for analysis in the manner discussed in Section A

of this chapter. The point substitution, shifting, adding and "deglitching" of files was important if maximum information was to be extracted from the data. Not all steps of the preparation described in that section are absolutely necessary for EXAFS analysis. Only the normalization of the edge jump to 1.0 is necessary. However, it was convenient to have common master files for both the XAES and EXAFS analysis. The pre-edge strip was not required for EXAFS since a post-edge strip which removed the slowly varying background in the EXAFS region of the data was the first step of the analysis. This background, μ_S* of equation III.2, which has been modified by the pre-edge strip and post-edge normalization, was used solely for the purpose of subtracting background from the data. Other researchers have used this background as an approximation of the slowly varying normalization function, μ_o, required by the EXAFS theory. We used the McMaster tables (8) to provide the free atom cross-section, μ_o. Thus the pre-edge strip only affected the shape of the post-edge background removed and not the resultant EXAFS, χ.

Free Atom Normalization and Background Removal

The part of the XAS scan beyond 50 eV above the edge onset is the EXAFS region of the data. The edge transitions and the onset of the continuum (μ_E*) are negligible in this region. Thus we may rewrite equation III.2 as follows:

$$\chi(k) = \frac{\mu_I^* - \mu_S^*}{\mu_o^*} \qquad \text{(III.3)}$$

or

$$\chi(k) = \frac{\mu_I^*}{\mu_o^*} - S \qquad \text{(III.4)}$$

A discussion of the proper choice of E_o needed to convert from $\chi(E)$ to $\chi(k)$ using $k = \frac{1}{\hbar}\sqrt{2m(E - E_o)}$ is left until later. Even if the background stip method requires the data to be represented in k-space, any choice of E_o within 40 eV of the onset of the continuum is useable for stripping. Data analysis to determine EXAFS results requires a more careful choice of E_o.

Equations III.3 and III.4 provide two different and comparable methods to extract the EXAFS information from the data. Either the slowly varying background can be subtracted from the data before normalization by μ_o^* (equation III.3) or after normalization by μ_o^* (equation III.4). Most other researchers have (3,4,6,9,11) simplified the expression to the following equation similar to equation III.3:

$$X(k) = \frac{\mu_I - \mu_S}{\mu_S} \qquad \text{(III.5)}$$

The substitution of μ_S for μ_o in the dividend of equation III.5 modifies the normalization. While it is true that μ_C is only 5 percent of μ_o at the edge and is negligible above 200 eV past the

edge, the residual background B* above the edge is often quite large. B* is usually small for concentrated samples which are taken using the absorption technique. This is shown in Figure III-10 where the data and free atom absorption coefficient, μ_M* from McMaster (8) are plotted. For some absorption data, as shown in Figure III-11, the background B* due to the instrument is large. The background problem at the end of this data file is due to the decreasing flux of this crystal at high energies. In addition, other writers have reported (1,2) that the fluorescence detector background function B* which includes Compton and Thompson scatter into the detector cannot be removed by any pre-edge strip.

We decided that a consistent general purpose analysis methodology must not be affected by these problems. Other researchers have used the Victoreen formula to approximate μ_o* (17). The McMaster fits (μ_M*) (8) were used to approximate μ_o*. μ_M* for the edge of interest is normalized to 1.0 at the same energy at which the edge jump in μ_I* was normalized to 1.0.

Thus the following equations describe our technique for extracting EXAFS:

$$\chi(k) = \frac{\mu_I^* - \mu_S^*}{\mu_M^*} \qquad \text{(III.6)}$$

$$\chi(k) = \frac{\mu_I^*}{\mu_M^*} - S \qquad \text{(III.7)}$$

Normally Equations III.6 and III.7 would yield the same $\chi(k)$. However, in certain cases such as the one plotted in Figure III-11, the residual background B* was enlarged by dividing by μ_M*.

This enhancement of an unwanted background function made the removal of this function more difficult. Thus equation III.6 was used for this and most of the samples investigated.

The following describes the method used to remove the smoothly varying background from the data. Often more than one background strip was needed in order to obtain the best results. In these cases a strip like that shown in equations III.6 or III.7 was performed to obtain a first estimation of χ (k) of the EXAFS and then another subsequent stripping was performed:

$$\chi_2(k) = \chi_1(k) - S_2 \qquad \text{(III.8)}$$

The first strip can be designed to remove one type of background and the second strip can be designed to remove another. This optimizes the background strip.

Background Removal Techniques

Various techniques have been used to generate the background, χ_S in equation III.6 or S in equation III.7, which must be subtracted from EXAFS.

The following have been described: Fourier filtering to remove low frequencies from the data after subtraction of a straight line (9), fitting of polynomials across the data (3,18), cubic spline fits across the data (4,6,19) and a running average smooth (1) suggested by F. W. Lytle (20).

The Fourier Transform technique disregards the harmonics generated in finite Fourier Transform which remain in the data. We tried the polynomial fitting approach at first. A polynomial of

at least 4th order in energy or wave vector space was usually required to fit the background. With this order polynomial, the polynomial fit to the data of samples with close first shell bond distances (1.6 to 2.0 Å) and low Z scatterers, followed the EXAFS in the low regions of the data. This removed part of the EXAFS and was undesirable. A quadratic was sometimes used as a preliminary strip for certain difficult backgrounds. S. H. Hunter (3) was able to do excellent background strips using fourth or sixth order Tschebychev polynomials in k-space with a weighting of k or k^2 times the data. The success of this technique was aided by the large first shell distance (2.4 Å) and high Z scatterers typical of the samples studied. The resultant polynomial was minimally affected by the EXAFS present for both of these reasons. The cubic spline has also worked well except that is usually leaves a peak in the Fourier Transform at about 0.4 Å to 0.8 Å (21). With phase shift included, first shells of fluorine at 1.8 Å have a maximum at 'R' = 1.2 Å. The cubic spline residual background peak would interfere with the interpretation of this peak.

The running average smooth was used in this work. The running average strip is basically a very heavy smooth which does not follow the EXAFS or high frequency noise. A similar size region of data centered around each data point was used. At the extremes of the data file a quadratic fit was used to estimate the background. The first smoothed background S^1 was created for each point by simply averaging the data in the region. This process can be repeated n times on the new smoothed file to create a smoothed background, S^n.

Typically n was 3. J. P. Smith (1) and J. A. Kirby (2) used this technique in energy space. This technique is applicable in a wider variety of spectra if it is performed in k-space as is standardly done in this work. The strip then removed similar frequencies in all parts of the spectrum.

For data in energy space, higher frequency components would be removed at the higher energy end of the spectrum since E is proportional to k^2. Thus if the spectrum extends to k values much greater than 14 $1/\mathring{A}$ or if one is not careful, low frequency EXAFS may be removed at high k-values and not at the beginning of the data.

Background Optimization

Examples of the data with the background strip created by a simple quadratic fit in energy space, as well as several different smoothing strips, are shown in Figure III-12. The background subtracted was chosen in the following manner. Various stripped files were created by changing the size of the smoothing region from 5 times the size of the slowest EXAFS frequency to half the size of that frequency. Figure III-12a is the original data file. Figures III-12b to III-12f are plots of the following strips: (b) a single smooth (S^1) over 2 $1/\mathring{A}$; (c) a triple smooth (S^3) over 1.2 $1/\mathring{A}$; (d) a triple smooth (S^3) over 2 $1/\mathring{A}$; (e) a triple smooth (S^3) over 4 $1/\mathring{A}$; and (f) a quintuple smooth (S^5) over 2 $1/\mathring{A}$. Figure III-12d is the optimum strip.

The smoothing strip used was chosen such that the value of the Fourier Transform near R = 0 was small (typically less than one-

tenth the largest EXAFS peak). The smoothing strip choice was also restricted by requiring that the lowest frequency EXAFS peak amplitude remain unaffected. As a final check, the background functions removed were plotted with a quadratic fit subtracted from them so that the highest frequencies of the background removed from the data could be checked. This technique removed the background without affecting the EXAFS spectra $\chi(k)$.

The background strip removed above is adequate for most analysis. However, since a great deal of the analysis described below was performed on the function $k^3\chi(k)$ and its Fourier Transform $\phi_3(R)$, a second smoothing background strip was performed on $k^n\chi(k)$ with n usually equal to 3 although values of n = 2, 4, or 5 were sometimes better. The resultant file $\chi_1(k)$ was modified as follows: $\chi_2(k) = k^{-n}(k^n\chi_1(k) - S_2^{\,3})$ where $S_2^{\,3}$ was typically another triple smooth background strip using approximately the same range as the first strip.

In order to optimize the strip at low k-values it was necessary to change the starting point of the file by deleting points below a certain k-value. These cutoff points were typically below k = 1.0. This is below the region of data used for EXAFS analysis. The double stripping technique combined with the deletion of points below a variable k-value optimized the strip at both the lower and upper limits of the data.

Fourier Transform

Separation of the EXAFS into its various frequency components via Fourier Transform can be used as an aid for background stripping

as described above or as an integral part of the analysis technique as described below. Since the theoretical form of the EXAFS is a sum of sinuisoidal functions with the argument $2kR + \alpha(k)$ the following Fourier Transform can be used to extract structural information (10,22):

$$\phi_n(R) = \int_{k_i}^{k_f} \{k^n W(k)\chi(k)\}\, e^{i2kR} dk \qquad \text{(III.9)}$$

where k_i and k_f are the initial and final k values, W(k) is an apodization window function (to remove side lobes in Fourier Transform), and k^n is a weighting function where n has been varied from -3 to 7 under some circumstances.

Typically, n is 1 or 3 since the transform with n = 1 is related to the spatial variation of the scattering matrix and the transform with n = 3 is related to a psuedocharge density (22,23). Practically, however, this k weighting is merely a weighting function which allows different portions of the data to be weighted differently. Since the k dependence of the amplitude function of the theoretical $\chi(k)$ expression $|F(k,\pi)|\, e^{-\sigma^2 k^2}/k$ varies for different scattering elements, elemental identification can be obtained by studying different $\phi_n(k)$ transforms.

Multiplication by k^n with $n > \phi$ prior to Fourier Transformation tends to reduce the damping of the EXAFS modulation. This effect results in an improved resolution in $\phi_n(R)$. However, it also decreases the signal to noise somewhat since the signal to noise ratio of the EXAFS is poorer at high k since the signal is damped.

In addition, the higher energy data more closely approximates the theory. Furthermore, k^n weighting, $n > 0$, reduces the effect of differing E_o choices since $E >> E_o$ near the end of the data. These factors must be considered when analyzing the data.

The EXAFS data used in any transform is only a finite samoling of the entire EXAFS which would extend from $k = \phi$ to $k = \infty$. Data cannot be used much below $k = 2.5\ 1/\mathring{A}$ since the theory is a high energy approximation. It is also not practical to obtain data beyond 1000 eV or 1500 eV above the edge since the damped oscillation usually decays into the noise by this energy.

This finite range of the transform has already modified the desired infinite transform

$$\phi_n(R) = \int_0^\infty \{k^n W_s(k) X(k)\}\, e^{2ikR} dk \qquad \text{(III.10)}$$

with $W_s(k) = 1.0$ for all k. Limitation of the data range to k values between k_i and k_f as in equation III.10 is equivalent to having $W_s(k) = 0.0$ below k_i and above k_f, and $W_s(k) = 1.0$ between k_i and k_f. The effect of this apodization window is the convolution in R-space of the Fourier Transform of this $W_s(k)$ with the desired transform of $k^n\chi(k)$. The power spectrum of the window function transform is shown in the dashed trace of Figure III-13. The sidelobes evident in Figure III-13 interfere with analysis of small peaks which may be near the sidelobes of large peaks. These sidelobes can be reduced by multiplying the data by a suitable apodization window, W(k) in equation III.9. The Kaiser window (24)

was usually used in this analysis. Kaiser (24) has shown that this window is nearly optimal in the sense that the maximum power is concentrated in the central peak of the data for a given broadening of that peak. Figure III-14 shows a set of these windows. Their Fourier Transform power spectra are shown in Figure III-13.

Hayes has used a gaussian convolved with the square window (25) as W(k). Sayers (26) has modified the Hamming window (27). The use of non-rectangular window functions is discussed in general in reference 27 and as it applies to EXAFS in references 28 and 29.

The Fourier Transform which was used to test the backgrounds was $\phi_1(R)$ or $\phi_3(k)$ with a Kaiser window with $\alpha = 4$, $k_i = 2.0 - 4.0$ and $k_f = 13.5 - 18.0$, depending on the data.

The Fourier Transformtechnique is an integral part of any analysis. It provides a quick look at all the data with the different shells of the radial distribution function separated at their different distances, R_j.

The EXAFS, $k^2\chi(k)$, for $As_2O_3$is plotted in Figure III-15. In Figure III-16, the Fourier Transform ϕ_1 and ϕ_3 of As_2O_3 are plotted using a Kaiser window of 4.0 and the data from k = 4.0 - 15.6. The first peak arises from O scatterers while the second contains a mixture of As and O scatterers. The increase in the amplitude upon multiplication by k^2 (in going from ϕ_1 to ϕ_3) demonstrates the ability to identify the presence of a higher Z scatterer (As) in this and other compounds. This separation aids in a qualitative interpretation of the data. For well separated peaks, it is possible

to measure their intensities and positions in R-space, or zero all the data except for a given peak and back transform to k-space for further analysis or curve fitting. In addition, signatures (Fourier Transform peaks) of known compounds can be used as models for fitting unknown compounds in R-space. These and other analysis techniques are discussed in the next section.

A Review of Analysis Techniques

The theoretical EXAFS equation

$$\chi(k) = \sum_j \frac{N_j}{kR_j^2} |f(k,\pi)| e^{-2\sigma_j^2 k^2} e^{-R_j/\lambda(k)} \sin\{2kR_j + \alpha_j(k)\} \quad \text{(III.11)}$$

provides the basis for all EXAFS analysis. Lytle, Stern and Sayers (9,22) developed the Fourier Transform technique based on this theoretical result. The Fourier Transform was described in the previous section. Determination of the distance in an unknown compound is performed by comparing its Fourier Transform with the Fourier Transform of a known compound with the same absorber and scatterer. As described before, the scatterer can be identified with some precision by comparing various $\psi_n(R)$ transforms.

Stern et al. (30) reported a method for determination of coordination number and disorder which others have exploited(3). By isolating a single shell in R-space and back-transforming to k-space, the phase and amplitude of the EXAFS for this shell can be calculated. Comparisons with the same calculation from a known compound can provide the coordination number and disorder.

Analysis of the isolated phase and amplitude function also provides an indication of the type of scatterer and its coordination distance (3,31). In addition if there are two or more distances inside the window in R-space, the phase and amplitude will show evidence of the beating of these two frequencies. Martens et al. (32) have proposed this as a method by which the presence of two closely spaced distances in the radial distribution function can be discerned.

Various fitting models have been proposed. Hayes et al. (33) have created "signatures" of known compounds in R-space. These signatures were then used as models for fitting to an unknown compound. If the known compound has only one distance with thermal motion less than the unknown, a thermal motion difference, and distance difference, could be calculated for the unknown. Furthermore, a distribution of distances has been used to model the distribution one expects in disordered metals (34).

A model functional form can be fit to the data in k-space. Several different models have been formulated by Shulman et al. (35), Cramer et al. (4,6,36) and Teo et al. (37).

The phase shift and amplitude functions were obtained empirically from standard known compounds and then applied to the unknown compounds. Identification of scattering types was often possible because the model function for the incorrect scatterer would not fit a given unknown scatterer peak. Thus the unknown scatterer peak could be identified as the type of scatterer whose model function fit best.

Teo et al. (37,38) improved this by making theoretical calculations of the absorber and backscatterer phase shifts and of the backscattering amplitude. Their first method (37) was to parameterize these calculations and use the parameterized functions to fit to EXAFS data. Their second method (38) was to use tabulated values of the theoretical phase and amplitude calculations and then fit to the data. In both methods, a variable E_o was necessary in order to use the theoretical calculations.

Improvements in the model fitting methods have been made by Fourier filtering regions of the data. Fits can then be made to single shells or a limited number of shells in k-space. This minimizes the interdependence of the fitting parameters. For single shells which could be isolated, Teo et al. (38) developed a method for E_o determination which did not require E_o as a fitting variable. $\chi(k)$ with a given E_o was Fourier isolated and the theoretical phase removed from the data. E_o was varied until the phase in k-space had minimum non-linear components, e.g., E_o was used as an adjustable parameter determined by requiring that the experimental and theoretical phases be as similar as possible. It is not the true threshold energy. This is the energy at which the sine component of the transform reaches a peak at the same R value as the magnitude of the Fourier Transform. A transform with the theoretical phase removed is shown in Figure III-17.

E_o Determination

Except for the adjustable E_o described by Teo et al. (38) there

is no clearcut method for determination of E_o . For an initial determination of E_o for our analysis, the threshold energy was estimated as the onset of the continuum which is approximately the edge inflection for a featureless edge or a metal. The threshold energy was also estimated by comparing the appropriate atomic spectroscopy (39) states mentioned in Chapter II, Section A, with the XAS spectrum. Figure 18 shows the atomic states for Se^{+5} which approximate the excited $(As^*)^{+5}$ in the relaxed core approximation. The first atomic state of p-character was plotted coincident with the intense pre-edge peak. The threshold energy used for EXAFS analysis can be estimated as the position of the atomic state continuum in Figure III-18. Note that for this compound, this appears to be the position of the arc-tangent shaped edge onset. These are initial choices of E_o . Examples of the effect of E_o variations on the results are discussed later.

Fourier Transform Analysis

The Fourier Transform method has already been described. The position of the peaks in R-space is determined by fitting a quadratic through the five points around the maximum of each peak. The position and amplitude were determined from these files. Since the curve fitting analysis was a better analysis method, these results are not reported in this work.

Conclusions about the EXAFS spectra were made following a comparison of all the analysis techniques in this work. Discussion of the results of this analysis is contained in Chapters IV and V, with the experimental conclusions. Different k-weighted transforms

$\phi(R)$ where n was varied from -3 to +7 were studied. Different apodization windows and different ranges of data in k-space were transformed for comparative purposes. In addition, by applying an apodization window to the data in R-space, the phase and amplitude function of a single shell can be created in k-space. The R-space window, a modified Hamming function, was a square window centered on a peak tapered in the last 10 to 20% at each end by a cosine function which went smoothly to 0.

Curve Fitting Analysis

Three fitting models were used on the data discussed in this work. We decided that the last method was the best method. Therefore, an extensive discussion of it is included.

The first fitting model, X_{M1}, developed by Tom Eccles (16), is described by equation III.12:

$$X_{M1}(k) = \sum_j A_j \frac{e^{\sigma_j k^2}}{k^{\beta_j}} \sin\left(a_j + b_j k + \frac{c_j}{k}\right) \qquad \text{(III.12)}$$

where $b_j = b' + 2R_j$ and j is the shell index. The parameters σ_j, β_j, a_j and c_j were obtained by fitting to a known compound. Using these parameters on an unknown sample, its distance R_j and EXAFS amplitude A_j were determined.

Both the parameterized theoretical model, X_{M2}, and the tabulated theoretical model, X_{M3}, of Teo et al. (37,38) were used. These models are described by equations III.13 and III.14:

$$X_{M2}(k) = \sum_j \frac{A_j e^{\sigma_j k^2}}{1 + B_j^2 (k - C_j)^2} \sin(\delta_j + \alpha_j k + \beta_j k^2 + \gamma_j k^{-3}) \qquad \text{(III.13)}$$

where $\alpha_j = 2R + \alpha_j$; j is the shell index and B_j, C_j, δ_j, α_j', β_j and γ_j are tabulated by Teo et al. (37).

$$\chi_{M3}(k) = \sum_j A_j e^{\sigma_j k^2} f_j(k) \sin\ (2Rk + \alpha_j(k)) \qquad \text{(III.14)}$$

where $f_j(k)$ and $\alpha_j(k)$ are the tabulated theoretical values (38) for amplitude and phase, respectively, and j is the shell index.

Both models 2 and 3 have an optional variable E_o. As mentioned above, the correct E_o can be determined before fitting for shells which can be distinguished from nearby shells. Further discussion of the use of the third model is included along with the EXAFS results in Chapters IV and V. They have also been discussed by J. A. Kirby (2).

A summary of the analysis approach using the third model follows. Starting with $\chi(k) * k$ with the background removed prepared with a given E_o, the theoretical phase was removed and a Fourier Transform computed. E_o was varied until the sine component peak of the transform occurred at the same R-value as the magnitude peak. Figure III-17 shows a data file prepared in this manner. This method provided an estimate of the E_o which was consistent with the theoretical calculation. The sine component maximum of the Fourier Transform agreed with the magnitude maximum since the oscillating term, with the theoretical phase removed, should be

$$\sin\left[2R\left(\frac{2m}{\hbar^2}(E - E_o)\right)^{\frac{1}{2}}\right]$$

where E is the energy of the x-ray photon, E_o is the electron threshold energy, and R is the shell distance. This E_o value was then used as a starting point for the fitting in k-space.

The fit done is equivalent to a fit in which the theoretical amplitude and phase have been removed from the data using the following equation as a fitting model:

$$F(E) = Ae^{\sigma k^2} \sin(2kR)$$

where $k = \left(\frac{2m}{\hbar^2}(E - E_o)\right)^{\frac{1}{2}}$, and A, σ, R and E_o are variables. F(E) should match $\chi(E)$, the EXAFS data where E is the energy of the incident x-ray. In practice, the theoretical amplitude and phase are included in the model instead of being removed from the data. It makes no difference. For a one-shell fit, the data, $\chi(k)$, are Fourier Transformed and filtered so that only the one shell of interest remains.

An example of the fit and data are plotted in Figure III-19. In order to get an estimate of the error in the fit values for an isolated shell, the least square error $\Sigma(D - F)$ between the data (D) and the fit (F) was plotted as a function of R and E_o in the region surrounding the optimum parameters. For the fit illustrated in Figure III-19, this error plot is plotted in Figure III-20. The contour was drawn for a 100% increase in the error function above the minimum found by the fitting program. The size of this ellipse provides an estimate of the error in the fit. The variation of both E_o and R is necessary since these variables are correlated. The ellipsoidal character of the error plot in Figure

III-20 demonstrates this fact.

The phases of the data and the fit were quite similar. However, the amplitude of the data and the fit did not agree well as Figure III-19 illustrates. This was true for all files. The procedure described below improved on the distance values which were obtained. The total total amplitude function for an isolated shell could be calculated using the Fourier Transform isolation method. It was then removed from the data. The theoretical phase function was also removed from the data. The fitting function now simplied to:

$$F(E) = A \sin (2kR)$$

where $k = \left(\frac{2m}{\hbar^2} (E - E_o) \right)^{\frac{1}{2}}$

We have only 3 variables, A, R and E_o. The amplitude, A, is a variable which should be close to 1.0. This second fit yields an improved estimate of the distance. An estimate of the error can be obtained from an error plot similar to Figure III-20.

In addition, for complicated spectra, several shells can be fit simultaneously to model the data in k-space. Each shell would have the 4 variables A_i, σ_i, R_i and E_{oi}, since the amplitude can only be removed from an isolated shell. The multiple shell fit is used for two spectra in this work.

Figure Captions
Chapter III

III-1 Absorbance of a representative AsF_6^- salt. (b) is an expanded background stripped plot of (a). A crystal "glitch" is printed out.

III-2 Absorbance of a representative AsF_6^- salt. The extrapolated fit used for a pre-edge strip is overplotted.

III-3 Normalized K-shell absorbance (μ_I^*) of $CsAsF_6$. (a) is a scaled plot; (b) is expanded to an arbitrary scale. The smooth lines in (a) and (b) are plots of the extrapolated post-edge function used for edge height normalization. The edge jump is set equal to 1.0 using this function.

III-4 Normalized K-shell absorbance (μ_I^*) for six representative As files.

III-5 Normalized K-shell absorbance (μ_I^*) for six representative As files.

III-6 Normalized K-shell absorbance (μ_I^*), and its first and second derivatives for a representative $RbNH_3$ sample.

III-7 First derivatives of the absorbance of sample D ($C+AsF_5$) shown in figure III-5c. See Text for discussion.

III-8 Second derivatives of the absorbance of sample D ($C+AsF_5$) shown in figure III-5c. See Text for discussion.

III-9 Data (solid line) and synthesized files (dots) plots of normalized absorbance, μ_I^*. The fitted function was synthesized from AsF_3 and graphite/AsF_6^- standard files.

III-10 Normalized K-shell absorbance (μ_I^*) of $CsAsF_6$. (a) is a scaled plot; (b) is expanded to an arbitrary scale. The smooth lines in (a) and (b) are plots of the normalized As K-shell free atom absorbance, μ_M^* (8). This file is representative of the discrepancies between μ_M^* and the measured background function.

III-11 Normalized K-shell absorbance (μ_I^*) of an AsF_3 gas with a very poor post-edge background.

III-12 Comparison of different smoothing average background files on $CsAsF_6$ data. See text for discussion.

III-13 Fourier Transform magnitudes of window functions, showing the attenuation of sidelobes by the use of a Kaiser window function. In the Fourier Transform of actual EXAFS data, the sidelobes would be symmetrically distributed on both sides of each structural peak.

III-14 A family of "Kaiser" apodization windows. The window functions are multiplied by the k-space EXAFS before Fourier transformation to reduce sidelobe intensity.

III-15 $k^2\chi(k)$ plot of EXAFS data for As_2O_3.

III-16 $|\phi_3(R)|$ and $|\phi_1(R)|$ radial distribution function plots of EXAFS data for As_2O_3.

III-17 Normalized K-shell absorbance of AsF_3. (a) is a scale plot; (b) is expanded to an arbitrary scale. For comparison, these Se^{+3} atomic states (11), calibrated such that the $4s^2p$ state is coincident with the white peak, are plotted. Se^{+3} states approximate the $(As^*)^{+3}$ states if the relaxed core approximation is assumed.

III-18 $|\phi_3(R)|$ (dots) radial distribution function plot of $CsAsF_6$ data with theoretical phase removed and E_o adjusted so that the sine component (solid line) of the transform peaks at the same position as the magnitude spectrum $|\phi_3(R)|$. Note that this peak position is the true radial distance.

III-19 $k^3\chi(k)$ plot of $CsAsF_6$ EXAFS data (dots) and the fit (solid line) with the Debeye Waller term, σ, included.

III-20 Error contour plot for the fit in Figure III-19. The contour for a 100% increase in error is drawn.

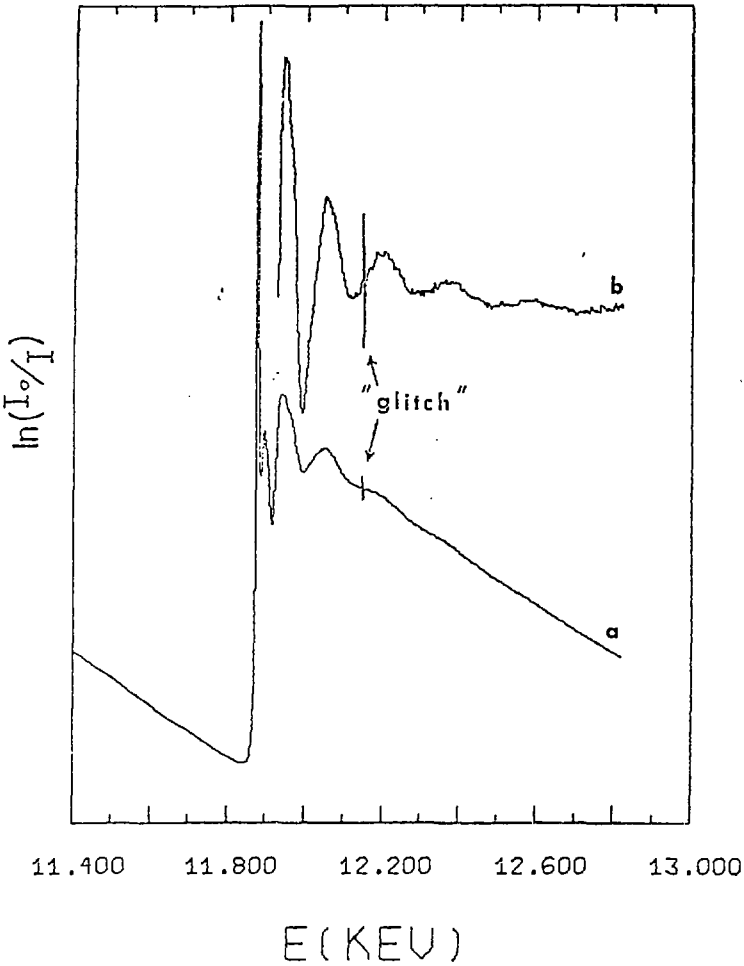

Figure III-1

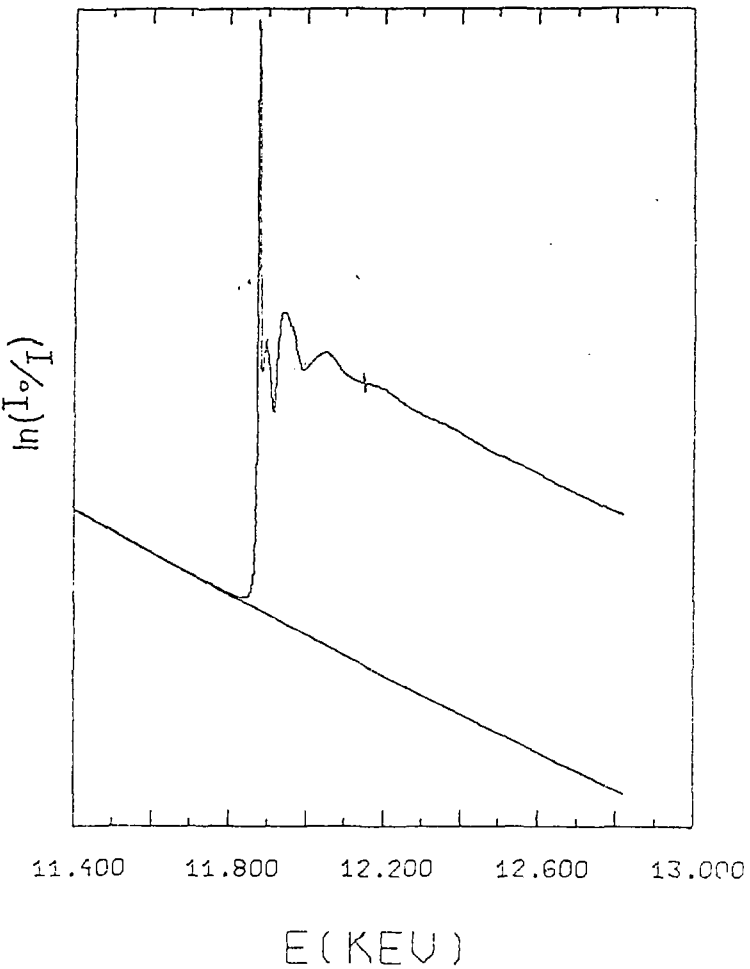

Figure III-2

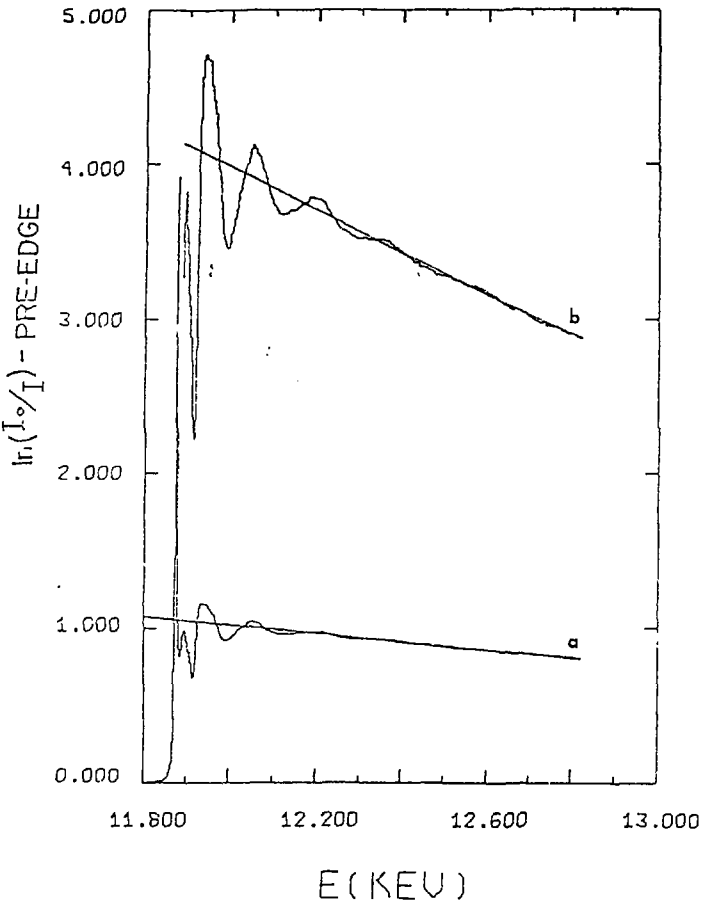
5.000
4.000
3.000
2.000
1.000
0.000
ln(I°/I) - PRE-EDGE
b
a
11.800
12.200
12.600
13.000
E(KEV)

Figure III-3

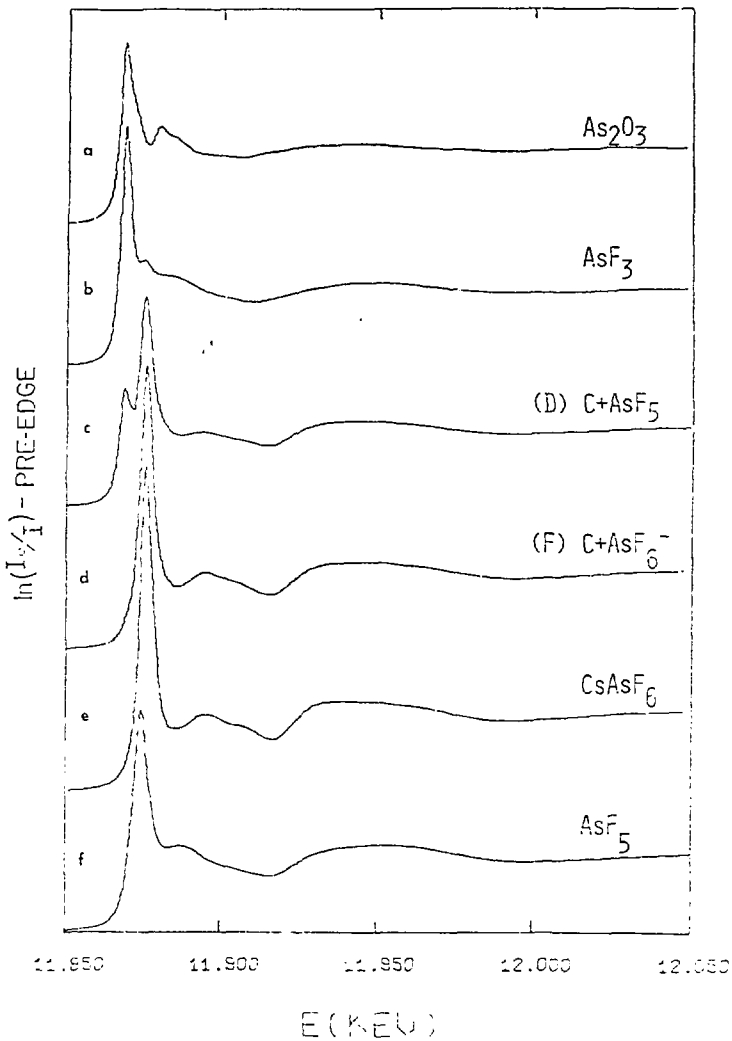
a
b
c
d
e
f
As_2O_3
AsF_3
(D) $C+AsF_5$
(F) $C+AsF_6^-$
$CsAsF_6$
AsF_5
$\ln(I_0/I)$ - PRE-EDGE
11.850
11.900
11.950
12.000
12.050
E(KEV)

Figure III-4

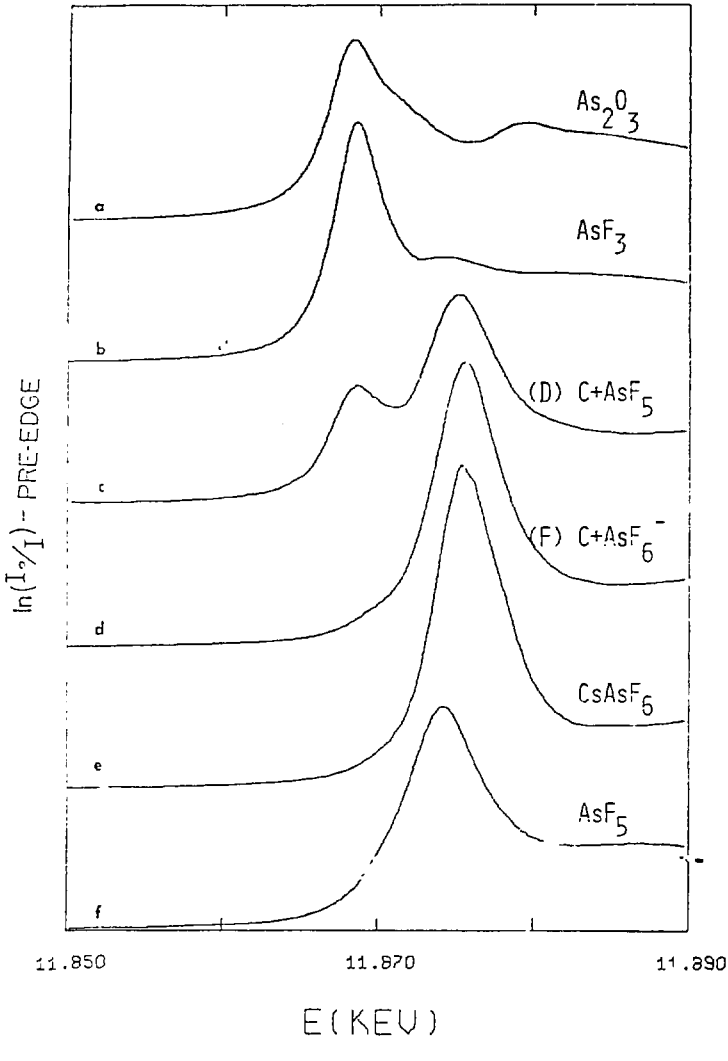
As_2O_3
AsF_3
(D) $C+AsF_5$
(F) $C+AsF_6^-$
$CsAsF_6$
AsF_5
a
b
c
d
e
f
$\ln(I_0/I)$ - PRE-EDGE
11.850
11.870
11.890
E(KEV)

Figure III-5

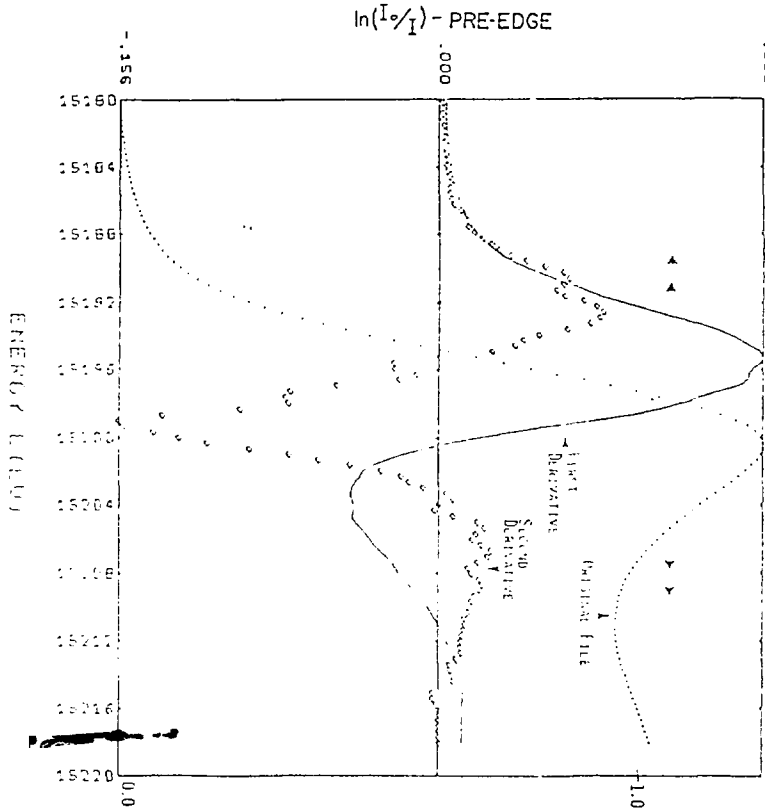
ln(I°/I) - PRE-EDGE
.156
.000
-.156
1.0
0.0
15160
15164
15168
15172
15176
15180
15184
15188
15192
15196
15200
15204
15208
15212
15216
15220
ENERGY (eV)
FIRST DERIVATIVE
SECOND DERIVATIVE
PRELIMINARY FIT

Figure III-6

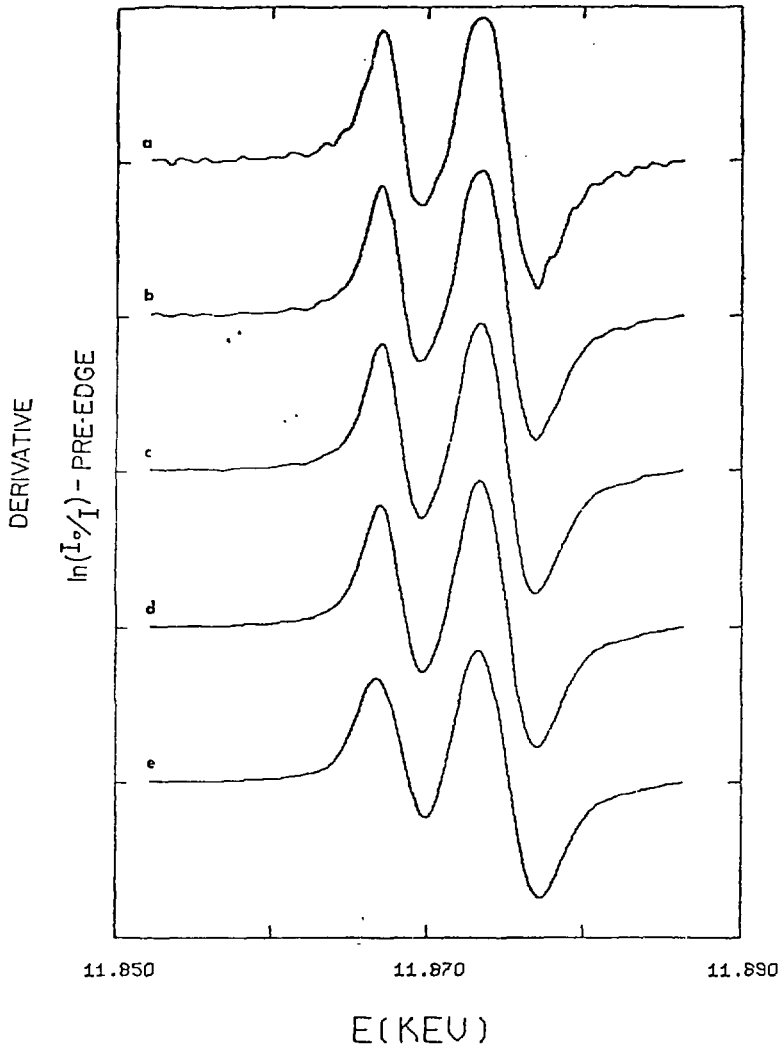

Figure III-7

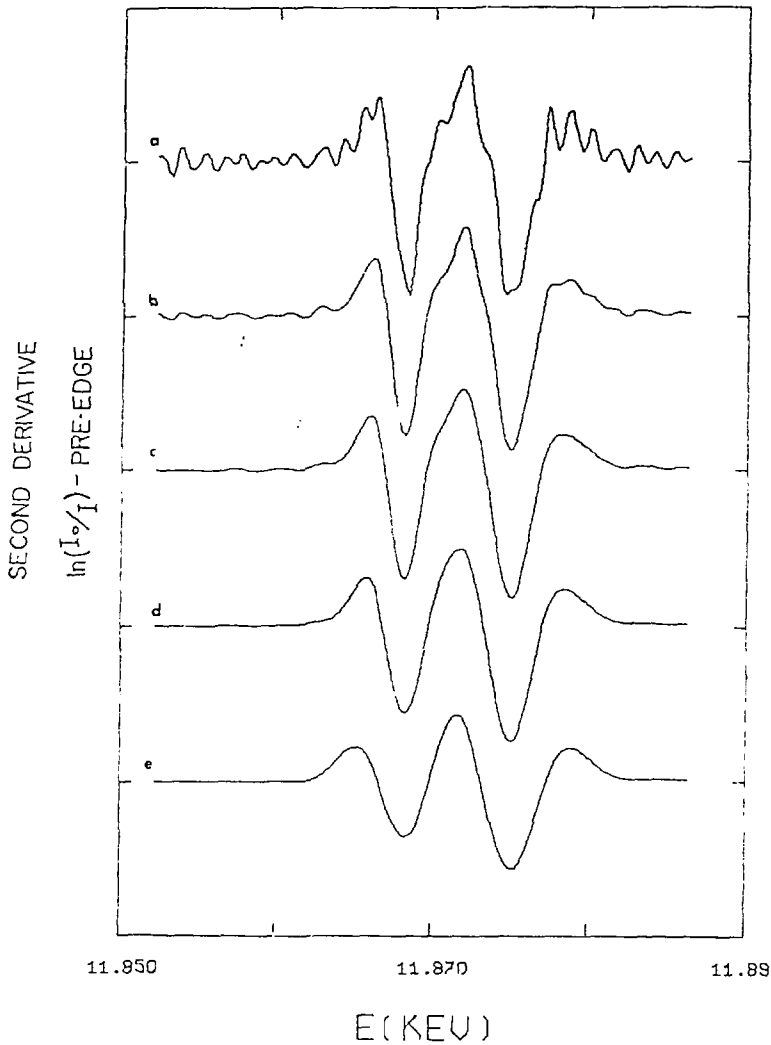
a
b
c
d
e
SECOND DERIVATIVE
ln(Io/I) - PRE-EDGE
11.850
11.870
11.890
E(KEV)

Figure III-8

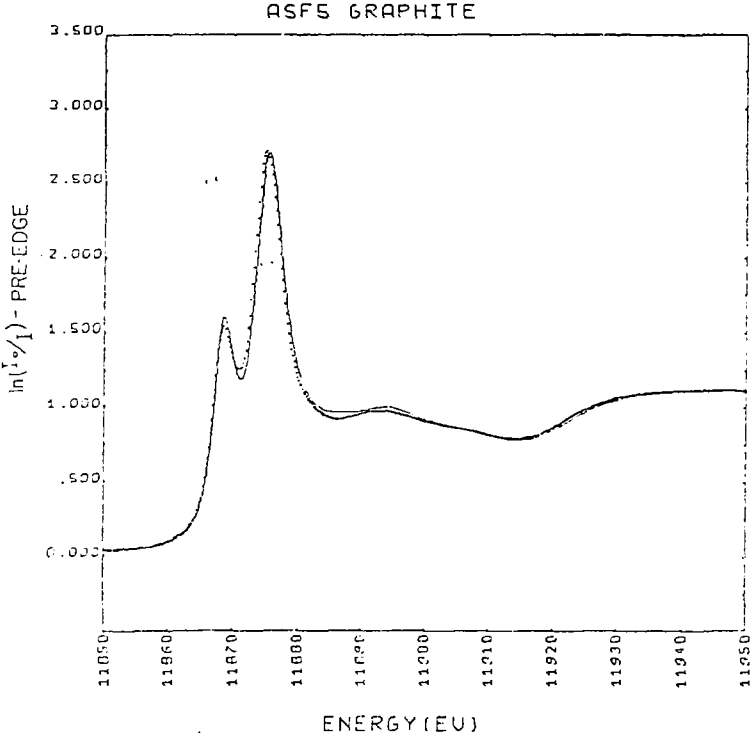
ASF5 GRAPHITE
3.500
3.000
2.500
2.000
1.500
1.000
.500
0.000
ln(I°/I) - PRE-EDGE
11850
11860
11870
11880
11890
11900
11910
11920
11930
11940
11950
ENERGY(EV)

Figure III-9

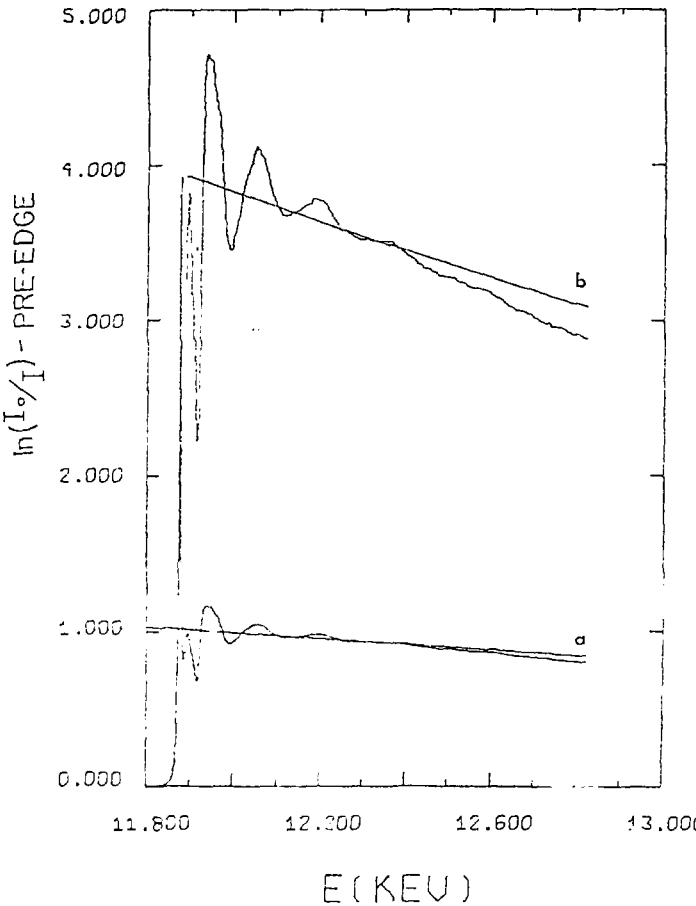

Figure III-10

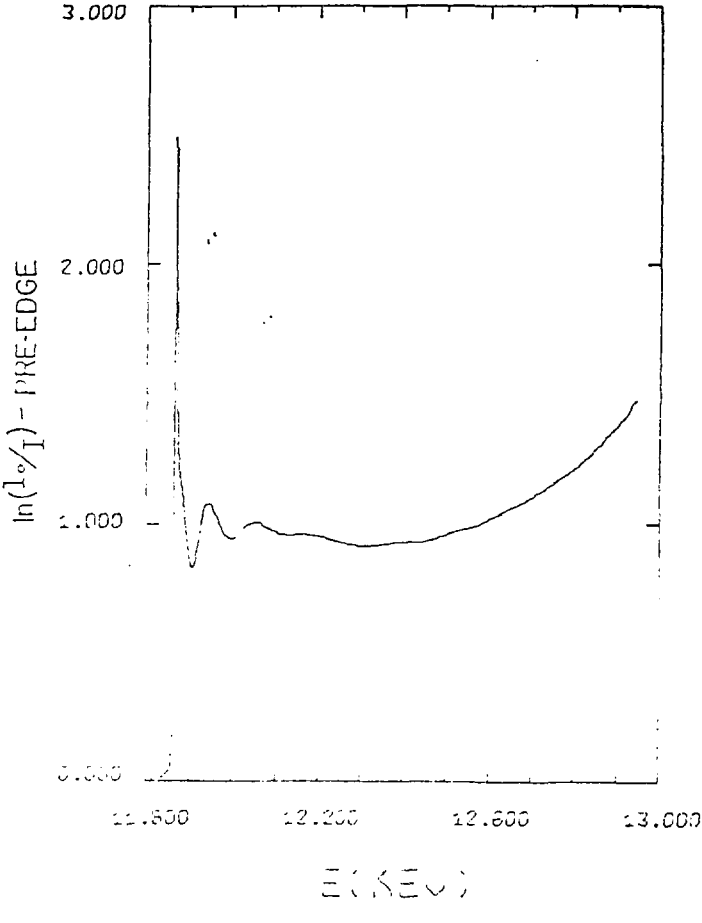

Figure III-11

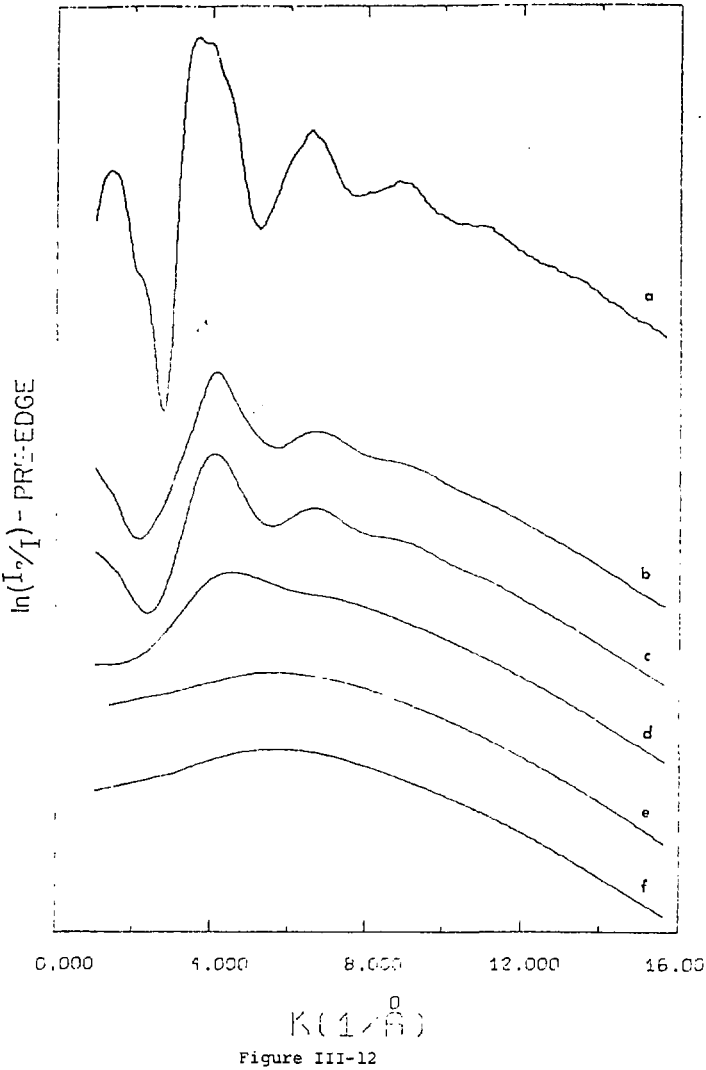

Figure III-12

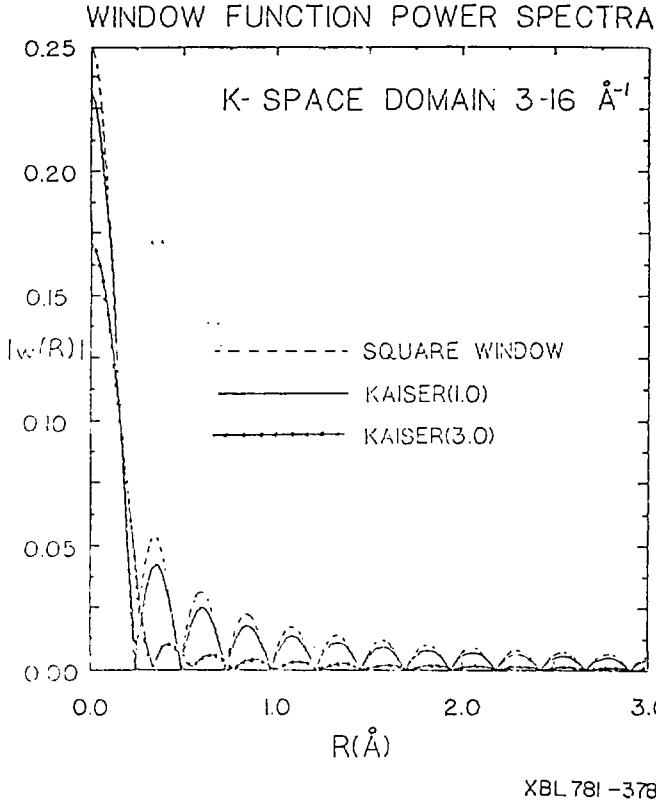

Figure III-13

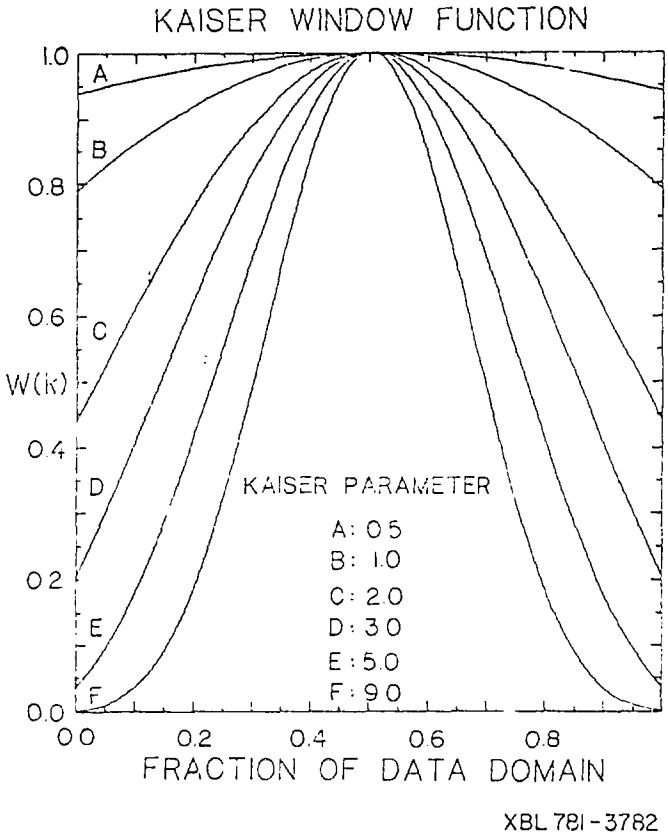

Figure III-14

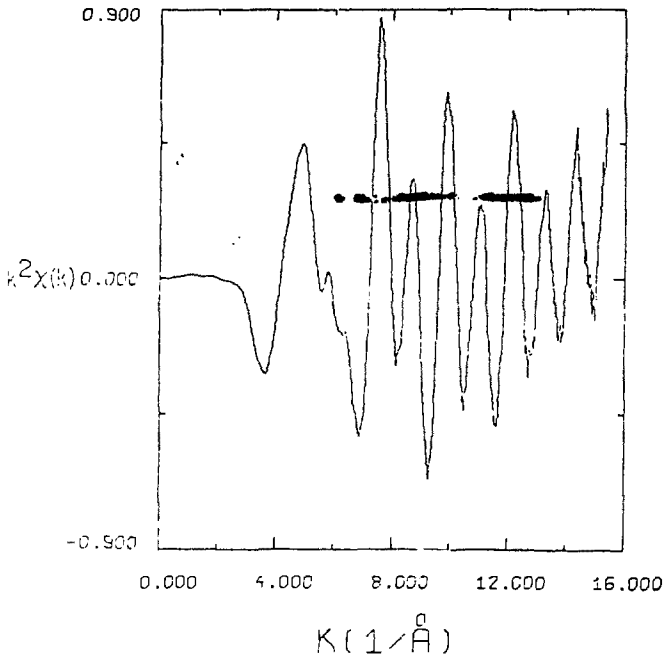

Figure III-15

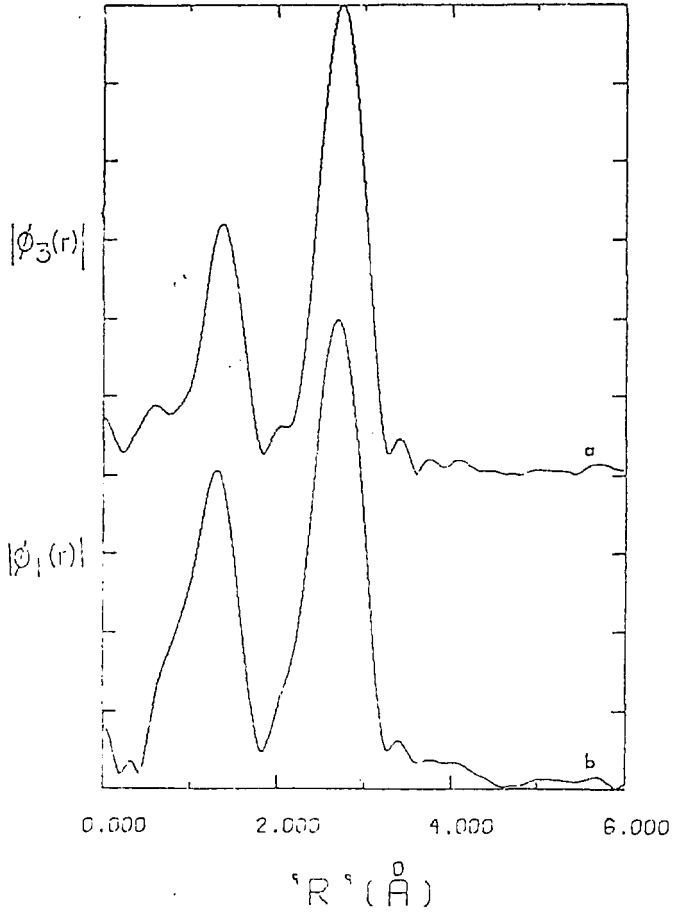

Figure III-16

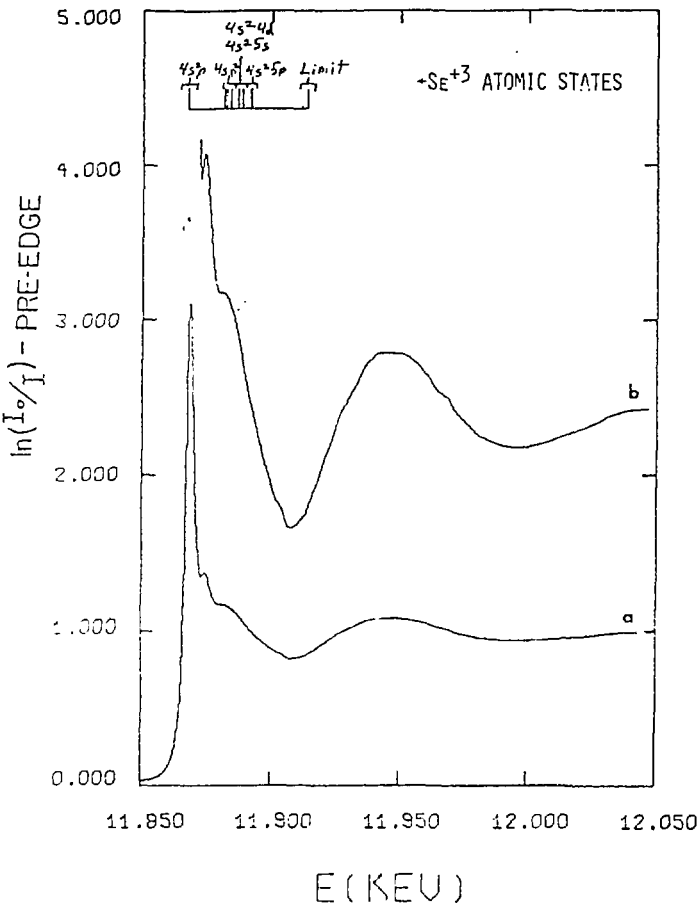

Figure III-17

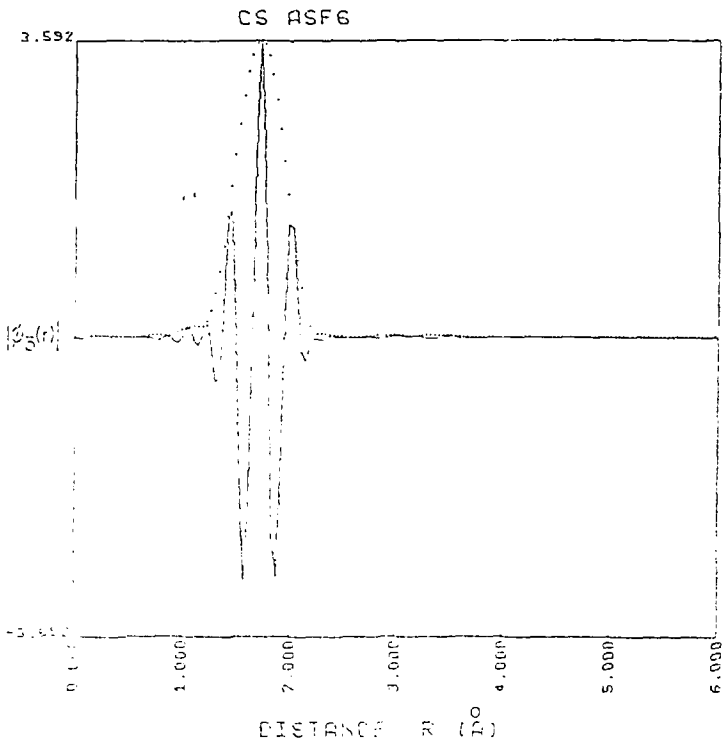

Figure III-18

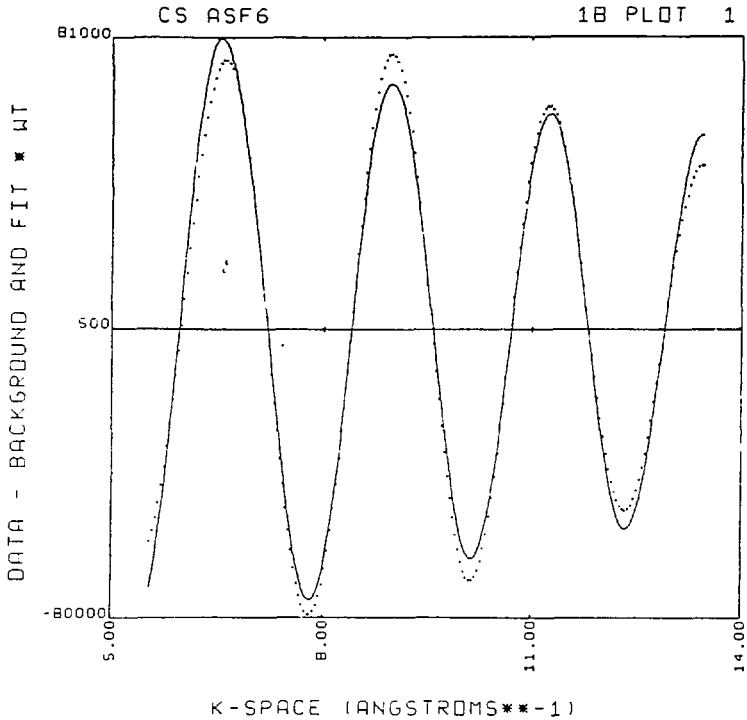

XBL 798-10752

Figure III-19

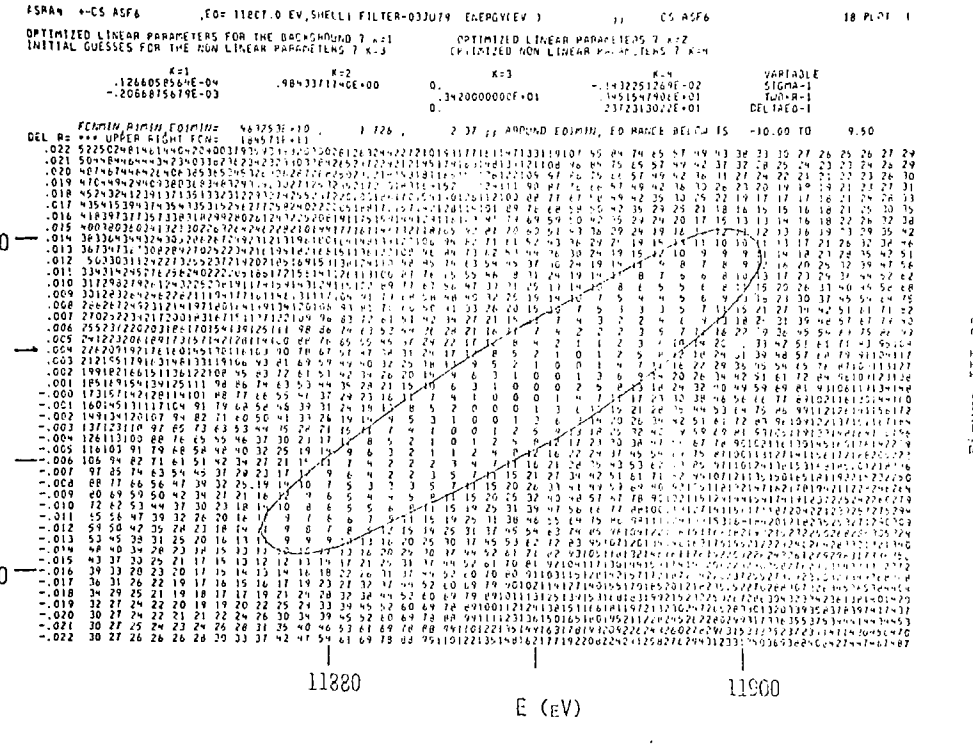
FSRAN 4-CS ASF6
CS ASF6
18 PLOT 1
OPTIMIZED LINEAR PARAMETERS ? K=1
INITIAL GUESSES FOR THE NON LINEAR PARAMETERS ? K=3
OPTIMIZED LINEAR PARAMETERS ? K=2
OPTIMIZED NON LINEAR PARAMETERS ? K=4
K=1
K=2
K=3
K=4
VARIABLE
SIGMA-1
TAU-1
DELTAEO-1
.126605864E-04
-.206887569E-03
.984337114E+00
-.143225126E-02
.342000000E+01
.237231302E+01
EDMIN, BMIN EDMIN=
1.740
1.710
R (A)
11880
11900
E (EV)
Figure 22

References
Chapter III

1. J. P. Smith; Ph. D. Thesis, University of California, Berkeley (1978).

2. J. Kirby; Ph. D. Thesis, University of California, Berkeley (in preparation).

3. S. H. Hunter; Ph. D. Thesis, Stanford University (1977).

4. S. P. Cramer; Ph. D. Thesis, Stanford Univeristy (1978).

5. W. E. Blumberg; private communication.

6. T. K. Eccles; Ph. D. Thesis, Stanford University (1978).

7. International Tables for X-ray Crystallography III, ed., K. Lonsdale, et al., Kynoch, Birmingham, England (1962), Sec. 3.2.

8. W. H. McMaster, N. Kerr Del Grande, J. H. Mullet and J. H. Hubbell; Compilation of X-Ray Cross Sections, UCRL-50174, Sec. II Rev. I, Nat'l. Technical Information Service, Springfield, Virginia (1969).

9. F. W. Lytle, D. E. Sayers and E. A. Stern; Phys Rev. B (1975) 11, 4825-4835.

10. N. K. Del Grande, in Proceedings of the International Symposium on X-ray Spectroscopy and Electronic Structure of Matter, ed., A. Faessler, University of Munich Press, Munich (1973), 183.

11. T. M. Hayes; private communication.

12. J. Jaklevic, J. A. Kirby, M. P. Klein, and A. S. Robertson; Solid State Comm. (1977) 23, 679-682.

13. R. G. Shulman, Y. Yafet, P. Eisenberger and W. Blumberg; Proc. Nat'l. Acad. Sci.-USA (1976) 73, 1384-1388.

14. U. C. Srivastava and H. L. Nigam; Coord. Chem. Rev. (1972-1973) 9, 275-310.

15. L. G. Parratt, Phys Rev. (1939) 56,295.

16. V. W. Hu, S. Chan, and G. S. Brown; Proc. Nat. Acad. Sci USA (1977) 74, 3821-3825.

References, Chapter III, continued

17. B. K. Teo, P. Eisenberger, and B. M. Kincaid; J. Am. Chem. Soc. (1978) 100, 1735-1744.

18. S. P. Cramer, T. K. Eccles, F. Kutzler, K. O. Hodgson and S. Doniach; J. Am. Chem. Soc. (1976) 98, 8059-8069.

19. B. K. Teo, P. Eisenberger, and B. M. Kincaid, J. Am. Chem. Soc. (1978) 100, 1735-1744.

20. F. W. Lytle; private communication.

21. S. P. Cramer; private communication.

22. E. A. Stern, D. E. Sayers, F. W. Lytle; Phys. Rev. B (1975) 11, 4836-4846.

23. E. A. Stern, Phys. Rev. B (1974) 10, 3027.

24. J. F. Kaiser; System Analysis by Digital Computer, F. F. Kuo and J. F. Kaiser, ed., J. Wiley and Sons Inc., N.Y. (1966).

25. T. M. Hayes, P. N. Sen and S. H. Hunter; J. Phys. C: Solid State Phys. (1976) 9, 4357-4364.

26. D. Sayers; private communication.

27. R. B. Blackman and J. W. Tukey, The Measurement of Power Spectra, Dover Publications, Inc., N.Y. (1958).

28. R. G. Shulman, Y. Yafet, P. Eisenberger and W. E. Blumberg; Proc. Nat'l Acad. Sci.-USA (1976) 73, 1384-1388.

29. G. Martens, P. Rabe, N. Schwentner and A. Werner; Phys. Rev. B (1978) 17, 1481-1488.

30. E. A. Stern, D. E. Sayers, and F. W. Lytle, Phys. Rev. B (1975) 11, 4836.

31. G. Martens, P. Rabe, N. Schwentner, and A. Werner; Phys.Rev.B (1978) 17, 1481-1488.

32. G. Martens, P. Rabe, N. Schwentner, and A. Werner; Phys.Rev. Lett. (1977) 39, 1411-1414.

33. T. M. Hayes and S. H. Hunter; Proc. of Symp. on Structure of Non-Crystalline Materials, Cambridge, England (1976).

References, Chapter III, continued

34. T. M. Hayes, J. B. Boyce, and J. L. Beeby; J. Phys. C.: Solid State Phys. (1978) 11, 2931-2937.

35. R. G. Shulman, P. Eisenberger, W. E. Blumberg, and N. A. Stombaugh. Proc. Nat. Acad. Sci.-USA (1975) 72, 4003.

36. S. P. Cramer, T. K. Eccles, F. Kutzler, K. O. Hodgson, and S. Doniach; J. Am. Chem.Soc. (1976) 98,8059.

37. B. K. Teo, P. A. Lee, A. L. Simons, M. Eisenberger, and B. M. Kincaid; J. Am. Chem. Soc. (1977) 99, 3854.
P. A. Lee, B. K. Teo, A. L. Simon; J. Am. Chem. Soc. (1977) 99, 3856.

38. B. K. Teo and P. A. Lee; J. Am. Chem Soc. (1979) 101, 2815.

39. C. E. Moore; Atomic Energy Levels, Vol. II (1952) National Bureau of Standards (U.S.) Circular 467.

Chapter IV

AS K-EDGE XAS EXPERIMENTS

In this chapter the XAS experiments performed on As-F compounds, in particular the As-F graphite compounds, are discussed.

A. Sample Preparation and Experiment

Chemical Preparation of Graphite Compounds

Five samples of graphite AsF_5 were prepared. In addition, a separate sample was prepared from graphite AsF_5 by exposing this sample to F_2 gas. Since these intercalates are unstable in all moist air, all samples were handled in the dry atmosphere of an Atmospheres Drilab when they were not attached to a vacuum line.

The basic preparation used for graphite AsF_5 is simple to describe (1). Powdered graphite was obtained from highly oriented pyrolytic graphite (HOPG) by shaving a fine powder off the block of graphite. Particles bigger than a certain size were rejected through use of a sieve. The graphite powder was placed in a clean quartz tube which was pumped and flamed for one to two days at vacuum. The AsF_5 gas was then added at about 500 torr and the reaction commenced. The reaction was allowed to continue for different amounts of time (3 to 24 hours). The AsF_5 pressure was removed and the sample exposed to vacuum for about 5 minutes. One atmosphere of N_2 was then placed over the sample. Except for sample G, a composition between

$C_{10}AsF_5$ to C_8AsF_5 was obtained. For sample G, a stoichiometric amount of AsF_5 was added in order to achieve a composition $C_{16}AsF_5$. The details of the preparation of each sample are presented below.

Samples A and B were placed separately into sample cells after the AsF_5 graphite was divided into two portions. 114 mg of graphite was exposed to AsF_5 for 24 hours as previously described. Gravimetry indicated a composition of $C_{9.5}AsF_5$. A powder pattern (001) showed a first stage material with C = 8.08 Å. The sample was stored for two weeks in a sealed tube before the XAS samples were made. The data were taken one week later.

Samples A and B were both mixed with powdered teflon and pressed into the slot of the sample holder shown in Figure IV-1. This cell is described later.

The same starting material was used for samples C and D. 128 mg of powdered graphite was exposed to AsF_5 for 3 hours in the manner described above. Gravimetry indicated a composition of $C_{10.8}AsF_5$. A portion of this was used to make sample D.

The rest of this sample was returned to the vacuum line and the N_2 was pumped out. F_2 gas was added at about 200 torr and maintained at that pressure for 7 hours. The F_2 was then pumped off. It was predicted that the sample would now be graphite AsF_6^- instead of graphite AsF_5. The weight increase obtained was slightly larger than predicted.

Samples C and D were both poured into the slot of the sample holder shown in Figure IV-1. They were not pressed. The samples were run the day after being prepared.

Sample E was prepared from 150 mg of graphite with an AsF_5 exposure time of 36 hours. The sample cell was loaded within two hours after removal from the AsF_5 gas. Gravimetry indicated a composition of $C_{7.75}AsF_5$. A carbon analysis two days later gave $C_{11.5}AsF_5$. The sample was mixed with dry powdered teflon and pressed into a 1¼" pellet press in a Drilab.

Sample G was prepared so that $C_{16}AsF_5$ would be made. 184 mg of powdered graphite was exposed to just less than a stoichiometric amount of AsF_5. After 3 hours, the reaction seemed complete. Gravimetry indicated a composition of $C_{18.8}AsF_5$. A little more AsF_5 was added and the sample was left overnight. The final weight indicated a composition of $C_{16.2}AsF_5$. The sample was mixed with powdered teflon and pressed into the 1¼" pellet die.

Graphite AsF_6 was made by adding O_2AsF_6 to the powdered graphite with SO_2ClF as a solvent for the two solids (1). The sample was maintained at -78° C for two days. The SO_2ClF and excess O_2AsF_6 were then removed.

Sample H was the first AsF_6 graphite compound made. 108 mg of powdered graphite was reacted with O_2AsF_6 as described above. Gravimetry indicated a composition $C_{9.5}AsF_6$. The sample was mixed with powdered teflon and pressed into the slot of the sample cell shown in Figure IV-1.

For sample F, 121 mg of powdered graphite was reacted in the manner described above. Gravimetry showed a composition of $C_{12}AsF_6$. The sample was mixed with powdered teflon and pressed into the 1¼" pellet die.

Chemical Preparation of Other Solid Standards

As_2O_3 was used as an energy reference for every run. Reagent grade As_2O_3 was mixed with powdered teflon and pressed into the 1¼" pellet die. The sample was then mounted in a plastic holder.

$CsAsF_6$ and $NaAsF_6$ were made by reacting either CsF or NaF with AsF_5 gas. The samples were characterized by x-ray powder diffraction. The $CsAsF_6$ was mixed with powdered teflon and pressed into the sample slot of the sample cell in Figure IV-1 while $NaAsF_6$ was pressed into the 1¼" pellet press. O_2AsF_6 is a standard reagent material. The preparation techniques for the other reference compounds have been described elsewhere. Since the details of their preparation are not important for the results of this thesis, only the references which describe the compound preparation are given. $C_{10}F_8AsF_6$ (2), $C_6F_6As_6$ (2), $XeFAsF_6$ (3) and $Xe_2F_3AsF_6$ (4) were all prepared. Each sample was mixed with powdered teflon and pressed into the slot of the sample cell shown in Figure IV-1.

Chemical Preparation of Gas Standards

AsF_5, supplied by Ozark-Maholing, was purified at -78° C with a brief pumping. Its IR spectrum showed no impurities. It was loaded into a standard 7 cm IR cell in which the windows were 10 mil teflon. The IR cell is shown in Figure IV-2. The interior of the cell had been pumped, leak-tested and exposed to F_2 gas prior to loading the AsF_5. 380 torr of AsF_5 was first added. Then 380 torr of N_2 was added so that the total pressure would be 1 atmosphere.

AsF_3 gas was made by exposing an excess amount of As metal to a quantity of AsF_5 gas. At -63° C, the residues were pumped off. The

IR showed pure AsF_3 , with a minor amount of SeF_4. Since this would not affect the XAS experiment, it was ignored. Vapor pressure of AsF_3 (160 torr) was added to another identical IR cell. 600 torr of N_2 was then added so that total pressure was 1 atmosphere.

Sample Cell and Dewar for Solid Samples

For all the solid samples except the most recent samples of $NaAsF_6$ and the graphite samples E, F and G, the sandwich sample as shown in Figure IV-1 was assembled and placed in another sealed plastic bag inside the Drilab. The low temperatures were obtained by placing the cell in a styrofoam box into which the boiloff from a liquid nitrogen dewar was vented. A heater in the dewar was manually controlled in order to maintain the temperature of a thermocouple in the atmosphere inside the styrofoam dewar.

For the most recent samples ($NaAsF_6$ and graphite samples E, F and G), the pressed pellet was in the sandwich cell in place of the middle teflon spacer. The sample cell was then assembled and mounted in a leak-tested dewar inside the Drilab. The dewar is the standard LN_2 dewar provided by SSRL. For low temperatures, the dewar was filled with LN_2. The temperature of the sample was measured via a thermocouple placed under one of the assembly screws of the sample cell shown in Figure IV-1.

Experimental Runs

Experimental runs were conducted on seven days. AsF_3 and AsF_5 gas were each run twice with comparable results. The compounds which were run by pouring or pressing the sample into the slot in the sample cell were the first samples for which data were obtained. The gas

samples were later done for comparison. The pressed pellets and additional gas samples were run last.

One persistent problem in analyzing the data is that some of the data were taken on a different beam line with the poorer resolution 111 Si crystal mounted. Most of the data were taken with the 220 Si crystal on the same beam line. From one day to another the resolution was fairly similar for the same crystal on the same beam line. Luckily, these problems affect only the XAES data and not the EXAFS data. The samples which were run with the 111 crystal were graphite sample C which is $C/AsF_5 + F_2$, one AsF_3 sample, and one AsF_5 sample. Other AsF_3 and AsF_5 scans exist on the 220 crystal.

Scan Parameters

The standard scan used to obtain data is described here. From about 420 eV to 20 eV below the onset of absorption, points were taken at 20 eV intervals. From 20 eV below the onset of the absorption to 40 eV above that energy, points were taken at 0.4 eV intervals for most runs. For AsF_3, AsF_5, $NaAsF_6$, and graphite samples E, F, and G, data were taken at 0.2 eV intervals. In addition, for all these samples except sample G, the 0.2 eV edge scan was extended to 90 eV above the onset of absorption. From about 40 eV to 1140 eV above the onset, data were taken at 3.0 eV intervals for all samples except the 6 samples just mentioned above. For these 6 samples, data were taken at 310 eV intervals up to 640 eV above the edge and at 6.0 eV intervals from there to 1300 eV above the edge.

B. XAES Analysis

Analysis of the edge features included both a qualitative comparison of the edge features as well as a quantitative assignment of their positions and intensities.

Figure IV-3 shows a raw spectrum plot of the absorbance, μx, for a representative AsF_6^- salt. Several spectra taken of this sample have been added.

As discussed in Chapter III, a pre-edge strip is done across the 350 eV of data below the onset of absorption. The function subtracted is overplotted in Figure IV-3. Formally, only the absorption from the As K-shell remains after the subtraction. In practice, small residual backgrounds remain from other edges and from detector backgrounds. These, however, are small in the 40 eV to 100 eV of data which are studied for XAES analysis. For EXAFS analysis, a separate background is removed and any remaining residual background does not affect the data. The data files are now normalized to an edge height of 1.0. Using the formalism of Chapter III, the function is now μ_I^* (E) where E is the photon energy. For the same sample, μ_I^* is plotted in Figure IV-4.

Extended Edge Plots

An extended edge region plot for six samples is shown in Figure IV-5. An expanded plot of the latter portion of these files is shown in Figure IV-6. The six samples chosen are representative of the data taken. The strong absorption lines, typically called white lines, near 11,870 eV are due to transitions into empty molecular orbitals which have p-symmetry. These lines and their meaning will be discussed

more below.

As discussed in Chapter II, if we a[illegible] that these lines are transitions to pure atomic states of As^{+3} for AsF_3, and of As^{+5} for AsF_6^- and other As^{+6} compounds, we would predict the onset of the continuum to be at 11912 eV for As^{+3} and 11943 for As^{+5}. Figures IV-5 and IV-6 show that the inflection point of the arc-tangent shaped onset of the continuum appears to be around 11920 eV for all samples. We do not expect excellent agreement, particularly because the transitions are transitions to molecular orbitals and not to atomic orbitals. Furthermore, for As^{+5} the radius of the 4p atomic orbital is larger than the accepted radius of As^{+5}. For these reasons, we would not expect this p-state to lie 67 eV below the onset of the continuum as predicted from the atomic states. The molecular orbital may be a mixture of both the 4s and 4p orbitals of As^{+5} in addition to the orbitals of F^-.

In Figures IV-5 and IV-6, other states can be observed between the strong absorption peak near 11870 eV and the rise in absorption near 11920 eV. These appear to be transitions to other molecular orbital states with p-symmetry. There is no indication of a 1s - 4p transition which would occur at 11,861 eV, if we assume the transitions are to atomic states, in the As^{+5} compounds in Figure IV-5 or in any of the other As^{+5} samples run. In an octahedral environment, we would not expect to see this line. As mentioned by Shulman et al. (5) such a transition is allowed only if there is vibronic mixing of states. This occurs in tetrahedral but not in octahedral environments.

The last half of Figures IV-5 and IV-6 (beyond 11950 eV) is the beginning of the EXAFS region of the data. As discussed before, we no longer have one electron transitions to bound states in this region. Transitions occur into a free electron continuum. This region will be discussed in the next section of this chapter.

For all graphite/AsF_5 compounds including the one C/AsF_5 compound in Figures IV-5 and IV-6, it appears that the edge spectra are a sum of fractions of AsF_3 and AsF_6^- spectra. This is particularly true around the strong absorption peak as indicated in Figure IV-7. This is exactly what we predicted.

We expected that the reaction

$$\text{Graphite} + 3AsF_5 \rightleftarrows \text{Graphite}^{++} + 2AsF_6^- + AsF_3 \qquad \text{(IV.1)}$$

would occur. For this reason, the narrow edge region from 11850 to 11890 eV will be discussed below. In addition the positions and intensities of these peaks in the second derivative spectra will be tabulated as support for this hypothesis. Finally, the results of a synthesis of the graphite/AsF_5 spectra will be presented. In this program, the varying proportions of the standard files AsF_3 and AsF_6^- were added until a best fit to the data was obtained.

In Figures IV-5a, 6a, and 7a, the As_2O_3 spectrum is plotted. Note that the As^{+3} peak appears at the same place as it does in AsF_3. A quantitative comparison of this agreement is presented in Table IV-I. The same is true for the apparent onset of the continuum. However, note that there are differences in the position and intensity of the other transitions. This is what would be expected, since the

site symmetry of As_2O_3 is different than AsF_3.

Narrow Edge Plots

In Figure IV-7, a narrow edge plot (11850 to 11890 eV) is shown for each of the six samples illustrated in Figures IV-5 and IV-6. Figure IV-8 shows plots of all the graphite/AsF_5 compounds which were run under similar monochromator resolution. Observe that all scans appear to be a sum of fractions of AsF_3 and AsF_6^- spectra. Only one major difference occurs. The intensity of the AsF_3 line varies with respect to the intensity of the AsF_6^- line.

This difference is a problem. One supposition is that different compounds were formed with different amounts of As^{+3}. Only one sample, sample D, had a significantly different size of As^{+3} peak. This compound is the only compound which was not pressed before the data were taken. The powdered pieces of graphite became ordered when they were pressed. Low angle scattering experiments performed by J. V. Acrivos (6) on the graphite samples E, F and G showed that the pellets were extremely well ordered with the c-axis of graphite perpendicular to the plane of the pellet. Upon powdering the pellet, the orientation again became random (6) .

Since the polarization of the x-ray beam was oriented within the plane of the pellet and perpendicular to the direction in which the samples were pressed, all graphite sample scans except samples C and D were of oriented samples. If the AsF_3 were oriented in the graphite such that the empty 4p orbital states were aligned mainly along the c-axis, then the As^{+3} 1s $\rightarrow$ 4p transition would be reduced in intensity. This would not be expected for the As^{+5} 1s $\rightarrow$ 4p transition

in AsF_6^- due to its octahedral symmetry. Quantitative results presented later in Table IV-I show that the relative intensity of the As^{+3} peak in the compounds in which it appears to be a small shoulder is actually 0.25 of AsF_6^- in that compound. If the oxidation-reduction in equation IV.1 were complete, one would expect this to be 0.50. So the peak is only a factor of 2 smaller than expected. Templeton et al. (7) have noticed this effect in a single crystal of Vanadium Oxide. Rotation of the crystal enhanced or eliminated a similar white peak in their data.

Of course, none of this proves that the variation in the size of the As^{+3} peak is due to orientation effects. It is, however, a reasonable explanation. The peak is not an As_2O_3 peak. If any of the samples had been exposed to air, there would have been As_2O_3 present. The EXAFS region of the data discussed in the next section shows conclusive evidence, however, that there is no As_2O_3 in the sample. The remaining possible explanation is that this intensity variation is due to true differences in the amount of As^{+3} in the samples. No conclusions about this intensity can be made from this XAES data alone.

Figure IV-9 shows the narrow edge plots of five different AsF_6^- compounds. Note that all of the peaks have maxima at the same energy value. The positions of these peaks are listed in Table IV-Ia. The peak positions are the same for all AsF_6^- compounds, the insulators and the metallic graphite/AsF_6^-. The As^{+5} peak positions of the metallic graphite/AsF_5 compounds appear to be the same as the others.

These positions are listed in Table IV-Ib. This implies that the orbitals of the As atom are not directly involved in the creation of the bands in the metallic graphite intercalates.

Figure IV-10 shows the second derivatives of seven representative files. The first six files are the same files illustrated in Figures IV-5, IV-6, and IV-7. Figure 10g is C/AsF_5 , sample E. The derivatives were calculated by first fitting a cubic polynomial over the data points within 1.5 eV on either side of every data point. The derivative for each point plotted is estimated by taking the analytical derivative of each fit. One can clearly see the positions of each of the peaks in the second derivative. Both AsF_5 graphite compounds have two peaks, one at the position of the AsF_3 gas peak and the other at the position of the AsF_6^- peak. The AsF_5 gas peak is about 1 eV below the AsF_6^- peak. Quantitative results are presented in Table IV-I. In order of increasing energy of white peaks, the three standards are AsF_3, AsF_5, and AsF_6^-. If one estimates the amount of charge present on the As atom, one would expect that the peak order would be AsF_3, AsF_6^-, AsF_5. Since this is not the case, it is evident that trigonal bi-pyramidal symmetry of the AsF_5 molecule must require some mixing of the As 4s and 4p orbitals for the bonding to occur. The 4s orbital in the As^{+5} ion is about 15 eV below the 4p orbital. A mixing of these orbitals would lower the position of the peak seen in the edge spectrum.

Quantitative Results

As a further comparison of the edge results the positions of the

peaks in the second derivative spectrum are listed in Table IV-I. A summary of these data are presented in Table IV-II. For the graphite/AsF_5 compounds, the intensity of the As^{+3} peak with respect to the As^{+5} peak is also listed. These numbers were extracted from second derivatives similar to the derivatives in Figure IV-10.

For the graphite/AsF_5 compounds, the relative intensity is also listed in Table IV-1 as calculated from a data synthesis program. The fraction of AsF_3 and graphite/AsF_6^- was varied until a best fit to the unknown was obtained. An example of a fit and the observed data are shown in Figure IV-11.

Three points are worth noting with regard to this data synthesis. The intensities of the peaks calculated seemed insensitive to the energy range of the fit. Several fits were done with the same results. One was done over the range 11860 to 11890 eV and the other over the energy range 11848 to 11968 eV. In addition, $NaAsF_6$ was also used as a standard. It did not work well as a standard in the energy range above 11890 eV. There appear to be some differences in the higher energy transitions between $NaAsF_6$ and the graphite compounds. The graphite/AsF_6^- is a better standard. Finally, the numbers derived from these fits can only be used to indicate the presence of AsF_3 and not to indicate its quantity since a graphite/AsF_3 standard does not exist.

Finally, fits were processed with AsF_5 gas as a third standard. Its contribution to the spectrum was usually less than 4% of the main peak and often negative. Since the estimate of error is around 3%,

this is a negligible contribution to the fit. The two cases in which the AsF_5 contribution is larger than 4% are both low resolution spectra. There is no hint of a third peak in the second derivative spectrum, but the narrowness of the AsF_6^- and AsF_3 standards causes a sizable difference between the unknown and the fitted file when only AsF_3 and AsF_6^- are used as standards. The addition of AsF_5 as a standard simply fills in the sides of the AsF_3 and the AsF_6^- peaks which results in a better fit. Therefore, this AsF_5 contribution is not indicative of an AsF_5 peak in the data.

The average values of the peak positions and their estimated errors are listed in Table II. The data show that AsF_5 is different from other As^{+3} peaks which occur at the same energy. All the As^{+3} peaks are within 0.8 eV of each other. It may be significant that the As_2O_3 peak, the AsF_3 peak and the As^{+5} peak in the graphite/AsF_5 sample are not at the same energy. However, since the error in the position of the AsF_3 peak is large one cannot determine whether the difference is between As_2O_3 and AsF_3, or between AsF_3 inside and outside the graphite.

The intensity results in Table IV-I show that a reasonable fraction of As^{+3} exists in all of the graphite/AsF_5 compounds studied. As mentioned before, it is likely for samples A, B, E and G, that their small As^{+3} peaks were caused by the orientation induced on the sample when each sample was pressed. The larger size of the AsF_3 peak in sample D may be caused because the AsF_3 and graphite/AsF_6^- are not the perfect standards for the graphite/AsF_5. Note that if the

oxidation reduction in equation IV.1 proceeded to completion, the relative intensity of the As^{+3} peak would be 0.50. The value of 0.70 (12) for the randomly oriented sample is not too far from this prediction especially since a visual inspection of the spectra indicates that a ratio of 0.50 is more reasonable, assuming the intensity per As atom is the same for AsF_3 and AsF_6^-.

A comparison of these edge results with the EXAFS results is contained in Section D of this chapter.

C. EXAFS Analysis

Analysis of the EXAFS features followed the methodology presented in Chapter III. A qualitative comparison of Fourier Transforms of the spectra showed that only the first shell would produce significant information for the Arsenic fluorocomplexes. Higher shells were too small in amplitude. The following analysis concentrates on the radial distance of this peak.

Figure IV-12 shows a raw spectrum plot of normalized post-edge data, μ_I^*, versus $k(1/\mathring{A})$ for $CsAsF_6$. The first post-edge background removal is also plotted on the same figure. This background strip is the result of a triple smooth (S^3) which covered the same k-range as 1.2 EXAFS cycles. Note that the background does not follow the EXAFS. The resultant file multiplied by k^3 is plotted in Figure IV-13. A second refining background strip is overplotted. This is the same type of strip as before except that the data, $X(k)$, was multiplied by k^3 before the smoothing background was calculated.

Plots Versus Wavevector and Distance

Figure IV-14 shows the resultant EXAFS file $\chi(k)$ multiplied by k^2 for six representative files. All of the files were processed in the manner described above and they all have a similar appearance to the files shown in Figure IV-14. The best files have EXAFS visible well above the noise level out to k = 18 $1/\mathring{A}$. However, since this is not true for the bulk of the data and since many of the files were only obtained to a maximum of k = 15.2 to 16.2 $1/\mathring{A}$, the data analysis presented was done over a k-range of k = 4.0 to 15.0 $1/\mathring{A}$. Analysis results with the higher k-values included and with other k-ranges were not substantially better nor significantly different. Figure IV-15 shows the $\chi(k) * k^3$ Fourier Transform of the six files in Figure IV-14. The k-range used was k = 4.0 to 15.0 with a 4.0 Kaiser apodization window applied in order to reduce sidelobes.

Analysis Methods

Figure IV-15 illustrates that the first shell distances are all very similar. Any analysis of these files for distances must be quite exact if any differences are to be observed. The expected average distances for AsF_5, AsF_3 and AsF_6^- are 1.68 $\mathring{A}$, 1.71 $\mathring{A}$, and 1.73 $\mathring{A}$, respectively. Comparisons of the positions of the Fourier Transform peaks among samples yielded distances which were separated by similar amounts. In addition, the data were fit in k-space using the fitting model developed by Hodgson et al. (8). Similar consistent results were obtained via this method. However, more reliable and accurate results were obtained by the fitting model developed by Bell Laboratories which uses the theoretical EXAFS amplitude and phase shift calculations

of Teo et al. (9). These results are discussed below. One further advantage of this latter method is that absolute distances are calculated instead of relative distances. For these reasons only the data from the latter analysis approach are presented in this work. A comparison of the three methods for these and other data is reported by Kirby et al. (10).

Description of Analysis

The following is a summary of the analysis approach used for each data file. The complete method was described in Chapter III. Starting with $\chi(k) * k^3$ with the background removed, prepared with a given E_o, the theoretical phase was removed and a Fourier Transform computed. E_o was varied until the sine component peak of the transform occurred at the same R-value as the power spectrum peak. This was an estimate of the E_o which was consistent with the theoretical calculation. This E_o value was used as a starting point for the fitting in k-space.

Using the theoretical amplitude and phase functions, the fitting model was equivalent to

$$F(E) = Ae^{\sigma k^2} \sin(2kR)$$

where $k = \left(\frac{2m}{\hbar^2}(E - E_o)\right)^{\frac{1}{2}}$ and A, σ, R and E are variables. For a one shell fit, the data, $\chi(k)$, were Fourier Transformed and filtered so that only the one shell of interest was kept. The initial Fourier Transform was k = 4.0 to 15.0 and the data fitted were k = 5.5 to 13.5 $1/\mathring{A}$.

An example of the fit and data is plotted in Figure IV-16. The phases of the two files are quite similar. However, the amplitude of the two files does not agree as well. This is true for all the spectra studied. The procedure in the next paragraph improved on the distance values. In order to get an estimate of the error in R, E_o and R were varied around the best fit values. The least square error function ($\Sigma(D - F)^2$), between the data (D) and the fit (F), is plotted in Figure IV-17. The contour was drawn for a 100% increase in this error above the minimum. The projection of this error ellipse onto the R and E_o axis is an estimate of the error in R and E_o. Tables IV-III and IV-IV report the results of these fits with the $e^{\sigma k^2}$ on all of the data. The distance, R, with the error estimates, is listed in column 3 of Table IV-III. The values of A, σ, and E_o are listed in columns 3, 4 and 5 of Table IV-IV. Error estimates for E_o are included. These results will be discussed later.

Tables IV-III and IV-IV also have results of fits with the total amplitude removed. The data used in these fits were prepared by Fourier isolating the first shell of the data $\chi(k)$. The total amplitude function and then the theoretical phase function were removed from the data. The fitting function is now:

$$F(E) = A \sin (2kR)$$

where $k = \left(\frac{2m}{\hbar^2} (E - E_o) \right)^{\frac{1}{2}}$.

A plot of these data and fit is shown in Figure IV-18. The agreement is excellent. Figure IV-19 is an error plot similar to

Figure IV-17. The 100% and 1000% increase in error contours are plotted. The 100% error contour provides an estimate of the error in R and E_o. Tables IV-III and IV-IV report the results of these fits on all the data. The distance values with error estimates in parentheses are listed in column 4 of Table IV-III. The E_o values with error estimates in parentheses are listed in column 6 of Table IV-IV. The amplitude, A, is a variable which should be and is close to 1.0. For all the samples except $Xe_2F_3AsF_6$, it was between 0.993 and 0.999. For the $Xe_2F_3AsF_6$, the amplitude was 0.982 which is an indication of the distortion present in the first shell of this sample.

Quantitative Results for Arsenic Fluorocomplexes

As mentioned above, Tables IV-III and IV-IV contain the quantitative results of the single shell fits done on all As-F first shells. Figure IV-20 is a plot of the amplitude removed error contours for a representative selection of the samples analyzed. This figure is a useful visualization of the EXAFS distance results. Tables IV-IIIa and IV-IVa contain standard compound results while Tables IV-IIIb and IV-IVb contain graphite intercalate results. The analysis technique used was described above.

Table IV-IIIa is a comparison of the distance results with the two EXAFS fits reported in columns 3 and 4. Since the distances of column 4 were obtained with the amplitude removed, they were not affected by inaccuracies in the theoretical amplitude function. Furthermore, they were minimally affected by multiple distances

within the same shell, since the amplitude removal eliminated the beating between shells. Column 4 therefore contains the best estimate of the average distance and error. For comparative purposes, the results of the other techniques are also listed. The agreement between the results reported here for AsF_3 and AsF_5 gas and the results reported by F. B. Clippard and L. S. Bartell (11) using electron diffraction is excellent. This agreement is a confirmation of this analysis method of the theoretical phase calculations.

The agreement of the distances of $Xe_2F_3AsF_6$ as measured by EXAFS and X-Ray crystallography (14) are within the statistical errors. The error listed for the EXAFS result is not justified by the noise present in the file. The signal-to-noise of this fit is as good as most of those files which have an estimated error of less than $\pm$ 0.007 Å in the distance estimation. The large error of $\pm$ 0.022 Å in the EXAFS determination of R is due to the distortion of the AsF_6^- octahedra as indicated in the summary of the X-Ray data contained in Table IV-IIIa. Thus an abnormally large error in the EXAFS distance determination indicates that a distorted shell is present.

The agreement between EXAFS and X-Ray data (3) is not as good for $XEFAsF_6$. The difference between the EXAFS distance and the average X-Ray distance is -0.018 $\pm$ 0.015. The error in this number indicates that the difference is barely statistically significant. This difference is troublesome given the excellent agreement of the distances measured in the other compounds.

Note that the EXAFS distance is within 0.002 Å of the average of the five close fluorines in $XeFAsF_6$. This effect has been noted in other compounds in which the first shell distortion is such that a majority of the bonds are at one short distance with a minority of the bonds at a longer distance. For manganese absorbers with oxygen scatterers and a known crystal structure which indicates 4 oxygen atoms at one distance and 2 oxygen atoms 0.20 Å farther away, the EXAFS distance found is within 0.02 Å of the shorter bond distance (10,12). This is also consistent with the recent report by Eisenberger et al. (13) that the EXAFS determination of the average distance for distorted shells is typically shorter than the real average distance. If one generates EXAFS data using the theoretical model and measured crystal structure distances with no thermal motion term, the Fourier Transform shows an effect by the minority longer distance scatterers. As the thermal motion term is increased to a reasonable value, the effect of the longer distances on the Fourier Transform disappears.

The other AsF_6^- compounds present a consistent set of distances as indicated in Tables IV-IIIa. All were expected to have an undistorted AsF_6^- octahedron. The error bars on the distance and the size of the thermal motion term, σ, in Table IV-IVa indicate that this is the case. Note that the distorted $Xe_2F_3AsF_6$ has a large negative value of σ compared with all the other files. The largest differences in the distances are just large enough to be statistically significant. The average of all the distances is 1.727 Å which is representative of the undistorted AsF_6^- octahedra. Given the consistency of these data,

the report (14) of a 1.800 Å bond distance for $KAsF_6$ must be in error.

Graphite/AsF_6^- has a bond distance of 1.714 Å as indicated in Table IV-IIIb. The bond distance is shorter for this compound than for the other AsF_6^- compounds.

The graphite/AsF_5 distances reported in Table IV-IIIb have two basic averages. Sample D at three different temperatures has an average distance of 1.722 Å while samples A, B and E have an average distance of 1.706 Å. This difference corresponds with the difference in the relative intensity of the As^{+3} peak in the same sets of samples. Since the difference in the intensity of the As^{+3} peak could easily depend upon the orientation difference, the orientation may explain the difference in distances as well. Orientation may reduce the effective distance measured. It is possible that the samples were in different stages of intercalation. A completely intercalated sample should have a shorter bond distance. Measurements have been made which indicate that the thickness of the gallery spacing decreases for first stage compounds as the composition C_8AsF_6 or C_8AsF_5 is approached (15).

$C_{16}AsF_5$, sample G, has a distance in between the other graphite compounds. Note that it is also a pressed pellet. Compared with the other pressed graphite/AsF_5 samples, the bond distance is longer. Since it is a stage 2 compound with less AsF_5 intercalated than the other samples, this longer distance may be related to the extent of intercalation.

Graphite/AsF_5+F_2, sample C, has the lowest distance, 1.697 ± 0.009 Å,

of all the graphite compounds, although it is consistent with the graphite/AsF_5 compounds with a bond distance of 1.706 $\pm$ 0.006 Å. It is apparent that this compound is not the same as graphite/AsF_6^-, sample F. Either sample C was not graphite/AsF_6^-, or the stage of intercalation was different which caused the short bond distance.

Figure IV-20 provides a visualization of these results which shows that all the graphite intercalates have distances which are similar to the AsF_6^- and AsF_3 distances. The bond distances are not similar to the AsF_5 gas distances. This shows that the intercalated species is not AsF_5 gas.

Table IV-IV contains the rest of the parameters obtained from the fitting program. Columns 3, 4, and 5 are the parameters A, σ, and E_o of the fit with only the theoretical amplitude removed and a variable $e^{\sigma k^2}$ term.

Column 2 is an estimate of the number of fluorine scatterers in the shell. It is derived from the amplitude term A in column 3 and has been normalized so that AsF_3 gas sample B has a value of N = 3. The derivation equation is $N = 3 * A_i * R_i^2/(A_{AsF_3} * R_{AsF_3})$. According to the theoretical model of Teo et al. (9), A_i should be proportional to N_i/R_i^2. For those samples which were known to be ordered, an orientation corrected value of N is included in Table IV-III.

Column 6 is the E_o found for the fit with the total amplitude removed and no $e^{\sigma k^2}$ term. As mentioned before, the amplitude A for this second fit was 0.982 for $Xe_2F_3AsF_6$, 0.993 for graphite/AsF_5+F_2, sample C, and 0.995 for $XeFAsF_6$. For all other files A ranged between

0.996 and 0.999. This is another indication that the AsF_6^- octahedron is distorted in $Xe_2F_3AsF_6$ and it may be indicative that distortion exists in the EXAFS of $XeFAsF_6$ and graphite/AsF_5+F_2 but this is not a clearcut statement.

The thermal motion parameter σ listed in Table IV-IV is indicative of the distortion of $Xe_2F_3AsF_6$. It is 3 times larger in magnitude than any other value of σ. A distorted shell would have a large thermal motion term using our present one shell model.

Positive values or exceptionally small negative values of σ are non-physical. Those positive values in Table IV-IV arise from two causes. For AsF_3, sample A, the signal to noise in the file is poor especially at high values of k. This distorted the amplitude function which affected σ. The other cause of a non-physical value is the inaccuracy in the shape of the theoretical amplitude function. This is particularly evident at the lower temperatures. This is another cause of non-physical thermal motion terms. Even when the thermal motion term is reasonable and the fluorine shell is undistorted as it is in AsF_3 sample B, the shape of the log of amplitude function versus k with the theoretical amplitude removed is not the straight line we would expect. See Figure IV-21 which is a plot of the log of the residual amplitude function versus k . These errors in the shape of the amplitude function also affect the amplitude, A, which is found. For this fitting equation, J. A. Kirby has shown that σ and A are highly correlated variables (10,12).

The value of N in column 2 of Table IV-IV is calculated from A, as previously described. Note that the number of scatterers for

the first AsF_3 gas sample and AsF_5 gas are close to the correct values of 3 and 5. Some of the AsF_6 compounds are good. Most of the error is due to inhomogeneity in the sample. S. Hunter has shown (16) that a 5% area of pinholes in the sample will reduce the size of the EXAFS modulations by 20% without changing their shape. Those samples which are known to have been inhomogeneous are footnoted. The correction factor of 1.282 for the oriented estimate of N was derived assuming that the intercalant species acts as the oxidant species indicated in Figure IV-22c. The agreement between this N and the expected number of scatterers is excellent. The correction factor for two other possible AsF_5 intercalant species indicated in Figures IV-22a and IV-22b would be 1.000 and 0.833. This correction factor would not provide agreement with the expected number of scatterers. Therefore, the existence of these species is not supported by these data.

Finally, consider the values of E_o in Table IV-IV. The E_o values are remarkably similar. The E_o values range from 11886 eV to 11891 eV with the exception of both fits on AsF_3 sample A (E_o = 11881, 11882), the first fit on $Xe_2F_3AsF_6$ (E_o = 11893 eV) and the second fit on $XeFAsF_6$ (E_o = 11893 eV). The errors in E_o are largest for these files. Therefore they may not be significantly different from other compounds of the same type.

A trend can be observed in the variation of the E_o values even though this trend is not statistically significant. The E_o values are correlated with oxidation state:

$E_o(AsF_3) \lesssim E_o(C/AsF_5) \approx E_o(C/AsF_6^-) \approx E_o(AsF_5) \lesssim E_o(AsF_6$ Compounds)

Note that this is a tenuous trend since a calculation of the difference between the E_o of AsF_3 and that of the other AsF_6^- compounds yields 4.7 $\pm$ 5.2 eV which is not statistically significant.

The coarse adjustment for E_o is a true measure of the onset of the continuum. Part of the fine adjustment of E_o may be for differences in oxidation state. However, most of the fine adjustment is an adjustment of the constant phase term in the sine wave so that the theory and experimental data are in phase. For all absorbers, and all scatterers in the first 4 rows of the periodic table, the phase shift is approximately linear. Therefore, the non-linear part of the phase affects E_o determination only slightly. In addition, distortions of the sine wave due to the amplitude function for backscattering are small for scatterers in the first four rows.

As_2O_3 Analysis

An EXAFS analysis of As_2O_3 is included as a contrast to the arsenic fluorine compounds. It also provides proof that there is no significant contamination of our samples with As_2O_3 which would be present if the samples had decomposed.

Figure IV-23 is a plot of the EXAFS data. Note that it is significantly different from the fluorine compounds. Two distinct frequencies are evident in Figure IV-23 and in its Fourier Transform plotted in Figure IV-24. The first peak is an oxygen peak while the second peak is a mixture of oxygen and arsenic.

The results of the fits are reported in Table IV-VI. The two peaks were Fourier isolated and then fit separately. Two shells

were fit simultaneously to the second peak. There is excellent agreement between the X-Ray crystallographic results (17) and EXAFS results listed in Table IV-VI. The data and fit performed on the first and second peaks of As_2O_3 are shown in Figures IV-25 and IV-26, respectively.

D. Conclusions

Table IV-VI is a condensation of the results presented in the previous two sections. The error listed inside each set of parentheses also includes an estimate of the breadth of the distribution of values which were averaged for the AsF_6^- compounds and the two sets of C/AsF_5 compounds. For these compounds, the error is not a measure of the accuracy of any of the values of an individual file. For instance, the distance for the AsF_6^- compounds on Table IV-VI is 1.727 $\pm$ 0.10 A. This is representative of the distance we would expect for the AsF distance in an undistorted AsF_6^- octahedron. From Table IV-IIIa, the bond distance measured for As-F in $C_{10}F_8AsF_6$ is 1.733 $\pm$ 0.003 A.

General Conclusions About Arsenic Fluorocomplexes

In the edge spectra of the compounds, the position of the white peak (primarily a 1s to 4p transition) depends upon coordination charge in an understandable fashion. A prediction of the coordination charge, C, for the species present in these compounds would be:

$$C\left[As^{+3} \text{ in } As_2O_3\right] \lesssim C\left[As^{+3} \text{ in } AsF_3\right] \approx C\left[As^{+3} \text{ in } C/AsF_5\right] <$$
$$C\left[As^{+5} \text{ in } C/AsF_5\right] \approx C\left[As^{+5} \text{ in all } AsF_6^- \text{ compounds}\right] \lesssim C\left[As^{+5} \text{ in } AsF_5\right].$$

The position of both the pre-continuum absorption peaks and the position of the onset of the continuum should follow this trend. The continuum onset is difficult to estimate. We have done this. The energy of the white peak, which is largely an As (1s) to As (4p) transition, follows the following trend (See Table IV-VI):

$$E[As^{+3} \text{ in } As_2O_3] \lesssim E[As^{+3} \text{ in } AsF_3] \lesssim E[As^{+3} \text{ in } C/AsF_5] < E[As^{+5} \text{ in } AsF_5] < E[As^{+5} \text{ in } C/AsF_5] \approx E[As^{+5} \text{ in all } AsF_6^- \text{ compounds}].$$

This progression agrees with the order of the coordination charge with the notable exception of AsF_5 gas. Since AsF_5 gas is a trigonal bi-pyramid we would need a mixing of the 4s and 4p orbitals of As in order to create the molecular orbitals of AsF_5. Thus the first empty orbital of p-symmetry would be a mixture of As - 4s and 4p and F orbitals. It would therefore have a lower energy than would be predicted from coordination alone for the AsF_5, As - 4p state.

Note that the As^{+3} peak in C/AsF_5 is slightly above the As^{+3} peak in AsF_3. This may indicate a partial positive charge on the AsF_3 species, but no definitive statement can be made due to the large error in the determination of AsF_3. I believe that this difference is real since the monochromator was slipping badly on the day sample B was run giving 68.4 eV for the position of the AsF_3 peak. Its energy calibration is therefore questionable. The energy reference for sample A is much better and a value of 67.7 $\pm$ 0.41 eV was obtained. The As_2O_3 energy reference for that day was 67.4 $\pm$ 0.4 eV.

As discussed in Section C, the distances on all the compounds are in excellent agreement with reported results of X-Ray crystallography and electron diffraction. This is indicated on Tables IV-IIIa and IV-V.

The agreement is so good that results for the standard AsF_6^- compounds reported in Table IV-IIIa must also be accurate. The presently accepted value for the first shell fluorine distance in $XAsF_6$ is 1.80 ± 0.05 Å (14). Since the error estimate is large and since only an X-Ray powder pattern was used to determine this distance, the numbers presented in this work are much better estimates of the bond lengths of an undistorted AsF_6^- octahedron than the powder pattern distance presented above. The complete results for each of the five samples, $CsAsF_6$, $NaAsF_6$, O_2AsF_6, $C_6F_6AsF_6$ and $C_{10}F_8AsF_6$, are reported in Table IV-IIIa. The distances are similar enough that the average distance of 1.727 ± 0.010 Å listed in Table IV-VI is representative of all t compounds.

Specific Conclusions About the Graphite Compounds

The estimated number of scatterers, N, which can be calculated from the amplitude of the fit is summarized in Table IV-VI. As already indicated, N is useful only if the samples were homogeneous. The values of N for homogeneous samples are summarized in Table IV-VI. For the oriented samples (footnote a in Table IV-VI), the value of N was increased by a factor of 1.282 to account for orientation. This factor was derived by assuming that Figure IV-22c represented

the intercalant species. Since the corrections for Figure IV-22a-b would be 1.000 and 0.833, Figure IV-22c agrees with the measured value of N while Figures IV-22a-b do not. The predicted gallery heights for Figures IV-22a and b do not agree with the measured gallery heights presented in Table IV-VII while Figure IV-22c agrees. Therefore the oxidation, represented in Figure IV-22c, is consistent with these data.

The structure shown in the region of the white peaks in Figures IV-7, 8, 9, and 10 is proof that As^{+3} and As^{+5} coexist in graphite/AsF_5. A summary of the positions of these peaks is listed in Table IV-VI.

The intensities of the As^{+3} peak 2 with respect to As^{+5} peak 1 are not entirely conclusive evidence about the relative amount of As^{+3} in graphite/AsF_5. The average values of these proportions for the pressed and random graphite/AsF_5 compounds are listed in Table IV-VI. Several problems with the size of these fitted intensities have already been discussed. To repeat:

- The orientation of the sample caused by pressing the samples must have caused a decrease in the intensity of the As^{+3} peak with respect to the As^{+5} peak.

- Although the peak is similar to AsF_3, the position, intensity per As^{+3} atom or width of this peak of the intercalated AsF_3 molecule may be different. This could not be studied in detail because the As^{+5} peak was too close.

- Different resolutions due to monochromator and temperature gave different answers. This was particularly evident when samples were cooled to lower temperatures.

As mentioned before, the AsF_3 gas peak may be slightly different in energy than the graphite/AsF_5 peak 2. If the shift in the position of peak 2 is correct, then the fractional charge transferred would be about 0.15 $\pm$ 0.07 electrons of positive charge to the AsF_3. This might be the explanation of why the AsF_3 does not escape from the graphite as one would expect.

This possible partial charge transfer to AsF_3 would modify our prediction of the following reaction slightly:

$$\text{(Graphite) plus } {}^{\prime}(AsF_5) \rightleftarrows \text{(Graphite)}^{++}(AsF_6^{-})_2AsF_3 \qquad \text{(IV.2)}$$

Furthermore, although the reaction in equation IV.2 must occur in order to explain the XAES data presented in this work, the reaction may not continue to completion. Some type of AsF_5 species may be present in graphite/AsF_5. This is most likely in the fully intercalated C_8AsF_5 which must be kept under an AsF_5 atmosphere in order to maintain the stoichiometry, C_8AsF_5. Reflectivity measurements (18) indicated that the extent of oxidation of the graphite was much lower than the value of 2/3 predicted by equation IV.2. We have serious doubts about the validity of using data from a surface effect to predict bulk properties of an anisotropic sample which may have two or more types of intercalant molecules. In addition, the effective mass of the charge carrier had to be estimated in order to calculate the amount of charge transfer from reflectivity data. The calculated charge transfer may be greatly in error. Therefore, we believe that equation IV.2 describes the intercalation process.

The change in the size of the AsF_3 peak in the pressed versus the random samples tells us about the orientation of the empty As-4p molecular orbital. It will be aligned along the c-axis of the graphite if the disappearance of this state is due to the ordering of the sample in the pressed graphite samples.

Arguments have been presented (19) that the As^{+3} states we see in the edge structure are caused by AsF_3 on the surface. The shaved powdered graphite samples used for this experiment simply do not have enough surface to volume ratio to account for an As^{+3} peak which is between 10% and 40% of the total As in the sample.

It has been suggested (20) that the As^{+3} peak is really As_2O_3 in our samples. Several features of the data files obtained eliminate this possibility:

- The As_2O_3 white peak is 0.9 eV $\pm$ 0.4 eV below peak 2 in graphite/AsF_5.
- The As_2O_3 white peak is shorter and broader than the white peak in AsF_3 and peak 2 in graphite/AsF_5.
- Between the white peak and the onset of the continuum, additional transitions which are not noted in AsF_3 or graphite/AsF_5 are observed.
- The first shell bond distance for all graphite compounds is less than 1.73 Å with no indication of the 1.80 Å Oxygen bond of As_2O_3.
- There is no evidence in any Arsenic fluorocomplex spectra for an As-As distance of 3.23 Å. Note that for the As_2O_3 data in Figure IV-16, this second peak is twice the size of the As-O first peak in the $\phi_3(k)$ spectrum.

A range of distances which vary from 1.70 Å to 1.72 Å is presented in Table IV-VI for the graphite intercalates. Figure IV-20 clearly indicates that all the graphite compounds have first shell

distances which are similar to the AsF_3 and AsF_6^- distances and significantly different than the average first shell distance of AsF_5. These distances are definitely longer than the average distance of AsF_5 gas (1.68 Å) and are similar to the distances of AsF_3 gas (1.71 Å) and the AsF_6^- compounds (1.73 Å). Using a distance of 1.708 Å for AsF_3 and 1.727 Å for AsF_6^- and assuming a composition $AsF_3(AsF_6^-)_2$, an average distance of 1.723 Å is calculated. This is nearly identical to the distance of 1.722 $\pm$ 0.009 Å found in the randomly oriented graphite/AsF_5 sample. This supports the proposition that $AsF_3(AsF_6^-)_2$ is the intercalant species in this sample.

The short distance of 1.706 Å measured in the pressed graphite/AsF_5 samples may occur because the samples are oriented. If this is true, an orientation dependence of the distance measurement is indicated. In this regard, note that the bond distance in the pressed graphite/AsF_6^- is only 0.016 Å less than the distance in the random graphite/AsF_5 sample. Note further that this difference of 0.016 $\pm$ 0.011 Å is just barely statistically significant. The randomly oriented graphite/$AsF+F_2$ sample is not exactly the same as the pressed graphite/AsF_6^- as anticipated. The bond distance difference of 0.017 Å $\pm$ 0.010 Å cannot be explained by the orientation difference. Additionally one notes that the pressed $C_{16}AsF_5$ has a distance of 1.714 Å. Possible explanations are discussed below.

Recent reports on X-Ray diffraction results have shown that the

separation graphite planes around a filled gallery can change as a function of concentration as much as 0.18 Å as the stoichiometry is changed in graphite/AsF_6(15). The results are shown in Table IV-VII. This can explain the variation in As-F distances which we have observed. As the layer spacing decreases, the bond distance for As-F would probably decrease. Table IV-VIII shows the intercalate distances with the results of the gravimetric analysis listed. If a careful study of the XAS features correlated closely with accurate gravimetry and X-Ray crystallographic measurement of stage and c-axis distance were made, this variation in As-F bond distances could be explained. The data presented here are only suggestive that the bonds may shorten as the composition of AsF_5 or AsF_6^- intercalates varies. It is possible in graphite/AsF_5 that the bond distance in the a-b plane is shorter than the average bond distance. Therefore a complete study of XAS features with both oriented and random samples in conjunction with X-Ray crystallography measurements of c and stage, accurate gravimetry, and conductivity measurements must be done on the same samples. Such an experiment would resolve this issue.

In conclusion, any supposition about the nature of the intercalants in graphite/AsF_5 must be consistent with these results:

- AsF_3 and AsF_6^- are both present in the filled galleries of graphite/AsF_5 . Both the edge and EXAFS features support this conclusion.

- The As-F bond distances are between the AsF_3 and AsF_6^- bond distances. The variation in distance may be a function of orientation, or composition of the graphite compound. The oxidation of graphite indicated in equation IV.2 is consistent with these results.

Table IV-Ia†

PEAK POSITIONS OF
STANDARD COMPOUNDS

Sample		T(°C) §	Position Peak 1 (eV) E-11800 eV	Position Peak 2 (eV) E-11800 eV
As_2O_3	A			67.90
	B			67.54
	C			68.16
	D			67.64
	E			67.44
	F			68.09
AsF_3	A			67.67
	B			68.45
AsF_5	A		74.25	
	B		74.15	
$XeFAsF_6$			75.38	
$Xe_2F_3AsF_6$			75.12	
O_2AsF_6	A		75.82	
	B		75.43	
$CsAsF_6$			75.26	
$C_{10}F_8AsF_6$			74.70	
$C_6F_6AsF_6$		-93	75.21	
$NaAsF_6$			75.24	

Table IV-Ib†

PEAK POSITIONS AND RELATIVE INTENSITIES OF GRAPHITE INTERCALATES

Sample		T (°C)§	Position Peak 1 (eV) E-11800 eV	Position Peak 2 (eV) E-11800 eV	Relative Intensity of Peak 2 2nd derivative	Relative Intensity of Peak 2 Edge fit*
C/AsF_5	A		75.55	68.96	0.25	.18 (4)
		-93	75.41	68.89	0.39	.22 (4)
	B		75.33	68.67	0.35	.27 (4)
	D		75.05	68.24	0.85	.75 (8)
		-50	75.46	68.64	0.81	.67 (8)
		-100	75.23	68.43	0.79	.67 (8)
	E		75.19	68.80	0.21	.25 (4)
			75.28	68.81	0.23	.25 (4)
		-140	74.75	68.44	0.27	.30 (4)
C/AsF_6	F		75.48			
		-140	74.85			
	H		75.37			
C/AsF_5+F_2	C		75.55	‡	‡	‡

† No absorption peak was observed if the peak position or intensity is not listed.

‡ Due to poor monochromator resolution, the possible existence of a peak 2 could not be confirmed or disproved.

§ Unless noted otherwise, the samples were run at room temperature (22° C).

* Estimate of error in last place is in parentheses.

Table IV-II

SUMMARY OF PEAK POSITIONS
AND INTENSITIES

Samples	Peak Positions: Peak 1 (As^{+5}) (eV) E - 11800 eV*	Peak Positions: Peak 2 (As^{+3}) (eV) E - 11800 eV*	Relative Intensity of Peak 2*
As_2O_3		67.8 (3)	
AsF_3		68.1 (6)	
AsF_5	74.2 (3)		
AsF_6^--Compounds	75.3 (4)		
Graphite/AsF_6^- Pressed	75.4 (3)		
Graphite/AsF_5 Random	75.2 (3)	68.4 (3)	.70 (12)
Pressed	75.3 (3)	68.7 (3)	.25 (8)

*Estimate of error in last place is in parentheses.

Table IV-IIIa

RADIAL DISTANCES OF STANDARD COMPOUNDS

Sample		T(°C)†	Fit with $e^{\sigma k^2}$ R (Å)*	Fit with Amplitude Removed R(Å)*	Results of Other Techniques§ Average R(Å)*	N	R(Å)*
AsF_3	A		1.699 (18)	1.701 (12)	1.706 (2)	3	1.706 (2)
	B		1.709 (13)	1.710 (7)			
AsF_5			1.678 (15)	1.681 (4)	1.678 (2)	3	1.656 (4)
						2	1.711 (5)
$XeFAsF_6$			1.727 (15)	1.732 (11)	1.750 (10)	5	1.730(10)
						1	1.860(10)
$Xe_2F_3AsF_6$			1.739 (30)	1.728 (22)	1.740 (20)	2	1.670(30)
						2	1.725(30)
						6	1.755(30)
						2	1.790(30)
O_2AsF_6			1.723 (12)	1.724 (4)			
$CsAsF_6$			1.726 (14)	1.726 (4)			
$C_{10}F_8AsF_6$			1.732 (11)	1.733 (3)			
$C_6F_6AsF_6$		-93	1.730 (12)	1.731 (5)			
$NaAsF_6$			1.727 (13)	1.726 (6)			
$KAsF_6$					1.800 (50)	6	1.800(50)

Table IV-IIIb

RADIAL DISTANCES OF GRAPHITE INTERCALATES

Sample	T(°C)†	Fit with $e^{\sigma k^2}$ R(Å)*	Fit with Amplitude Removed R(Å)*
A C/AsF_5		1.703 (12)	1.705 (4)
	-93	1.698 (13)	1.700 (5)
B		1.704 (11)	1.706 (3)
D C/AsF_5		1.725 (12)	1.725 (5)
	-50	1.719 (12)	1.719 (7)
	-100	1.720 (12)	1.723 (7)
E		1.706 (12)	1.708 (5)
		1.706 (12)	1.708 (5)
	-140	1.705 (12)	1.707 (4)
F C/AsF_6		1.714 (12)	1.715 (6)
	-140	1.712 (12)	1.714 (5)
C C/AsF_5+F_2		1.696 (14)	1.698 (8)
G $C_{16}AsF_5$		1.711 (13)	1.712 (6)

† Unless otherwise noted, the samples were run at room temperature (22° C).

* The estimate of the error in the last place is enclosed in parentheses.

§ The other techniques are: electron diffraction (11) for AsF_3 and AsF_5; X-Ray crystallography for $XeFAsF_6$ (3) and $Xe_2F_3AsF_6$ (4); X-Ray powder pattern for $KAsF_6$ (14).

Table IV-IVa

FITTING PARAMETERS OF STANDARD COMPOUNDS

Sample[§]		N[†]	Fit with $e^{\sigma k^2}$ term A	$(\mathring{A}^2)$	E_o(eV) -11800eV*	Fit With Amplitude Removed E_o(eV) -11800eV*
AsF_3	A	2.9	.5096	.00011	81 (8)	82 (5)
	B	3[†]	.5173	-.00067	86 (6)	87 (3)
AsF_5		4.7	.8444	-.00034	88 (7)	89 (2)
$XeFAsF_6$		4.9[c]	.8274	-.00156	91 (6)	93 (4)
$Xe_2F_3AsF_6$		6.2	1.0352	-.00524	93 (10)	90 (8)
O_2AsF_6		4.6[a]	.7837	-.00070	89 (5)	90 (2)
$CsAsF_6$		5.8	.9850	-.00144	89 (6)	90 (2)
$C_{10}F_8AsF_6$		5.8	.9698	-.00161	90 (5)	91 (1)
$C_6F_6AsF_6$	d/	4.9[a]	.8243	-.00064	90 (5)	90 (2)
$NaAsF_6$		4.6[b]	.7539	-.00118	88 (5)	89 (3)

Table IV-IVb

FITTING PARAMETERS OF GRAPHITE INTERCALATES

Sample§		N†	Fit with $e^{\sigma k^2}$ term: A	σ ($Å^2$)	E_o (eV) -11800eV*	Fit With Amplitude Removed E_o (eV) -11800 eV*
C/AsF_5	A	4.4/5.5	.7685	-.00137	86 (5)	87 (2)
e/		4.4/5.6	.7618	-.00082	85 (5)	86 (2)
	B	4.1/5.1	.7018	-.00047	88 (5)	90 (2)
	D	3.7[a]	.6278	-.00131	90 (5)	90 (2)
f/		4.1[a]	.6955	-.00106	86 (5)	87 (3)
g/		3.5[a]	.5939	.00022	87 (5)	88 (3)
	E	3.8/4.9	.6598	-.00009	88 (5)	89 (2)
		3.7/4.8	.6463	-.00007	88 (5)	89 (2)
h/		3.6/4.6	.6297	.00071	88 (6)	89 (2)
C/AsF_6	F	4.5/5.8	.7781	-.00075	88 (5)	89 (2)
i/		4.4/5.6	.7479	-.00005	87 (5)	88 (2)
C/AsF_5+F_2	C	4.2[a]	.6920	.00024	86 (8)	87 (4)
$C_{16}AsF_5$	G	4.4/5.5	.7562	-.00080	86 (6)	87 (2)

Footnotes for Table IV-IVa,b

§ Unless otherwise noted, the samples were run at room temperature (22°C).

* The estimate of the error in the last placed is enclosed in parentheses.

† A should be proportional to N/R^2 (9). N is normalized with AsF_3, sample B, as a reference, so that this sample is defined to be 3. A second value, corrected for the orientation of the samples, is listed for those graphite intercalates which were oriented samples.

a This sample was inhomogeneous.

b The small amount of white $NaAsF_6$ may not have been adequately mixed with the ground teflon before pressing the sample. The sample was probably inhomogeneous.

c This low value of N may be an indication that the EXAFS is sensitive to the 5 short Fluorine bonds, but it is possible, but unlikely, that the sample was inhomogeneous.

d Sample run at -93° C.

e Sample run at -93° C.

f Sample run at -50° C.

g Sample run at -100° C.

h Sample run at -140° C.

i Sample run at -140° C.

Table IV-V

FITTING RESULTS FOR As_2O_3

EXAFS Results

	Peak 1 Fit	Peak 2 Fit
k-range used ($1/\mathring{A}$)	5.5 to 13.5	5.5 to 13.5
k weighting	k^3	k^0
Starting E_o (eV)	11886	11923

	Shell 1	Shell 2	Shell 3
Atom Type	O	O	As
E_{oi} (eV)*	11888 (5)	11937	11872
σ_i ($\mathring{A}^2$)	-.0024	.0200	.0053
A_i †	.3918	.0432	.0932
R_i ($\mathring{A}$)*	1.797 (15)	3.02 (4)	3.22 (2)

Crystal Structure Results §

	Radial Distances			
	1	2	3	4
Atom Type	O	O	O	O
N_i	3	3	3	3
R_i ($\mathring{A}$)*	1.80 (5)	3.02 (7)	3.23 (1)	3.46 (6)

* The error in the last place is enclosed in parentheses.

† Peak 1 A_i results cannot be compared with Peak 2 results due to different k-weight and fit regions.

§ See Reference 17.

Table IV-VI

SUMMARY OF XAS RESULTS

Samples	Peak Positions* Peak 1 (As^{+5}) E - 11800 eV	Peak 2 (As^{+3}) E - 11800 eV	Relative Intensity of Peak 2*	First Shell Distance R(Å)*	No. of Scatterers N†
As_2O		67.8 (3)		1.800 (15)	a/
AsF_3		68.1 (6)		1.708 (7)	3†
AsF_5	74.2 (3)			1.681 (4)	4.7
AsF_6^- Compounds	75.3 (4)			1.727 (10)	5.8[b]
C/AsF_6^- Pressed	75.4 (3)			1.714 (5)	5.7[c]
C/AsF_5 Random	75.2 (3)	68.4 (3)	.70 (12)	1.722 (9)	d/
C/AsF_5 Pressed	75.3 (3)	68.8 (3)	.25 (8)	1.706 (6)	5.1[a]
C/AsF_5+F_2 Random	75.6 (3)	÷/	÷/	1.698 (8)	d/
$C_{16}AsF_5$ Pressed	§/	÷§/	÷/	1.712 (6)	5.5[c]
$XeFAsF_6$	75.4 (3)			1.732 (11)	4.9[e]
$Xe_2F_3AsF_6$	75.1 (3)			1.728 (22)	6.2

§ Reliable data are not available because of a poor energy calibration for this sample.

÷ The existence or non-existence of peak 2 could not be confirmed because of poor monochromator resolution.

† All values of N are normalized with respect to AsF_3 which was defined to have N = 3.

a The value of N for As_2O_3 is not listed since only one As-O sample was run.

* The estimate of the error in the last place is enclosed in parentheses.

Table IV-VI footnotes, continued

b Only the two homogeneous samples are included in this average.

c As discussed in Section C, these data are corrected for orientation.

d No value of N is listed since all of these samples were inhomogeneous.

e See the discussion in Section C for an explanation of this small value of N.

Table IV-VII*

X-RAY DIFFRACTION DATA FOR SOME
HOPG INTERCALATION COMPOUNDS

Sample	00ℓ Features	c(Å) † (±0.02 Å)	Gallery Height (Å)
$C_{8.1}AsF_6$	1st stage	[illegible]36	7.86
$C_{9.7}AsF_6$	1st stage	8.00	8.00
$C_{13.1}AsF_6$	1st stage	8.04	8.04
$C_{16.0}AsF_6$	2nd stage	11.19	7.85
$C_{8.4}AsF_6$	1st stage	8.02	8.02
$C_{8.4}AsF_5$	1st stage	8.00	8.00
$C_{13.1}AsF_5$	2nd stage	11.34	8.00
$C_{16.5}AsF_5$	2nd stage	11.35	8.01

* For further discussion of these data, see Reference 15.

† The true unit cell c may, in some cases, be an integral multiple of this value, which was derived from the simplest indexing of 00ℓ data.

Table IV-VIII

GRAVIMETRY AND DISTANCE RESULTS

Sample		Orientation	Distance * R(Å)
Graphite/AsF_5			
A	$C_{9.5}AsF_5$	Pressed	1.703 (4)
B	$C_{9.5}AsF_5$	Pressed	1.706 (3)
D	$C_{10.8}AsF_5$	Random	1.722 (9)
E	$C_{7.8}AsF_5$	Pressed	1.708 (4)
G	$C_{16.2}AsF_5$	Pressed	1.714 (6)
Graphite/AsF_5+F_2			
C	$C_{11}AsF_6$	Random	1.697 (9)
Graphite/AsF_6			
F	$C_{12}AsF_6$	Pressed	1.714 (5)

* The estimate of the error in the last place is enclosed in parentheses.

Figure Captions
Chapter IV

IV-1 Sample cell used for solid samples.

IV-2 Sample cell used for gas samples.

IV-3 Absorbance of a representative AsF_6^- salt. The extrapolated file used for a pre-edge strip is overplotted.

IV-4 Normalized K-shell absorbance of $CsAsF_6$. (a) is a scaled plot; (b) is expanded to an arbitrary scale. The smooth lines in (a) and (b) are plots of the extrapolated post-edge function used for edge height normalization. The edge jump is set equal to 1.0 using this function.

IV-5 Normalized K-shell absorbance for six representative As files.

IV-6 An expanded plot of the normalized K-shell absorbance for six representative As files. The files are plotted so that each letter a → f indicates the placement of the edge height value of 1.0 for its respective file, a → f (As_2O_3 → AsF_5). All files are plotted to the same scale.

IV-7 Normalized K-shell absorbance for six representative As files.

IV-8 Normalized K-shell absorbance for four graphite/AsF_5 files.

IV-9 Normalized K-shell absorbance for five AsF_6^- compounds.

IV-10 Second derivative of the normalized K-shell absorbance for seven representative files.

IV-11 Data (solid line) and synthesized files (dots) plots of normalized absorbance. The fitted function was synthesized from AsF_3 and graphite/AsF_6^- standard files

IV-12 Normalized K-shell absorbance and first post-edge background strip overplotted for $CsAsF_6$.

IV-13 $k^3\chi(k)$ EXAFS data and second post-edge background strip overplotted for $CsAsF_6$.

IV-14 $k^2\chi(k)$ plot of EXAFS for 6 representative As-F samples.

IV-15 $|\phi_3(R)|$ plot of 6 representative As-F samples.

IV-16 $k^3\chi(k)$ plot of EXAFS data (dots) and the fit (solid line) with the Debeye Waller term, σ, included.

IV-17 Error contour plot for the fit in Figure IV-16. The contour for a 100% increase in error is drawn.

IV-18 $\chi_T(k)$ plot of $CsAsF_6$ EXAFS data (dots) and the fit (solid line). $\chi_T(k)$ is the EXAFS data with both the complete amplitude and theoretical phase function removed.

IV-19 Error contour plot for the fit in Figure IV-18. The contours for 100% and 1000% increase in error are drawn.

IV-20 100% increase amplitude removed error contour plots for ten representative As-F compounds. The center of the contours is the best fit value and the contour provides an estimate of the reliability of the data.

IV-21 A plot of Log_e (Residual Amplitude) versus k^2 for $CsAsF_6$. The residual amplitude is the amplitude with the theoretical amplitude (a) removed.

IV-22 Presentation of potential intercalant species for graphite/ AsF_5. Potential orientations are indicated. The AsF_3 in (c) may be oriented with the three fluorine atoms pointing up or down. Of these three potential structures only (c) is consistent with gallery height measurements (15) and the XAES and EXAFS data presented in this work.

IV-23 $k^2\chi(k)$ plot of EXAFS data for As_2O_3.

IV-24 $|\phi_3(R)|$ and $|\phi_1(R)|$ radial distribution function plots of EXAFS data for As_2O_3.

IV-25 $k^3\chi(k)$ plot of the first peak of As_2O_3 data (dots) and the fit (solid line) with the Debeye Waller term, σ, included.

IV-26 k^0 (k) plot of the second peak of As_2O_3 data (dots) and the fit (solid line) with the Debeye Waller term, , included. The fit was done using two scattering shells, As an O.

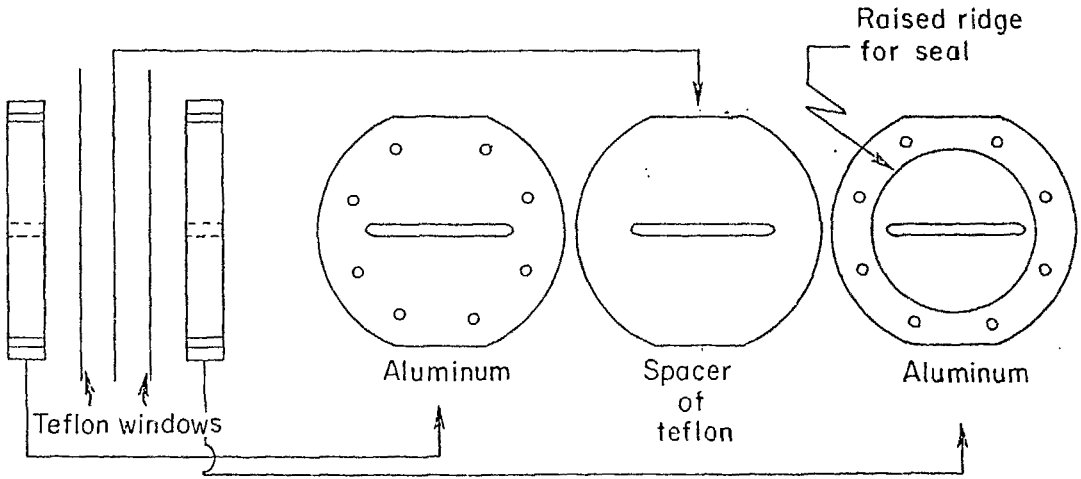

Figure IV-1

XBL798-4983

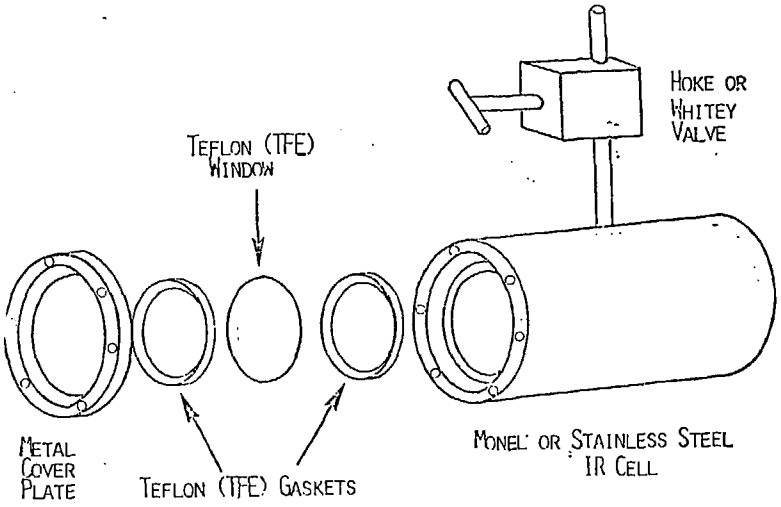

XBL798-4984

Figure IV-2

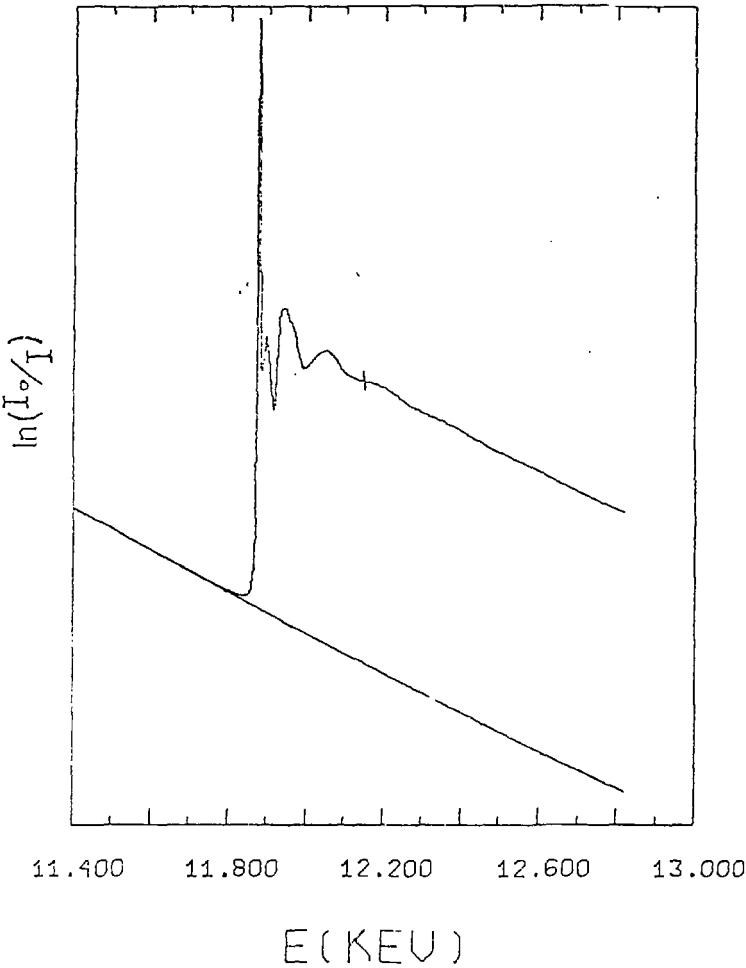

Figure IV-3

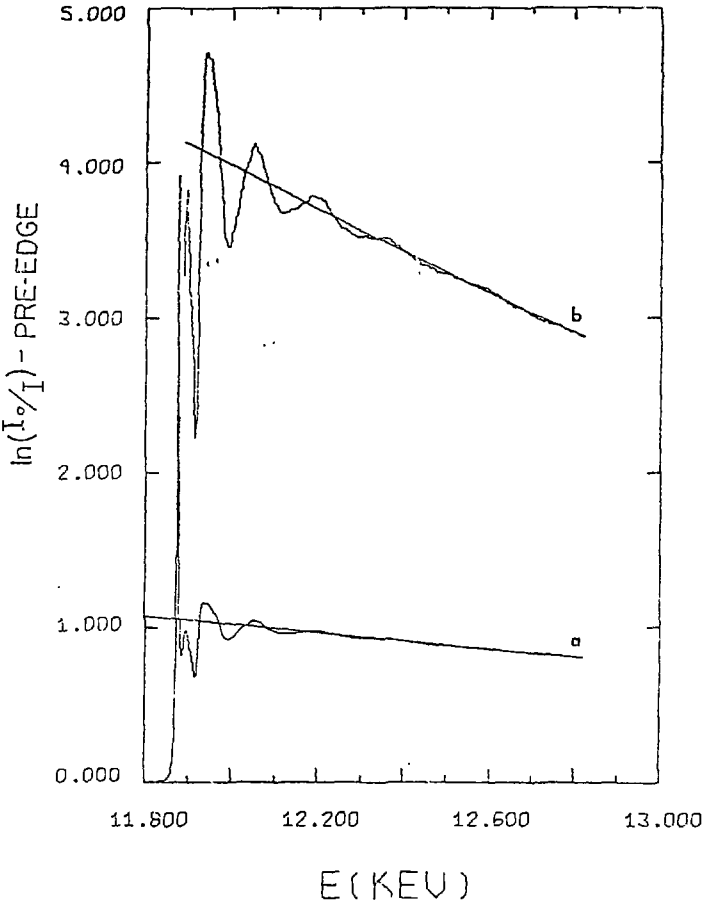
5.000
4.000
3.000
2.000
1.000
0.000
ln(I°/I) - PRE-EDGE
b
a
11.800
12.200
12.600
13.000
E(KEV)

Figure IV-4

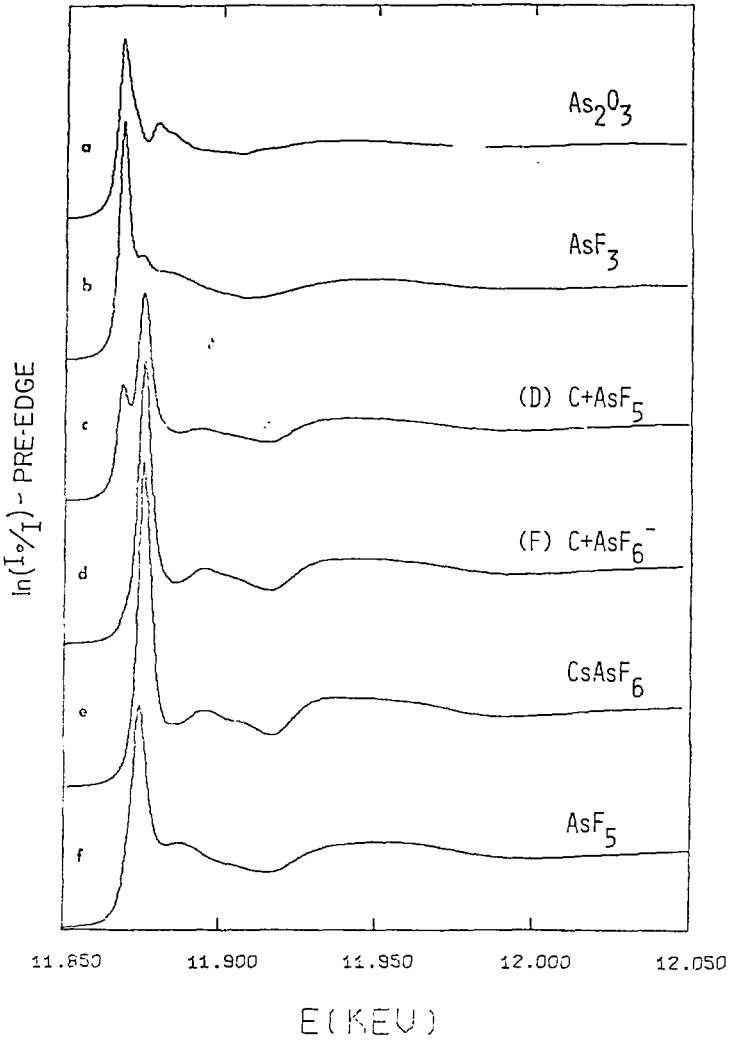
As_2O_3
AsF_3
(D) $C+AsF_5$
(F) $C+AsF_6^-$
$CsAsF_6$
AsF_5
a
b
c
d
e
f
$\ln(I_0/I)$ - PRE-EDGE
11.850
11.900
11.950
12.000
12.050
E(KEV)

Figure IV-5

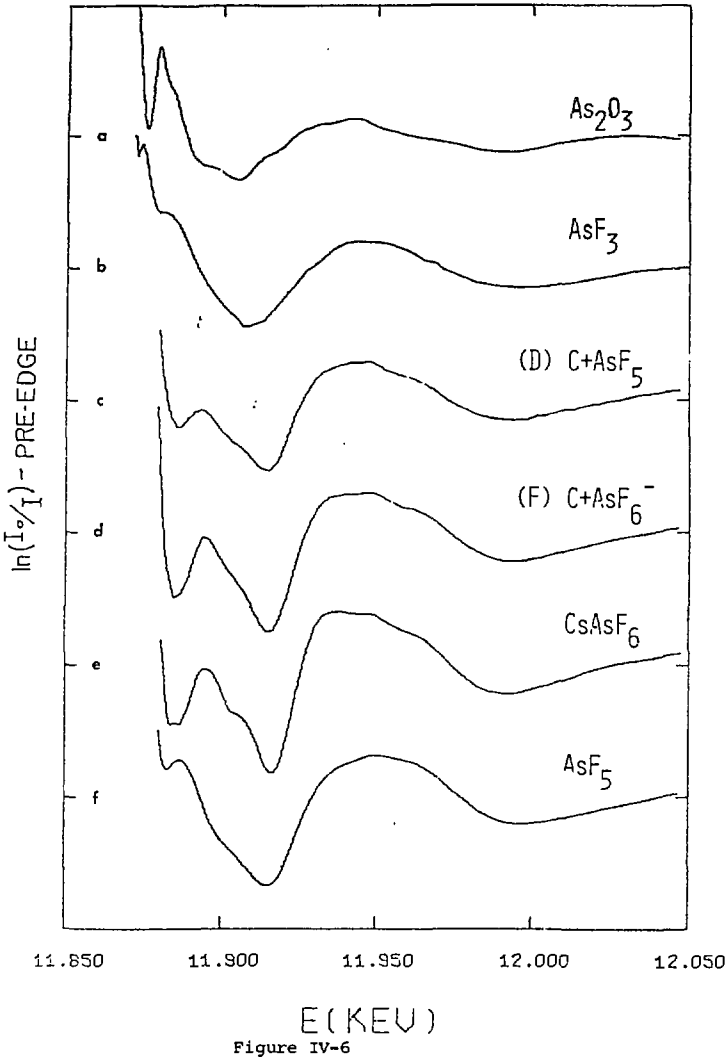
a
b
c
d
e
f
As_2O_3
AsF_3
(D) $C+AsF_5$
(F) $C+AsF_6^-$
$CsAsF_6$
AsF_5
$\ln(I_0/I)$ - PRE-EDGE
11.850
11.900
11.950
12.000
12.050
E(KEV)

Figure IV-6

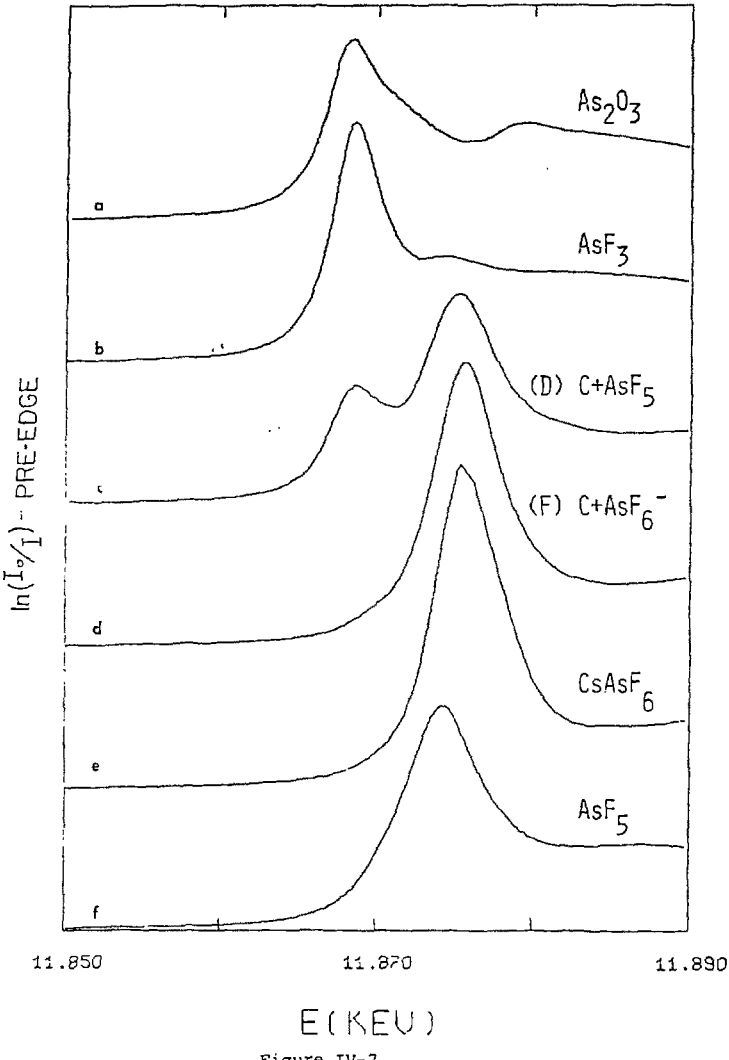
As_2O_3
a
AsF_3
b
(D) $C+AsF_5$
c
(F) $C+AsF_6^-$
d
$CsAsF_6$
e
AsF_5
f
$\ln(I_0/I)$ - PRE-EDGE
11.850
11.870
11.890
E(KEV)

Figure IV-7

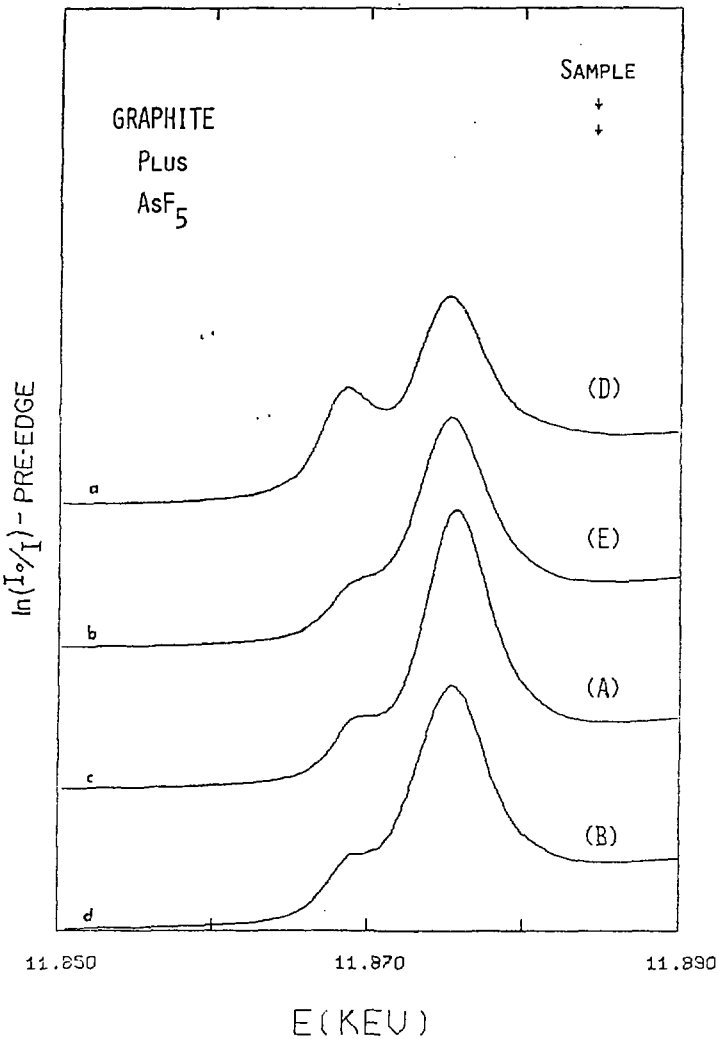
SAMPLE
GRAPHITE
PLUS
AsF5
(D)
(E)
(A)
(B)
a
b
c
d
ln(I°/I) - PRE-EDGE
11.850
11.870
11.890
E(KEV)

Figure IV-8

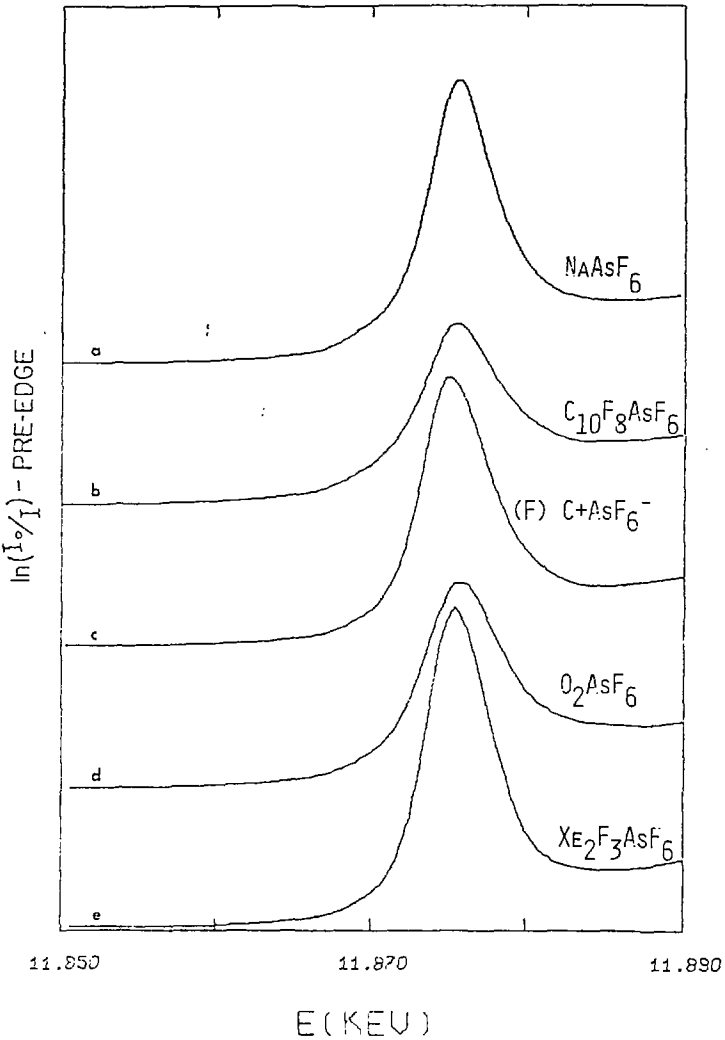
NaAsF6
C10F8AsF6
(F) C+AsF6-
O2AsF6
Xe2F3AsF6
a
b
c
d
e
ln(I°/I) - PRE-EDGE
11.850
11.870
11.890
E(KEV)

Figure IV-9

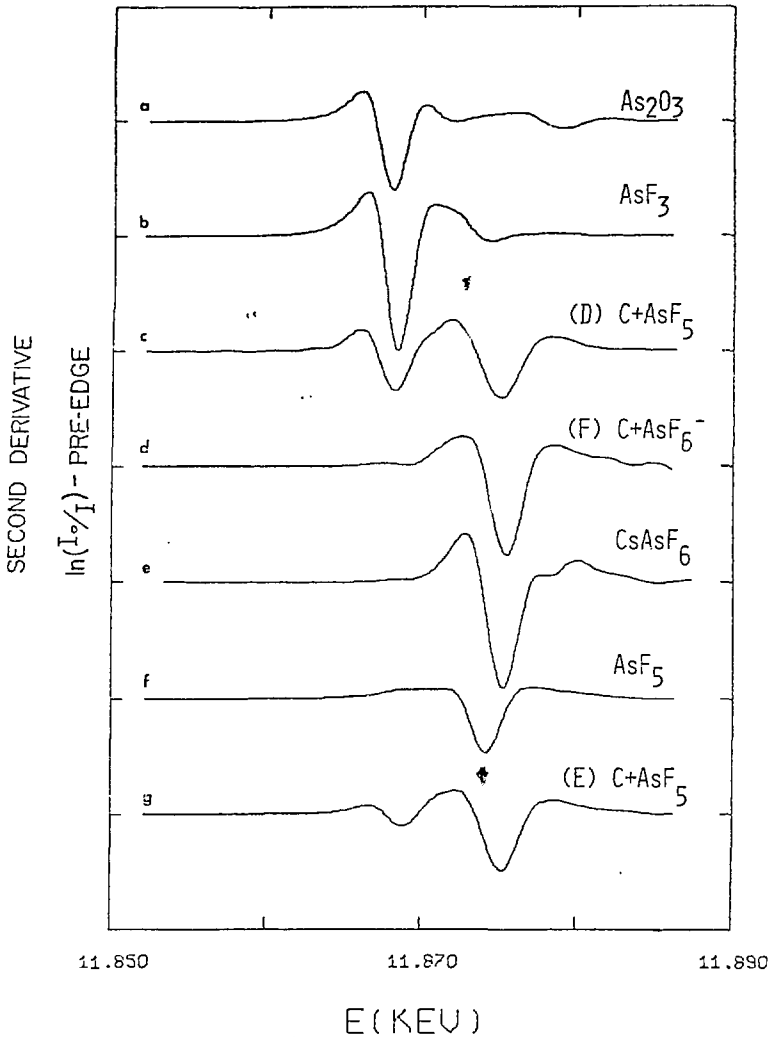
SECOND DERIVATIVE
ln(I°/I) - PRE-EDGE
a
b
c
d
e
f
g
As2O3
AsF3
(D) C+AsF5
(F) C+AsF6-
CsAsF6
AsF5
(E) C+AsF5
11.850
11.870
11.890
E(KEV)

Figure IV-10

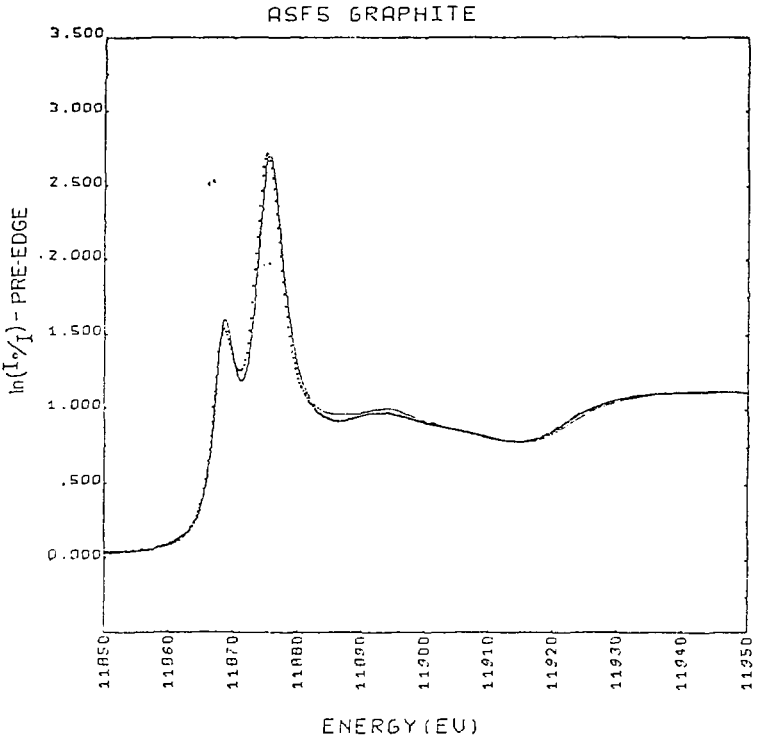
ASFS GRAPHITE
3.500
3.000
2.500
2.000
1.500
1.000
.500
0.000
ln(I°/I) - PRE-EDGE
11850
11860
11870
11880
11890
11900
11910
11920
11930
11940
11950
ENERGY(EV)

Figure IV-11

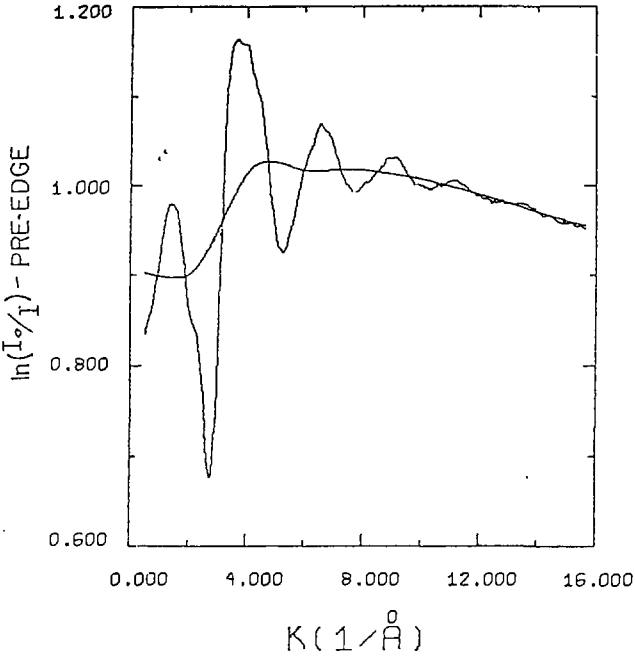
1.200
1.000
0.800
0.600
ln(I°/I) - PRE-EDGE
0.000
4.000
8.000
12.000
16.000
K(1/Å)

Figure IV-12

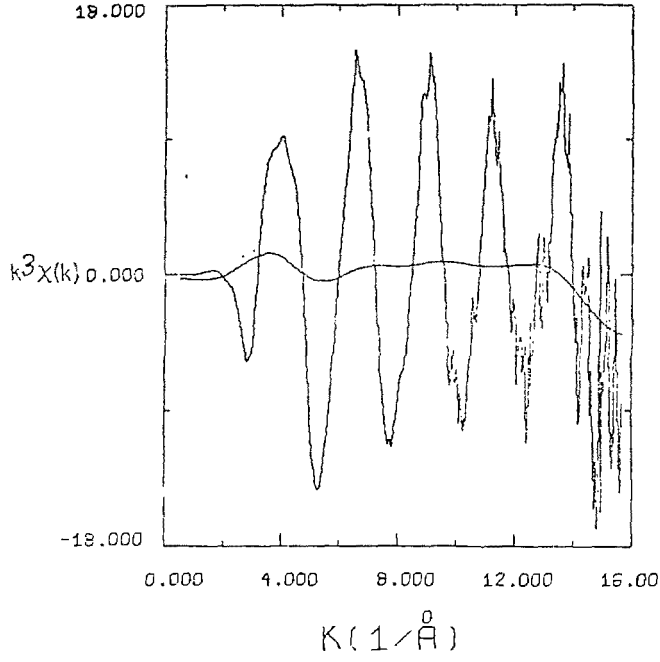

Figure IV-13

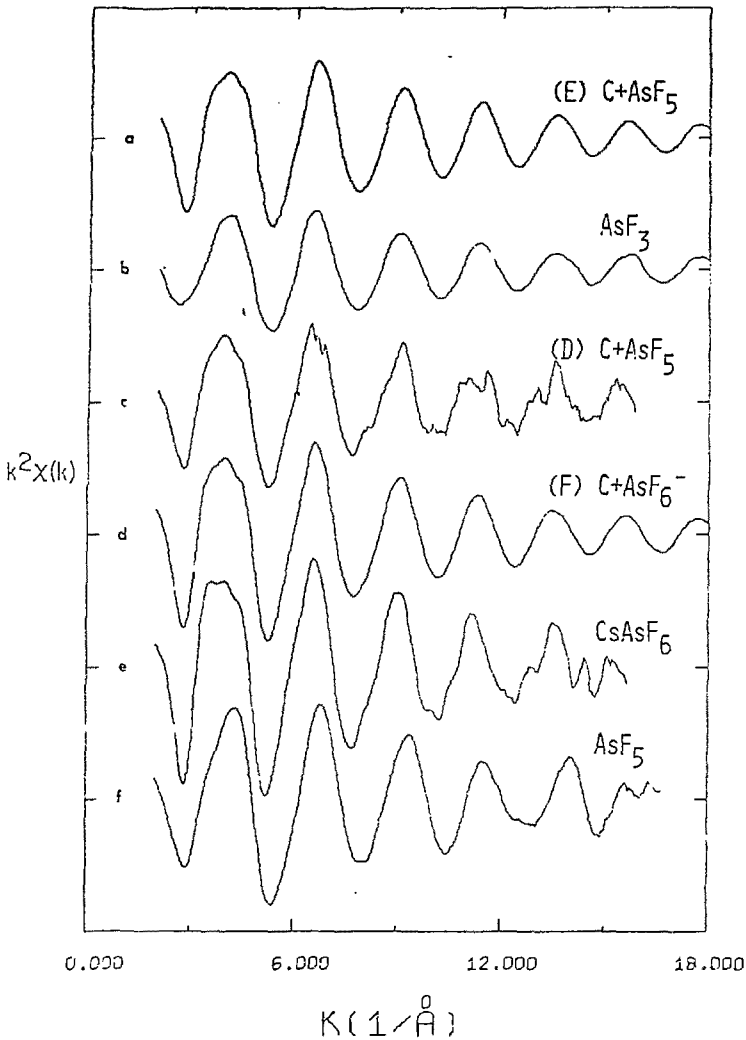
(E) C+AsF5
AsF3
(D) C+AsF5
(F) C+AsF6-
CsAsF6
AsF5
a
b
c
d
e
f
k2χ(k)
0.000
6.000
12.000
18.000
K(1/Å)

Figure IV-14

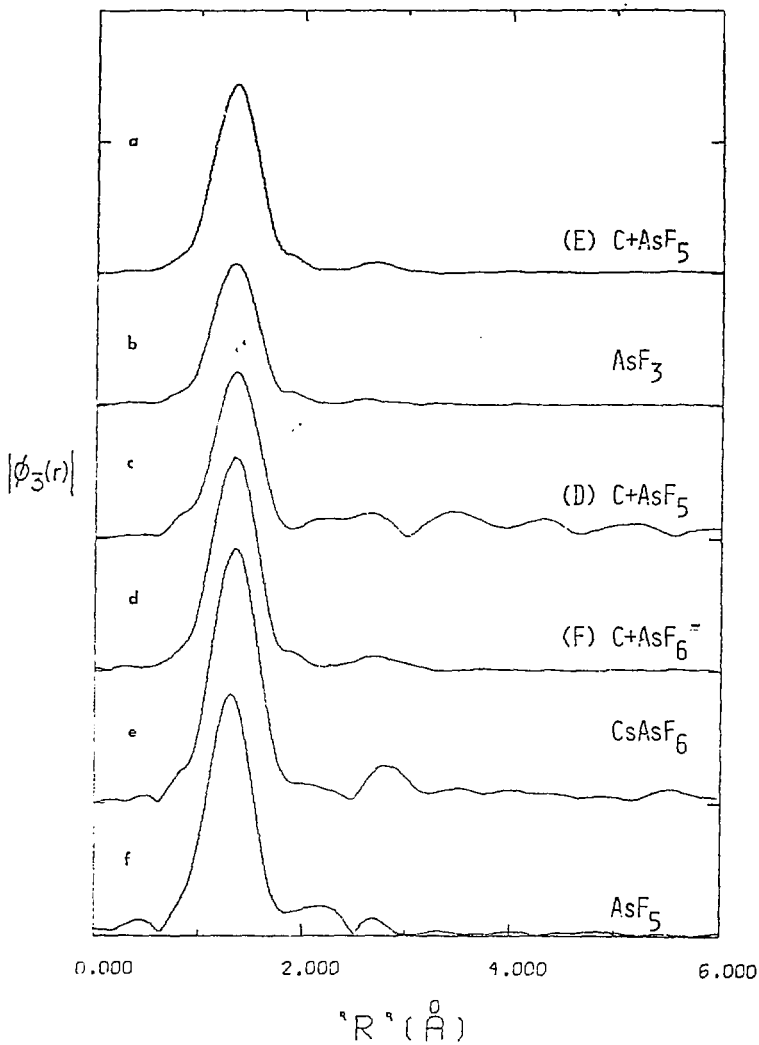
a
(E) C+AsF5
b
AsF3
c
(D) C+AsF5
d
(F) C+AsF6
e
CsAsF6
f
AsF5
|φ3(r)|
0.000
2.000
4.000
6.000
"R" (Å)

Figure IV-15

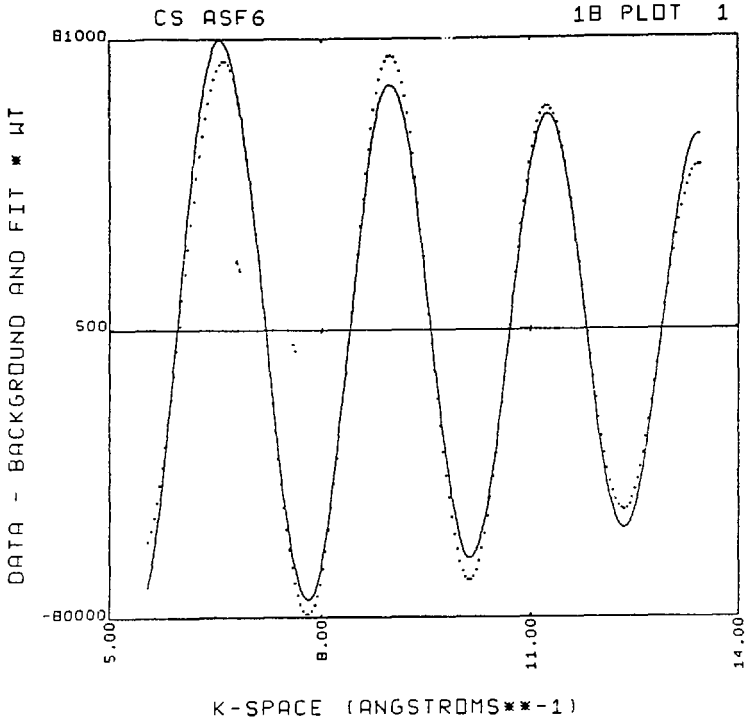

XBL 798-10752

Figure IV-16

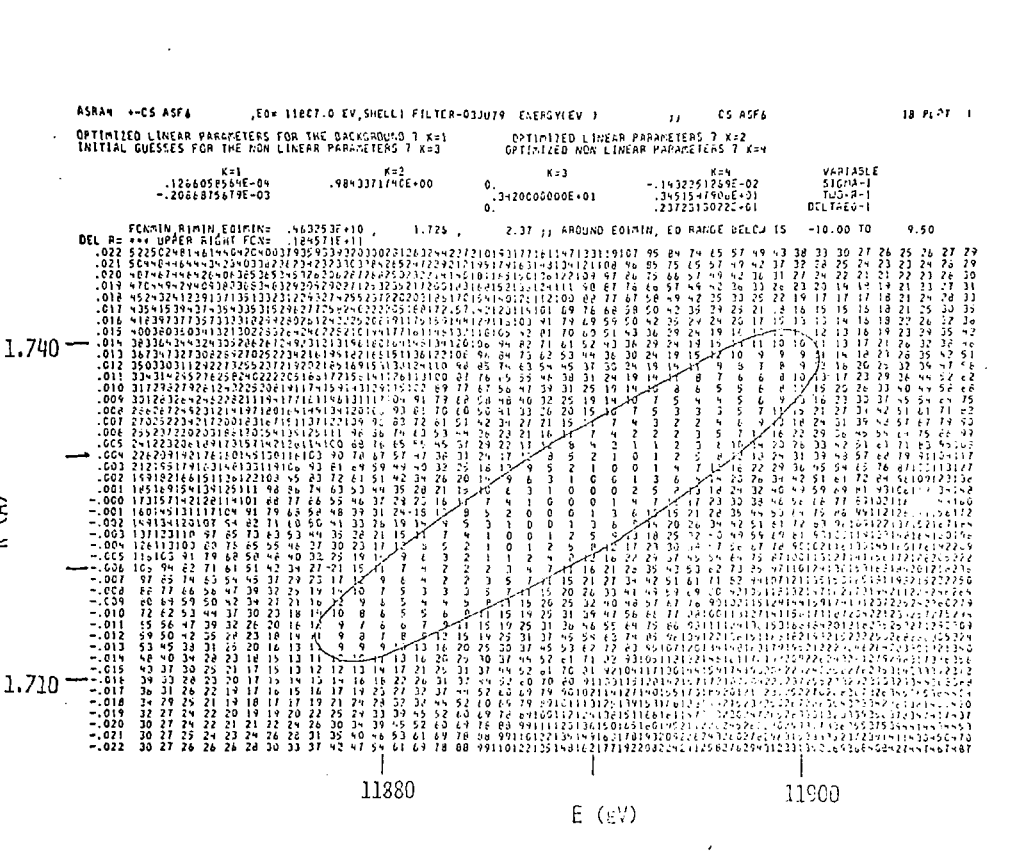
ASRAM +-CS ASF6
,E0= 11807.0 EV,SHELL1 FILTER-03JU79 ENERGY(EV)
CS ASF6
18 PLOT 1
OPTIMIZED LINEAR PARAMETERS FOR THE BACKGROUND 7 K=1
INITIAL GUESSES FOR THE NON LINEAR PARAMETERS 7 K=3
OPTIMIZED LINEAR PARAMETERS 7 K=2
OPTIMIZED NON LINEAR PARAMETERS 7 K=4
K=1
K=2
K=3
K=4
VARIABLE
SIGMA-1
TLS-A-1
DELTAEV-1
.1266059569E-04
-.2068875679E-03
.9843371740E+00
0.
.3420000000E+01
0.
-.1432251269E-02
.3451547900E+01
.2372515022E-01
FCNMIN,RIMIN,EDIMIN= .4632537E+10 , 1.725 , 2.37 ;; AROUND EDIMIN, EO RANGE DELCU IS -10.00 TO 9.50
DEL R= *** UPPER RIGHT FCN= .1245718E+11
1.740
1.710
R (Å)
11880
11900
E (eV)

Figure IV-17

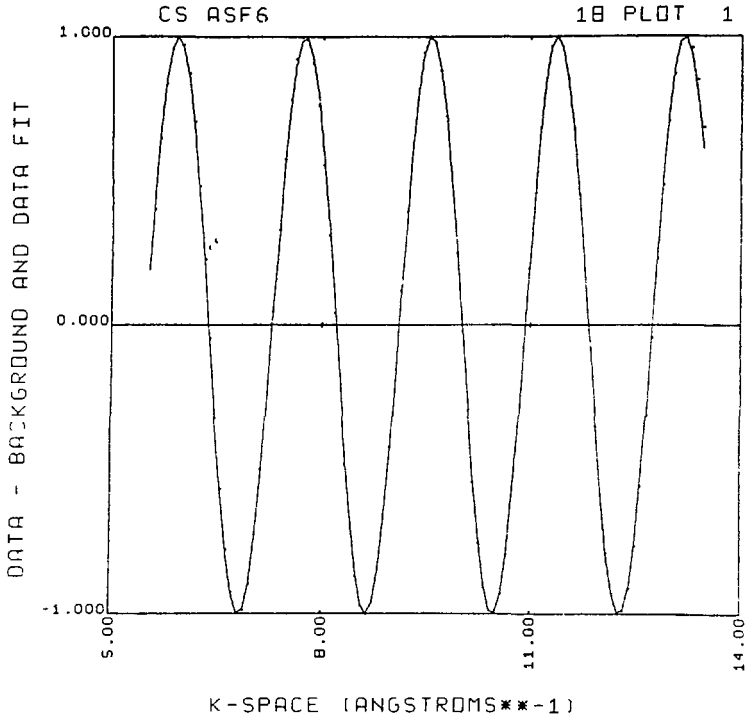

XBL 798-10751

Figure IV-18

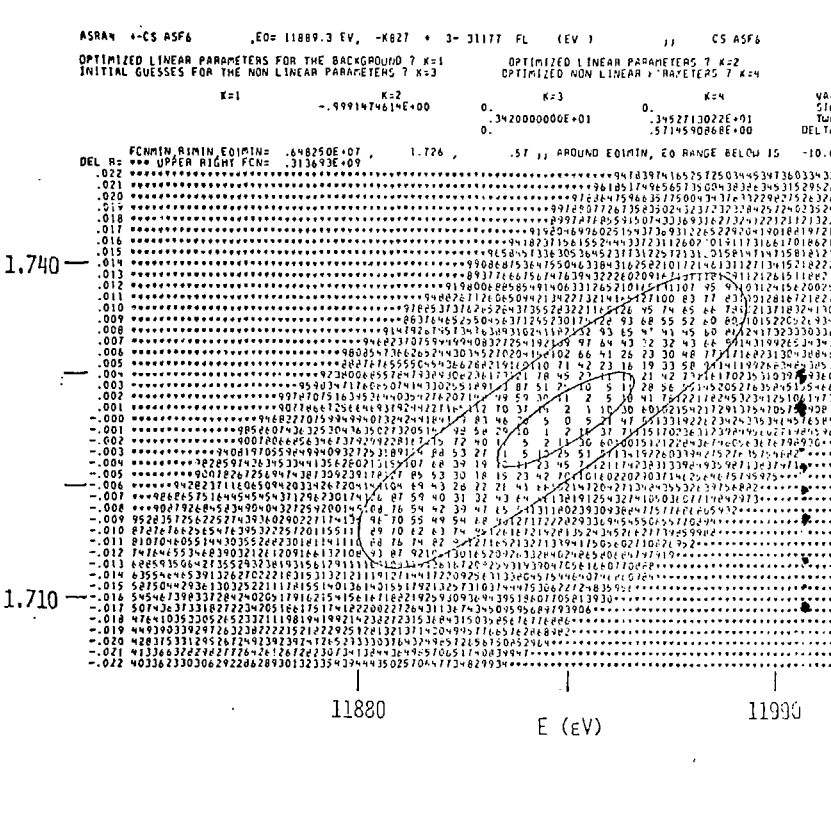
ASRA4 4-CS ASF6 ,EO= 11889.3 EV, -K827 + 3- 31177 FL (EV) ,, CS ASF6 18 PLOT 1
OPTIMIZED LINEAR PARAMETERS FOR THE BACKGROUND ? K=1
INITIAL GUESSES FOR THE NON LINEAR PARAMETERS ? K=3
OPTIMIZED LINEAR PARAMETERS ? K=2
OPTIMIZED NON LINEAR PARAMETERS ? K=4
K=1
K=2
-.999194746194E+00
K=3
0.
.3420000000E+01
0.
K=4
0.
.3452713022E+01
.5714590868E+00
VARIABLE
SIGMA-1
TWO-R-1
DELTAEO-1
FCNMIN,RIMIN,EDIMIN= .648250E+07 , 1.726 , .57 ,, AROUND EDIMIN, EO RANGE BELOW IS -10.00 TO 9.50
DEL R= *** UPPER RIGHT FCN= .3136931E+09
1.740
1.710
R (Å)
11880
11900
E (εV)

Figure IV-19

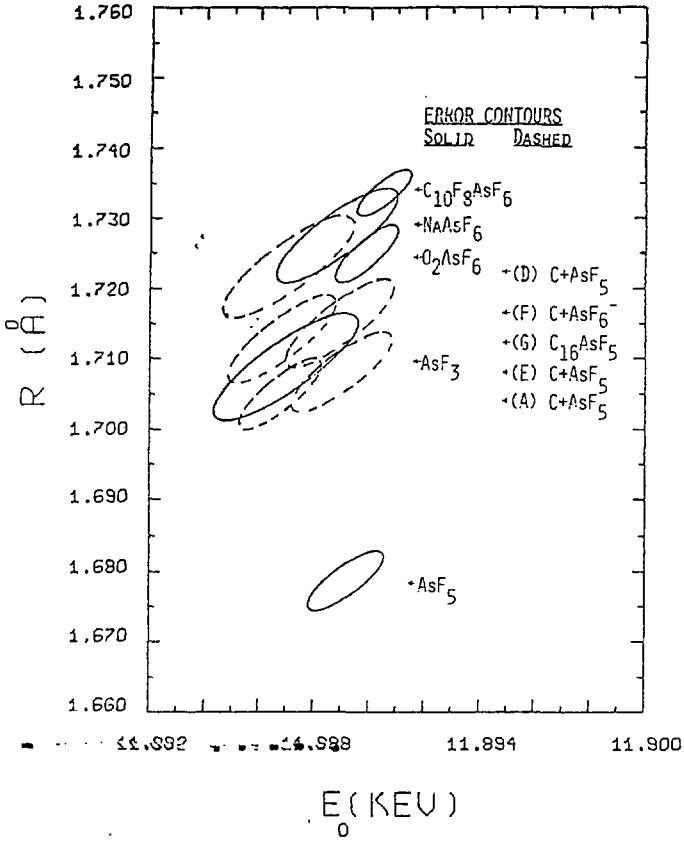
1.760
1.750
1.740
1.730
1.720
1.710
1.700
1.690
1.680
1.670
1.660
R (Å)
ERROR CONTOURS
SOLID DASHED
C10F8AsF6
NaAsF6
O2AsF6
(D) C+AsF5
(F) C+AsF6-
(G) C16AsF5
AsF3
(E) C+AsF5
(A) C+AsF5
AsF5
11.894
11.900
E0(KEV)

Figure IV-20

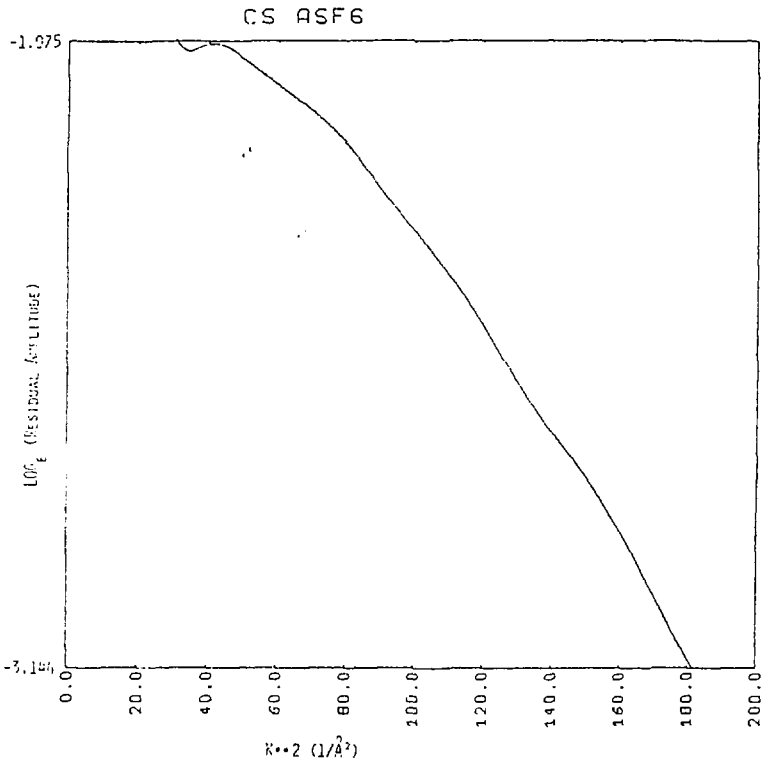
CS ASF6
-1.975
-3.184
0.0
20.0
40.0
60.0
80.0
100.0
120.0
140.0
160.0
180.0
200.0
K**2 (1/Å²)

Figure IV-21

POTENTIAL SPECIES PRESENT IN GRAPHITE

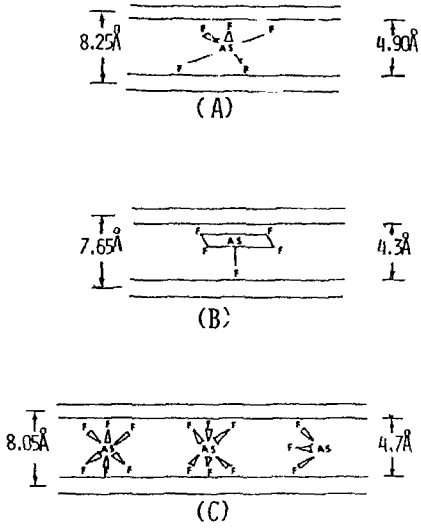

$$3\,AsF_5 + 2\,e^- \longrightarrow 2\,AsF_6^- + AsF_3$$

DEGREE OF OXIDATION
F = NUMBER OF e^- REMOVED FROM GRAPHITE PER As

F = 0

F << 1

F = 2/3

XBL 798-10815

Figure IV-22

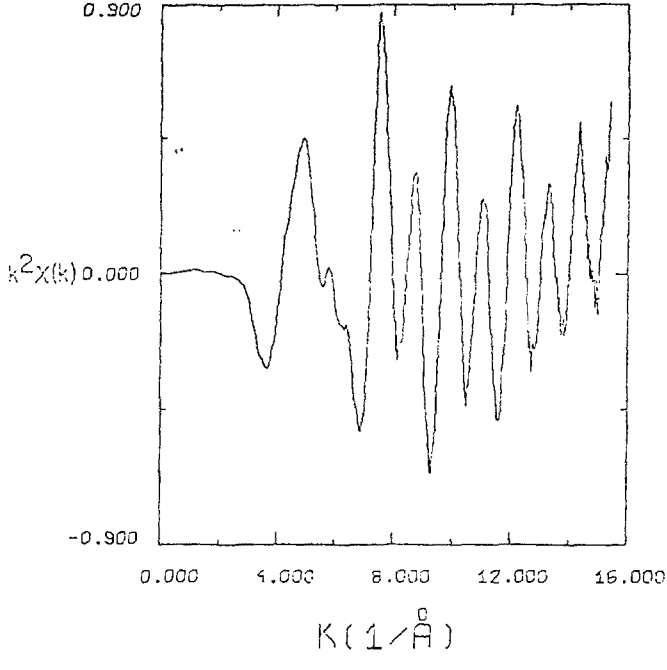

Figure IV-23

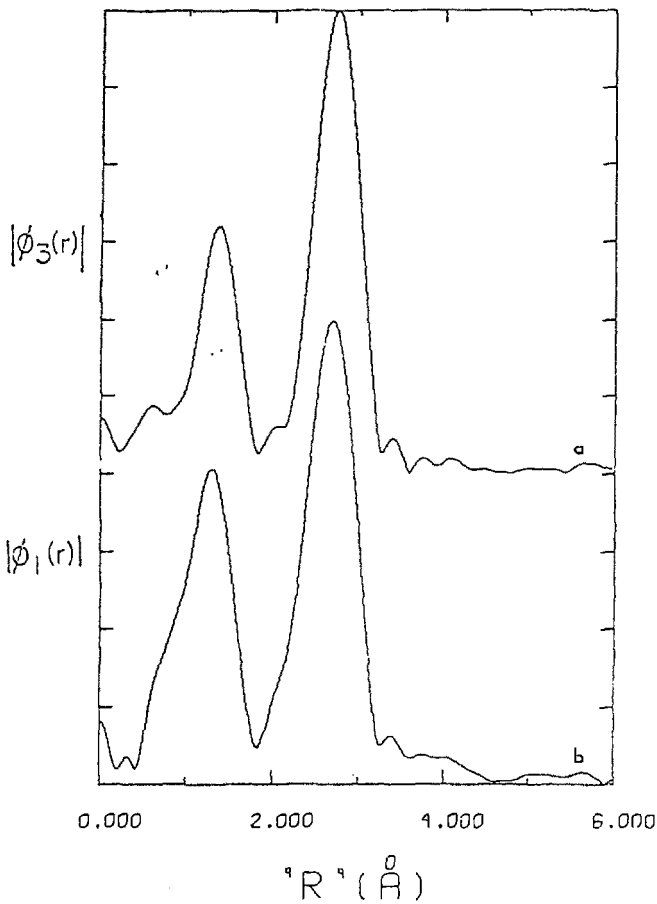

Figure IV-24

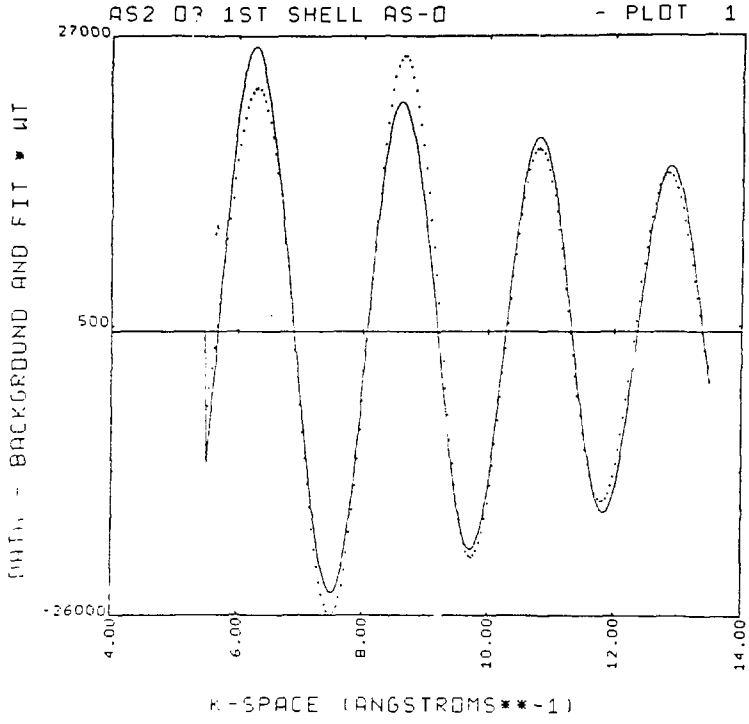

XBL 798-10753

Figure IV-25

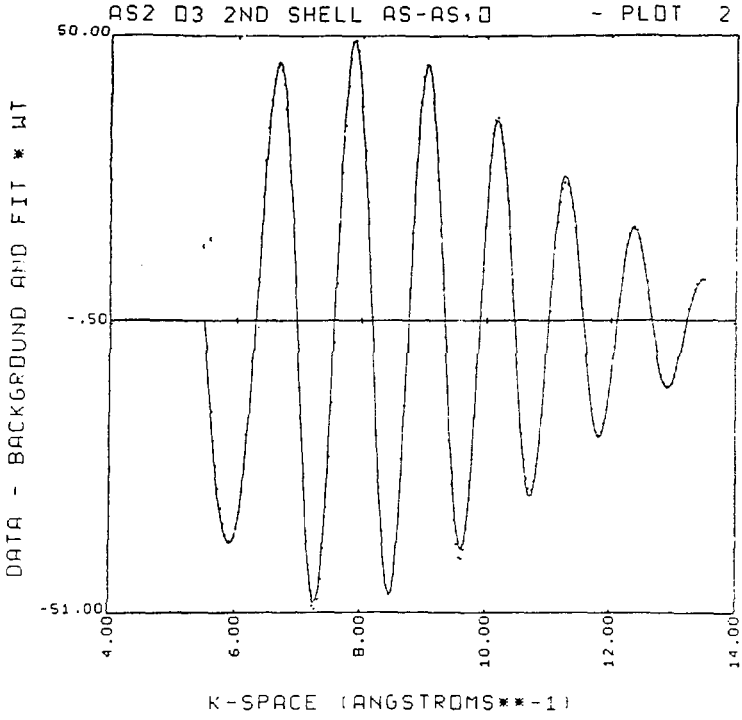

XBL 798-10755

Figure IV-26

References
Chapter IV

1. N. Bartlett, B. McQuillan, and A. S. Robertson, Mat. Res. Bull. (1978) 13, 1259-1264.

2. N. Bartlett, R. N. Biagioni, G. McCarron, B. McQuillan, and F. Tanzella; "Salts of Aromatic Cations and Related Graphite Salts," Molecular Metals, ed., W. Hatfield, Plenum Publishing Co. (1979).

3. A. Zalkin, D. L. Ward, R. N. Biagioni, D. H. Templeton, and N. Bartlett; Inorg. Chem (1978) 17, 1318.

4. N. Bartlett, et al.; Inorg. Chem. (1974) 13, 780.

5. R. G. Shulman, Y. Yafet, P. Eisenberger and W. Blumberg; Proc. Nat'l. Acad. Sci.-USA (1976) 73, 1384-1388.

6. J. V. Acrivos; unpublished data.

7. D. H. Templeton; unpublished data.

8. T. K. Eccles; Ph. D. Thesis, Stanford University (1978).

9. B. K. Teo and P. A. Lee; J. Am. Chem. Soc. (1979) 101, 2815.

10. J. A. Kirby, A. S. Robertson, M. P. Klein; (in preparation).

11. F. B. Clippard, Jr., and L. S. Bartell; Inorg. Chem. (1970) 9, 805-811.

12. J. A. Kirby; Ph. D. Thesis, University of California, Berkeley (in preparation).

13. P. Eisenberger and G. S. Brown; Solid State Comm. (1979) 29, 481-84.

14. J. A. Ibers; Acta Cryst. (1956) 9, 967-969.

15. N. Bartlett, E. M. McCarron, B. W. McQuillan, and T. E. Thompson; submitted to Synthetic Metals.

16. S. H. Hunter; Ph. D. Thesis, Stanford University (1977).

17. Almin and Westgren, Ark Kemi Min. Geol. 1513, 1-7.

References, Chapter IV, continued

18. L. R. Hanlon, E. R. Falardeau, and J. E. Fischer; Solid State Comm. (1977) 24, 377-381.

19. F. L. Vogel; private communication.

20. L. V. Interrante; private communication.

Chapter V

RB K-EDGE XAS EXPERIMENTS

In this chapter, the XAS experiments performed on metal-ammonia solutions will be described. The manner in which we studied the metal-ammonia solutions will be discussed. The sample preparation done and the experiments performed will be described in Section A. The XAES and EXAFS analysis performed on metal-ammonia will be described in Sections B and C, respectively. Comparisons of XAES and EXAFS data and the conclusions which can be drawn from these experiments are contained in Section D.

A. Sample Preparation and Experiment

Material Preparation

The preparation of Rubidium-ammonia solutions is similar to the preparation of other metal-ammonia solutions (1). The Rb-NH_3 samples were prepared in vacuum by first distilling a known weight of Rb into the side arm of a sample tube and then distilling the required volume of NH_3 from a $NaNH_3$ solution. The pyrex sample tubes had previously been aged in HF, passed through a hot cleaning solution, and then steamed and dried in the absence

of dust.

Once the samples were prepared, they were stored at dry ice temperature. No decomposition of the samples was noted when they were warmed to room temperature. In fact several of the samples survived in cold storage for six months. They were re-used at that time for more XAS experiments. No decomposition was noted and the data were similar to the data obtained 6 months earlier.

In the early stages of sample preparation, several samples were broken or exploded. These losses may be attributed to contaminated samples, defects in the glass or poorly made cells. Several cells were discovered broken when they were removed from long term storage at dry ice temperature. This could be due to a slow decomposition of the samples or mechanical stress on the cells when handling them or their storage container. All samples, except E and G, broke within six months after the XAS experiment.

The samples run were carefully prepared and stored. Pyrex glass was chosen in order to minimize decomposition. All the samples displayed the blue color, which is characteristic of metal-ammonia solutions, for weeks after the sample was run. Decomposition of the samples used was not observed.

Sample Cells

Several different types of sample cells were designed. As our experimental technique improved, the design of the cells changed. The sample cells described first are the cells used for samples

E, F, G and H. After this description, the differences between these cells and those used for samples A, B, C, and D are discussed.

The cells were made from Wilmad precision rectangular Pyrex tubing. The inside rectangle of the tubing was 0.6 cm by x. The thickness, μx, of the cell was varied from 0.1 cm to 0.5 cm so that differing concentrations of metal in solution could be studied. This variable thickness is oriented in the direction that the X-Ray beam travels. It was chosen so that the X-ray absorbance, μx, of the sample just above the Rb absorption edge was about 0.1. This choice produced the optimum signal-to-noise ratio. The two Pyrex walls (3 cm by 0.5 cm) through which the X-Ray beam travelled were ground and etched on the exterior of the cell. This operation reduced the absorption of the X-Rays in the glass. The wall thickness achieved was about 0.03 cm which corresponds to an absorbance, μx, of about one for both glass thicknesses at the Rb X-edge.

The ends of the Pyrex tubing were closed by heating the glass. A fill tube was attached on the top of the cell so that the glass sample cell could be attached to a vacuum line. After the metal-ammonia solution was transferred to the sample cell, the cell was detached from the vacuum line by heating and sealing the fill tube. In order to protect the sample, the main body of the cell containing the sample was immersed in liquid nitrogen during this process. The sample cell mounted on the dewar is shown schematically in Figure V-1. 5 samples were mounted on the dewar.

The basic difference between the cells just described and those used for samples A, B, C and D is that the outside walls were not reduced in thickness. Thus more than 90% of the X-Ray beam was absorbed in the glass as opposed to 35% for the cells just described. Thus, the signal-to-noise ratio is poor for these samples. In addition, incorrect metal concentrations were used for samples A and B. For this reason and other experimental problems, no significant data were obtained from these two samples.

Figure V-2 shows a plot of the inverse of the linear absorption coefficient, $(1/\mu)$ versus atomic number, Z. Note that for Rb, Z = 37, $1/\mu$ = 0.06 cm, or twice the thickness of one wall. In addition, $(1/\mu)$ is plotted versus the mole ratio of ammonia to metal, $R = [NH_3]/[M]$ for M = Rb and Sr. The curves were evaluated from tabulated values of mass absorption coefficients (2).

Figure V-2 graphically indicates the reason why Rb and Sr are the elements with the lowest atomic numbers whose ammonia solutions can be studied using XAS. The pyrex glass is much too thick to conduct experiments with metal-ammonia solutions with a metal which has a Z much lower than Rb. Furthermore, until recent X-Ray flux improvements, Rb and Sr were the heaviest elements accessible. This was due to a lack of X-Ray flux at the K-edges for heavier metals.

Experimental Dewar

The dewar used for Samples E, F G and H is outlined in Figure V-1 with front and back views. Nitrogen gas flowed through a heat exchanger immersed in liquid nitrogen and then into the heater

element of a Varian V-4343 temperature control. This element is shown on the back side diagram of Figure V-1. The gas circulated through copper tubing attached to the ¼" copper block. The controller was used to control the temperature to ±1 K during experimental runs. Two pieces of one-inch thick styrofoam were mounted around the plate to insulate the copper block and samples.

The sample cells were mounted on small shelves and held in place via spring loaded clips on the front of the copper block. Three thermocouples at points A, B and C were used to monitor the temperature of the samples. It is important to note that these thermocouples were not in direct thermal contact with the copper block and that all three closely agreed in temperature throughout all experimental scans. Thus they are a good measure of the sample's true temperature Note that the cell holds 5 samples at the same time so that one can run several different samples at the same temperature without dismantling the dewar.

For samples A, B, C and D, a smaller dewar was used which held only one cell at a time. This severely limited data collection. For this reason, the dewar in Figure V-1 was designed. Since the smaller dewar maintained the sample temperature as well as the one shown in Figure V-1, it will not be described.

Experimental Runs

For the early experiments, a range of temperatures were explored so that the effects of temperatures on XAS features could be studied. Each of the samples was individually mounted in the smaller sample dewar mentioned above.

For the run on samples A and B and the first two runs on samples C and D, a wide range of temperatures were explored. The temperature range covered was 202 K to 284 K. As was mentioned above, no significant data were obtained from samples A and B because the signal-to-noise ratio was poor.

For Run 3 on sample D, multiple scans were taken at three different temperatures, 217 K, 242 K, and 263 K. This was done so that better EXAFS could be obtained than was obtained during Runs 1 and 2. In addition, care was taken so that the energy calibration of the monochromator was known throughout the run. The position of the edge versus temperature was studied in addition to other XAS features. This is only run in which we were able to maintain this calibration within the necessary accuracy, ± 0.1 eV, to obtain an accurate measurement of the edge position. For earlier runs, we were not careful enough. For later runs, the calibration of the monochromator was slipping due to a slippage in the mechanical drive. These problems only affected the position of the edge and did not affect comparisons of other XAS features.

Samples E, F, G and H were mounted in the dewar outlined in Figure V-1. Scans were taken at two different temperatures, 197 K and 228 K. For the higher temperature, only edge (XAES) data were obtained while both XAES and EXAFS data were obtained at the lower temperature.

Standard Compounds

RbN_3 and RbBr compounds were obtained from Alfa Chemical. The samples were powdered and mixed with a binder, cellulose acetate.

They were then pressed into the 1¼" diameter pellet which was placed in a plastic holder for protection.

Rb-metal was evaporated into one of the sample cells used for metal-ammonia solutions. It was highly reflective and silver in color. The cell was removed from the vacuum apparatus in the manner described above.

Scan Parameters

The standard scan used to obtain data is described here. Data points were taken at 20 eV intervals from about 420 eV to 20 eV below the edge inflection. Data points were taken at 0.3 eV intervals from 20 eV below the inflection point to 30 eV above the inflection point. For the early data scans and samples A through D, all the data (except part of Sample D, Run 3) were taken using using a 0.6 eV interval. This is sufficiently fine as the features in the edge region of the Rb samples vary much more slowly than 0.6 eV. From about 30 eV above the edge to about 150 eV above the edge, points were taken at 3.0 eV intervals. This is an adequate sample of the EXAFS region. The range in energy is shorter than is normally used above the edge. In every sample, no EXAFS was visible above the noise level at 600 eV above the edge. This is due to three factors present in all Rb samples:

- large thermal motion parameters
- first shell bond distances of more than 3 Å
- first shell scatterers of nitrogen.

Conductivity and Phase Separation of $Rb-NH_3$ Solutions

The conductivity and phase separation data presented in this section were measured by Sharp et al. (3). Figures V-3, 4 and 5 are plots of the conductivity and phase separation of the $RbNH_3$ solutions. The bold letters C, D, E, F, G and H indicate sample concentrations where data were taken and analyzed for this work.

Figure V-3 is a plot of conductivity versus temperature for two different concentrations. Figure V-3a is a plot of conductivity versus temperature for a sample with the same concentration as sample D. The data taken on samples C and D were taken at temperatures from T = 205 K and up as indicated on Figure V-5. The conductivity change for this temperature range is indicated in Figure V-3. The position of the edge was observed to increase and the density of the rubidium was observed to decrease as the temperature increased for sample D.

Figure V-4 is a plot of conductivity versus concentration for several different metal-ammonia solutions. The bold letters indicate the different concentrations at which EXAFS data were obtained. Figure V-5 shows a phase diagram for $RbNH_3$ solutions. The bold letters indicate the concentration and temperature at which data were obtained. Figures V-3, 4, and 5 show that the XAS sample concentrations and temperatures studied investigated the region in and near the metal-insulator phase separation and phase transition.

The next three sections discuss the results and conclusions derived

from these experiments.

B. XAES Analysis

Analysis of edge features included a qualitative comparison of the edge features evident in the original data and in the second derivative spectra.

Figure V-6 shows a raw spectrum plot of absorbance, μx, for $RbNH_3$, sample E. There were no crystal "glitches" removed from any of the Rb data files.

As discussed in Chapter III, a pre-edge strip was done across about 150 eV of data below the onset of the absorption. Formally, only absorption from the Rb K-shell remained after the subtraction. In practice, small residual background remained from other edges and from the detector backgrounds. These were small in the 50 eV of data which were studied for XAES analysis. For EXAFS analysis, [illegible] background was removed, and the residual background which remained here did not affect that data analysis. The data files were then normalized to an edge height of 1.0. Using the formalism of Chapter III, the function is now $\mu_I^*(E)$ where E is the photon energy. For sample G, μ_I^* is plotted in Figure V-7.

An example of an edge spectrum, its first derivative, and its second derivative are shown in Figure V-8. These spectra have been pre-edge stripped and post-edge normalized as described in Chapter III. A quantitative comparison of the features indicated on Figure V-8 has been done. H_p is the height of the 1s to 4p transition peak with the edge height $\Delta(\mu)$ normalized to 1.0. E_p is the position of

the peak, which is defined as the zero crossing in the first derivative. E_I is the major inflection point in the onset of the edge, which is defined as the zero crossing in the second derivative. $\Delta_P = E_P - E_I$ is the edge width. Since a small shoulder was evident in the region of the inflection point, a low resolution derivative was used to estimate E_I and E_P. In order to calculate the first derivative, a quadratic was fit through the data within 3.0 eV of each point. The analytical derivative of that quadratic function was an estimate of the true derivative for each data point. The process was repeated on the first derivative file to obtain the second derivative. In addition, since the sample thickness, t, is known, the density of the metal in solution, $D_X = \rho_{A/t}$, can be compared. As discussed in Chapter III, ρ_A can be calculated from the size of the edge jump, $\Delta(\mu x)$, using the equation

$$\rho_A = \frac{\Delta(\mu x)}{\Delta(\sigma)}$$

where $\Delta(\sigma)$ is the change in cross section in traversing the edge listed in the McMaster tables (2). $\Delta(\mu x)$ is obtained from the data by subtracting the pre-edge fit from the post-edge fit each extrapolated to E_C = 15208 eV. E_C is an estimate of the onset of the continuum using the atomic states of Charlotte Moore's Tables (4).

Changes in each one of these quantities have been observed to correlate well with the known properties of Rubidium metal-ammonia solutions. However, experimental difficulties, primarily with the monochromator system, limited the usefulness of some of

the data obtained.

Data from samples A and B will not be presented. The low intensity of the X-Ray beam coupled with the thickness and concentration of the samples caused the data to be of insufficient quality to yield significant results.

Qualitative Discussion of Second Derivatives

Figure V-9 is a plot of the second derivatives of the Rb-ammonia solution edges. There is a significant difference in these files between 15190 and 15200 eV. These differences are caused by the presence of other small transitions in addition to the large major absorption onset. In comparing these plots, bear in mind that the monochromator was slipping slightly from scan to scan. Corrections were made, but some changes in the absolute position of an edge feature may be due to this slippage. Only relative changes should be considered. In this light, a shoulder appears to move in the direction of higher energy as the sample becomes higher in conductivity. This change could also be due to changes in the intensity of a transition. From published diagrams of conductivity and phase separations, reproduced in Figures V-3, 4 and 5, a qualitative comparison can be made. Data presented later indicate that the metallic phase of the phase separated solution was observed for sample F at 197 K as would be expected since Figure V-5 indicates that sample F is in the phase separation region. The conductivity estimates are listed below for these samples so that they can be compared with Figure V-9.

σ_a (E at 228 K) > $\sigma_{a'}$(E at 200 K)

> $\sigma_{b'}$(F at 197 K) > σ_b (F at 228 K)

> σ_c (G at 228 K) > $\sigma_{c'}$(G at 197 K)

> $\sigma_{d'}$(H at 197 K)

Note also that sample G at 197 K in Figure V-9c' has a much larger negative peak in the second derivative. This may be an indication of the differences one would see in the edge spectrum when the sample is on the phase-separation contour. Our measurements of temperature and density indicate that sample G was run on the phase-separation boundary as shown in Figure V-5.

Figure V-10 shows a plot of the second derivative of Sample D at three different temperatures. The resolution and poorer signal-to-noise ratio for this file made it impossible to extract information about the small shoulders observed in Figure V-9. These were the only data taken in which the monochromator slippage problem did not occur. The absolute position of the edge is therefore meaningful. The position of the inflection point is discussed next.

Inflection Point (E_I)

Only Run 3 of Sample D was of sufficient quality to obtain information on the position of the inflection point. We were able to obtain consistent data accurate to $\pm$0.1 eV. On all other runs the monochromator calibration slippage, mentioned in Chapter III, masked any effect of changes in concentration or temperature. For sample D, several experimental runs were used as monochromator

calibration between beam fills.

The inflection point for Run 3 of Sample D is plotted in Figure V-11. The straight line is the best fit through the 11 data points. The correlation coefficient of the fit is 0.972. The fit is $E_I = a + b\ T$ where T is the temperature in Kelvin and

$a = 15186.31\ (3)$ eV and

$b = 0.0309\ (10)$ ev/K .

(The estimate of the error in the last place of the fit results is enclosed in parentheses.)

Since the conductivity increases and density decreases as the temperature is increased (1), this change must be the cause of the increase in the inflection point position. As noted above, the absorption rise occurs at lower energy in Rb-NH_3 compounds than in Rb metals. This, in addition to the small shoulder in the absorption rise, indicates the presence of other transitions which change intensity or position as a function of concentration and temperature. In contrast to these data, the onset of the edge usually decreases in energy as the samples become more metallic (5). In fact, we note that RbN_3, an insulator, has an onset at a higher energy. Therefore, the states may be attributable to excitonic transitions in the bond gap of a semi-metal since they are not explained by the standard explanation.

D_M, H_P and Δ_P

Table V-I lists the quantitative XAES results of samples C through H. For samples D/Run 3, E, F, G and H, the density of Rb metal (D_M), the height of the peak (H_P), and the edge width (Δ_P)

are listed separately for each temperature run. For Runs 1 and 2 on samples C and D these quantities are listed as an average of the values of scans at different temperatures spanning the range of temperatures listed. The different temperatures used are evenly spaced throughout these regions. These average values are presented for comparisons with other results. No statistically significant changes were noted in H_P and Δ_P for samples C and D. Therefore, complete data as a function of temperature are not presented.

Statistically significant dependence of D_M versus T will be presented later for samples C and D. The results for D_M, H_P and Δ_P will be discussed separately.

The estimated concentration (C) of the samples in Mole Percent Metal (MPM) is listed. This is a rough estimate which is calculated from D_M assuming that the volume of Rb (V_M) is 40 cm^3 per mole of Rb. The number of measurements for each line of data is listed as N. The error bars for D_M, H_P and Δ_P are the standard deviations of these N values.

Note that the data from Runs 2 and 3 were taken using a poorer resolution crystal. This fact caused the edge width Δ_P to increase and the peak height H_P to decrease. Therefore these data cannot be compared with the data taken with the better monochromator. Additionally, differences may occur due to smaller changes in resolution from day to day using the same monochromator. Therefore, accurate comparisons can only be made within the same run. There are four runs represented on Table V-I. Samples E, F, G and H were all Run 4.

Density, D_M

Figures V-12 and V-13 show the plot of the $\log_{10}(D_M)$ versus 1/T for the data of Samples C and D, respectively. These values can be fitted to a semi-empirical relation indicated by the solid lines. The results of this fit are contained in Table V-II where the equation fit was

$$\log_{10}(D_M) = a_o + a_1(1/T) + a_2(1/T)^2$$

The errors in these values are large, but they are in apparent agreement with the values of a_2 as calculated from measurements of the volume of the solution. For several different metal-ammonia solutions, Thompson et al. (6) found that a_2 was between -1.2 and -2.1. As shown in Table V-II, our measurement of a_2 is -2.8 $\pm$ 0.9. Thus the XAS experiment provides a new manner by which to investigate density fluctuations which occur near the critical points of the metal-insulator transition.

Note that in Table V-I the densities (D_M), except for sample F, of the solutions increase when the temperature is lowered. This increase is more evident when the percent increase is plotted as in Figure V-14. Here the percent density increase from the highest temperature run is plotted. For sample F, however, the density decreases dramatically (by 25%). Samples D, E and G increased only 2 to 6%. The cause of this anomaly is that concentration, C = 2.7 MPM, and temperature, T = 197 K, place the sample within the phase-separated region of Rb-NH_3 as shown in Figure V-5. Since the lighter phase of the metal-ammonia solutions

is the metallic phase, the data taken at 197 K for sample F were taken on the metallic phase of the phase-separated solution.

Peak Height (H_p) and Edge Width (Δ_p)

The data obtained for edge height, H_p, and edge width, Δ_p, for samples E, F, G and H are plotted in Figures V-15 and V-16. Sample E, the most concentrated, is in a metallic phase at both temperatures. All other samples at all temperatures are insulating except sample F at 197 K, as mentioned before. Thus the edge peak is diminishing in size and the edge width increasing as the conductivity of the sample increases. This correlates with the qualitative discussion of the second derivative spectra above.

As the solvated electron grows in size (with increasing concentration or increasing temperature), it begins to include the empty orbitals of the Rb in the conduction band. The Rb edge spectrum thus starts to look less like Rb^+ and more like the Rb^o metal which would not have a peak P at the edge but rather a smooth continuum onset. At a higher conductivity of the metal-ammonia solution, the peak in the edge spectrum should disappear completely. The exact nature of these states which change intensity and the detailed explanation for their change must await more detailed experimental data and theoretical calculations.

C. EXAFS Analysis

Analysis of the EXAFS features followed the methodology presented in Chapter III. Several attempts to remove the backgrounds from the post-edge data failed. A polynomial fit to the background had to be

done simultaneously with an initial fit to the EXAFS data. The following analysis concentrates on finding the radial distance of the first shell Rb-N peak in the $RbNH_3$ solutions.

Background Removal

Figure V-17 shows a raw spectrum plot of normalized post-edge data, μ_I^* versus $k(1/\mathring{A})$ for $RbNH_3$, sample E. The first post-edge background removal, a quadratic fit from 250 eV above the edge to the end of the data, is overplotted on the same figure.

Figure V-18 shows the resultant data. The sharp drop in the background which occurs at about 5.0 $1/\mathring{A}$ is just beyond 100 eV above the edge (E(photon) = 15300). This drop in absorption is believed to arise from two electron events in which both electrons are bound. The M_{IV} and M_V edges of Rb are bound by about 110 eV. The 2-electron process which excites an M-shell electron and a K-shell electron into bound states would no longer occur once the exciting photon energy is greater than about 15310 eV. Two electron processes in which one or both of the electrons is free (shakeup and shakeoff processes) have been shown to have a negligible cross-section until the photon energy is 400 to 800 eV past the edge (8). Therefore, one would expect to see a decrease around 100 eV above the edge as noted. Since no theoretical or other experimental work has yet been published on this effect, it will not be discussed further. The following analysis concentrates on the removal of this background so that the sinusoidally oscillating EXAFS can be analyzed.

Using the theoretical EXAFS calculation of Teo et al. (9), a fit to data in Figure V-18 was performed on all data files. One

nitrogen shell was fit simultaneously with a 10 term Tschebychev polynomial expansion for background removal over the range k = 2.5 to 10.0 1/Å. Any polynomial of an order lower than 10 terms would not follow the background correctly. In addition, the background was tested to show that it did not follow the EXAFS. The background for sample E is plotted with the data in Figure V-18. The resultant file less the background and the EXAFS fit less the background are plotted in Figure V-19 for sample G. All the other files were processed in a similar manner. The parameters for the shell are similar to the final answers listed below. However, the following procedures produced more accurate values for the fit parameters.

Plots Versus Wavevector and Distance

Figure V-20 is a plot of $k^2\chi(k)$ for the six $RbNH_3$ EXAFS samples. Note that the thermal motion term for these samples is large. This is expected for a metal atom dissolved in a solution. Figure V-21 is a plot of the Fourier Transform, $\phi_3(R)$, of $k^3\chi(k)$ for the same six EXAFS scans of $RbNH_3$. The one peak in each file is nearly identical in position to the peak in each of the other spectra. The position of the peak in $\phi_3(R)$ can be used to compare different samples. However, this method is not as accurate nor does it give an absolute distance as does the fitting method described below.

Description of Analysis

The following is a summary of the analysis approach used for each data file. The complete method was described in Chapter III. Starting with $\chi(k) * k^3$ with the background removed prepared with

a given E_o, the theoretical phase was removed and a Fourier Transform computed. E_o was varied until the sine component peak of the transform occurred at the same R-value as the power spectrum peak. This provided an estimate of the E_o which was consistent with the theoretical calculation. This E_o value was used as a starting point for the fitting in k-space.

Using the theoretical amplitude and phase functions, the fitting model is equivalent to

$$F(E) = ae^{\sigma k^2} \sin(2kR)$$

where $k = \left(\frac{2m}{\hbar^2}(E - E_o)\right)^{\frac{1}{2}}$ and A, σ, R and E_o are variables. For a one-shell fit, the data, $\chi(k)$ were Fourier Transformed and filtered so that only the one shell of interest was kept. The initial Fourier Transform was k = 2.3 to 10.5 and the data fitted were k = 3.3 to 9.0 $1/\mathring{A}$.

An example of the fit and data is plotted in Figure V-22. The phases of the two files are quite similar. However, the amplitudes do not agree as well. This is true for all the data files. The procedure described in the next paragraph improved on these distance values. In order to get an estimate of error in R, E_o and R were varied around their best fit values. The least square error, $\Sigma(D - F)^2$, between the data (D) and the fit (F) is plotted in Figure V-23. The contour was drawn for a 100% increase in this error above its minimum value. The projection of this error ellipse onto the R and E_o axis provided an estimate of the error in R and E_o. Tables V-III and V-IV report the results of

these fits with the $e^{\sigma k^2}$ term. The distance R, with error estimates, is listed in column 4 of Table V-III. The values of A, σ, and E_o are listed in columns 5, 6 and 7 of Table V-IV. Error estimates for E_o are included. These results will be discussed later.

Tables V-III and V-IV also have results of fits with the total amplitude removed. The data used in these fits were prepared by Fourier isolating the first shell of the data $\chi(k)$. The total amplitude function and then the theoretical phase function were removed from the data. The fitting function is now:

$$F(E) = A \sin (2kR)$$

where $k = \left(\frac{2m}{\hbar^2} (E - E_o) \right)^{\frac{1}{2}}$

The amplitude, A, is a variable which should be and is close to 1.0.

A plot of the data and fit is shown in Figure V-24. The agreement is excellent. Figure V-25 is an error plot similar to Figure V-23. The 100% and 1000% increase in error contours are plotted. The 100% error contour provides an error estimate. Tables V-III and V-IV report the results of these fits on all the data. The distance with error estimates in parentheses is listed in column 5 of Table III. The E_o values with error estimates in parentheses are listed in column 8 of Table V-IV.

Quantitative Results for Rubidium Ammonia Solutions

As mentioned above, Tables V-III and V-IV contain the quantitative results of the single shell fits done on all the Rb-N first shells.

Table V-III is a comparison of the distance results with the two

EXAFS fits reported in columns 4 and 5. Since the fit of column 5 is done with the amplitude function removed, they were not affected by inaccuracies in the theoretical amplitude function. Furthermore, they were minimally affected by multiple distances within the same shell, since the amplitude removal also eliminated the beating between shells. Column 5 therefore contains the best ertimate of the average distance and error in the distance. Tables V-III and V-IV contain the results from all the one shell fits on RbN_3 which gave a reasonable distance of 3.20 Å, close to the correct average of the first two nitrogen shells. A 3-shell fit on RbN_3 will be presented later. In addition, the results of a short range fit on sample F, which was an abbreviated scan, and a similar short range fit on sample G are listed in Tables V-III and V-IV for comparative purposes.

Except for sample G, the Rb-N coordination distance is about 3.10 Å. The distance for the most concentrated (C = 13 MPM) sample G, is 3.071 ± 0.006 Å. The error bars for samples E, G and H are small enough that this difference is statistically significant. The error ellipses of samples E, G and H are plotted for comparative purposes in Figure V-26. The other samples are not included in this figure since the signal-to-noise ratios of these files were poor enough that the error bars were large. The difference in distance between sample G and the average distances of samples G and H is 0.028 ± 0.010 Å. This difference is statistically significant as indicated by Figure V-26.

The E_o values in columns 7 and 8 of Table IV are virtually identical for each fit. Therefore, no information can be obtained from these numbers. The thermal motion term in column 6 is large in magnitude as one would expect. The amplitude term, A, in column 5 was multiplied by R^2 from Table V-I and normalized so that the first shell nitrogen distance of the 3-shell RbN_3 fit contained in Table V-V had a coordination number equal to 8. An estimate of the coordination number, N, is listed in column 4 of Table V-IV.

Sample D is known to have been an inhomogeneous sample. Therefore these coordination numbers should not be interpreted since any slight inhomogeneity in the sample affects the EXAFS amplitude dramatically. Five percent pinholes in a sample would reduce the EXAFS amplitude to 77 percent of its true value (10).

The estimated coordination numbers of samples F and G are both about 15% larger than the estimated coordination numbers of samples E and H. As discussed in Section A, sample G is on the phase separation boundary while sample F is in the phase separation region. This may be the reason for this coordination number difference.

Three Shell Fit on RbN_3

The data file for RbN_3 was prepared in the same manner described above for the $RbNH_3$ samples. The Fourier Transform of this file is shown in Figure V-27. The poor resolution of the EXAFS peaks is caused by thermal motion in the sample. These 3 peaks are not well separated and any resulting fit will not be very accurate. The fit

was done to show that the fitting procedure and the theoretical model were producing answers where were roughly correct for $RbNH_3$ solutions. The results for Rb-N distances in these solutions can be considered very accurate even if the RbN_3 results are poor since the theoretical model has proven accurate in the Arsenic fluorine compounds studied in Chapter IV and other systems (9,11).

The starting parameters for distance were chosen by adding 0.6 Å to the positions of the 3 peaks in the Fourier Transform of Figure V-27. Neither a two shell fit with two nitrogens for scattering nor a three shell fit with three nitrogens matched the data. The results of the three shell fit with two nitrogens and one rubidium are listed in Table V-V. Figure V-26 is a plot of $\chi(k) * k^3$ and the fit $F(k) * k^3$ overplotted. Note that although the fit is not excellent, the major features in the data are synthesized by the fit.

As Table V-V shows, the distances for all three shells which were fit are within 0.1 Å of the crystal structure results (12). The number of scatterers, N, which is estimated from the amplitude of the fit is close to correct for peak 2 but very much smaller than one would expect for peak 3. This is not entirely unanticipated. The large thermal motion terms which are evident in both k- and R-space data decrease the intensity of Rb backscattering more than N. This is due to the fact that Rubidium scatters less efficiently at low values of k than does nitrogen. By the time the scattering function of Rb has become large, the large thermal motion terms have damped

the EXAFS observed to a small value.

Since a three shell fit on such low resolution data would not be expected to be accurate, one would not expect the EXAFS results to be in excellent agreement with X-Ray crystal data. The data in Table V-V show, however, that the fitting procedure used produced results with reasonable distances. Therefore, the theoretical EXAFS calculations provided reasonable answers for $RbNH_3$ solutions.

D. Conclusions

Figures V-4 and V-5 indicate what range of sample concentrations and temperature values were studied. In addition to the temperatures indicated in Figure V-5, XAES scans of samples E, F and G were obtained at T = 228 K. XAES data were obtained at all these positions. EXAFS data were obtained at the positions indicated by letters E, F G and H in Figure V-5 and at T = 263, 242 and 217 K for sample D. The variety of samples studied is representative of the different portions of the phase transition region. As the first XAS experiment performed on ammonia solutions, this sampling provided a basis for a feasibility study of XAS experiments on metal-ammonia solutions.

The density, D_M, of the metal atom Rb was measured for these samples from the XAS data. The measured data in Tables V-I, II and Figures V-12, 13, 14 are consistent with reported measurements of the density of the overall solution (6,7). With the improved experimental design used for samples E, F, G and H, the measurement of $D_M(T)$ illustrated in Figures V-12 and V-13 could be repeated

with greater precision. A measurement of density for both the metal and the overall solution on the same samples would provide a measure of the volume of the metal atom. This would provide more information about the nature of the metal-insulator transition.

Figure V-14 shows proof that the data collected for sample F at T = 197 K were a measurement of the metallic phase in a phase separated sample. The 25% decrease in D_M as T was decreased is explained by this fact. Since the metallic phase is lighter (7) and the density at 197 K is dramatically less than at 228 K, the metallic phase was investigated. This explains why the features of sample F at 197 K are similar to the features of the metallic sample E and not of the other insulating samples.

Figure V-9 shows the second derivative spectra of samples E, F, G and H. In addition to the major transition peak at 15199 eV, smaller transitions which appear as shoulders are evident in these spectra between 15190 and 15196 eV. The position and intensity of these transitions are different in these spectra. The trends in these differences correlate with the estimated conductivity of the samples.

Table V-VI provides a summary of the peak height and edge width data which are plotted in Figures V-15 and V-16. For the higher conductivity samples, the peak height was less than for the lower conductivity samples and the edge width was greater than for the lower conductivity samples. The decrease in intensity of the major p-transition as the conductivity increases

accounts for both of these phenomena.

The main absorption peak is largest when the sample has low conductivity and it is therefore indicative of the insulating phase in which the Rb^+ ion is not screened by the localized solvated electrons. As the sample parameters (T and C) are changed so that the solvated electron mean free path increases, the conductivity increases. Increasing electron delocalization causes this change. This delocalization causes a mixing of the solvated electron states with the Rb^+ states so that these states are no longer localized and discrete. This broadening of the empty orbitals into bands causes the peak height (H_P) to decrease. For the same reason, the edge width, Δ_P, increases.

The edge position, E_I, plotted in Figure V-11, is another indication of the correlation of the edge features with the conductivity and electron delocalization. Figure V-3a demonstrates that the conductivity will increase for sample D in this temperature range as T is increased. As the conductivity increased, E_I shifted to a higher energy. This was consistent with the observation above, that the small shoulder peak shown in Figure V-5 shifted to higher energy with increasing conductivity.

Therefore, as the delocalization of the solvated electron was increased, the main transition peak P decreased in intensity and broadened while the small shoulder shifted to higher energy. The edge spectra is a sum of these transitions and the arctangent-shaped onset of the continuum (5). As the sample became more metallic, the onset of the absorption occurred at the Fermi level

of the metal. The small shoulder was probably caused by the Fermi level, since the shoulder was most apparent in the spectra of higher conductivity samples.

The major result of the EXAFS measurements presented in Tables V-III and V-IV is that the average distance of the first shell Rb-N distance is between 3.07 and 3.10 Å. This is the first measurement of the metal-nitrogen distance in any metal-ammonia solution. All of the samples (except E) had a measured bond distance consistent with R = 3.10 ± 0.01 Å. The most concentrated sample (E) had a shorter measured distance of R = 3.07 ± 0.01 Å. Figure V-26 is a plot of the error contours which indicates that this difference is statistically significant. The Rb-N bond distance appears to decrease as the radius and delocalization of the solvated electron increase.

Finally, the measured number of scatterers (listed in Table V-IV) is 15% larger for samples F and G than for the other samples E and H. Since samples F and G are located in the region of phase separation as indicated in Figure V-5, the phase separation must involve an increase in the number of nitrogen atoms bonded to the Rb atom.

These experiments provided a measure of the XAS features of $RbNH_3$. Changes in the features which are consistent with the known properties of $RbNH_3$ were correlated with conductivity and delocalization of the solvated electrons. In the XAES region, intensity and position changes of absorption transitions were explained. In the EXAFS region, the Rb-N bond distance and the relative number of nitrogen atoms in the first shell were measured. XAS has been

shown to provide unique information about the nature of the metal-ammonia phase separation, phase transition, and density fluctuations.

Table V-I

$RBNH_3$ XAES RESULTS

Sample/ Run	C(MPM)	T (K)*	N§	D_M* (gm/cm^3)	H_p*	$\Delta_p=E_o-E_i$* (eV)
C/1	6	203 to 247	13	0.1914 (26)	1.281 (7)	5.79 (3)
C/2†	[illegible]	248 to 278	7	0.1871 (95)	1.194 (49)†	6.09 (23)†
D/1	7	202 to 233	7	0.2299 (36)	1.293 (8)	5.79 (4)
D/2†	7	232 to 284	8	0.2247 (86)	1.140 (15)†	6.45 (14)†
D/3†	7	263 (1)	7	0.2230 (16)	1.146 (6)†	6.03 (3)†
		242 (1)	3	0.2296 (12)	1.144 (1)†	5.99 (5)†
		217 (1)	1	0.2359	1.139†	5.98†
E	13	228 (1)	4	0.4206 (32)	1.211 (9)	5.92 (6)
		199 (2)	9	0.4299 (39)	1.231 (15)	5.66 (16)
F	3.4	228 (1)	4	0.1165 (3)	1.301 (1)	5.42 (1)
		197 (1)	4	0.0866 (4)	1.244 (2)	5.78 (3)
G	2.7	228 (1)	4	0.0941 (3)	1.297 (3)	5.39 (2)
		197 (1)	8	0.0964 (7)	1.303 (4)	5.24 (6)
H	0.5	197 (1)	8	0.0180 (1)	1.303 (2)	5.39 (3)

* The estimate of the error in the last place is enclosed in parentheses.

† The data for these samples were obtained using a monochromator with a poorer resolution. H_p and Δ_p cannot be compared with the other data.

§ N is the number of measurements of each quantity whose mean and standard deviation were calculated to obtain each datum and its error estimate.

Table V-II

FITTING RESULTS OF DENSITY VERSUS TEMPERATURE

$$\log_{10}(D_m) = a_2(1/T)^2 + a_1(1/T) + a_o$$

Sample	C (MPM)	N †	$a_2(\times 10^{-})$ *	$a_1(\times 10^{-2})$ *	a_o *
D	7	29	-2.8 (9)	2.6 (7)	-1.22 (15)
C	6	20	-3.9 (17)	2.7 (14)	-1.34 (30)

* The estimate of the error in the last place is enclosed in parentheses.

† N is the number of measurements of D_M mole which were used in the fit.

Table V-III

RADIAL DISTANCE RESULTS OF ONE SHELL FITS

Sample	C (MPM)	T (K)	Fit with $e^{\sigma k^2}$ R(Å) *	Fit with Amplitude Removed R(Å) *
$RbNH_3$				
D/3 †	7	263	3.09 (5)	3.086 (28)
		243	3.10 (9)	3.100 (17)
		217	3.09 (7)	3.108 (46)
E †	13	200	3.07 (3)	3.071 (6)
G †	2.7	197	3.10 (3)	3.101 (12)
H †	0.5	197	3.10 (3)	3.096 (10)
RbN_3 †	---	295	3.20 (21)	-----
$RbNH_3$				
F §	3.4	197	3.23 (17)	3.09 (7)
G §	2.7	197	3.12 (14)	3.13 (5)

* The estimate of the error in the last place is enclosed in parentheses.

† The data were fit over the range of k = 3.8 to 9 1/Å

§ The data were fit over the range of k = 3.8 to 6 1/Å.

Table V-IV

EXAFS FITTING PARAMETERS OF ONE SHELL FITS

Sample	C (MPM)	T(K)	N†	Fit with $e^{\sigma k^2}$ A	σ(Å)	E_o-15000eV*	Fit with Amplitude Removed E_o-15000eV*
$RbNH_3$							
D/3 [α]	7	263	2.8	.053	-.022	206 (4)	206 (2)
		243	4.0	.075	-.023	203 (3)	204 (2)
		217	5.2	.097	-.038	203 (6)	204 (3)
E [α]	13	200	5.6	.106	-.032	205 (3)	205 (1)
G [α]	2.6	197	6.6	.123	-.036	206 (3)	206 (1)
H [α]	0.5	197	5.7	.107	-.036	206 (3)	206 (1)
RbN_3 [α]	---	295	16.9	.297	-.107	203 (21)	---
$RbNH_3$							
F [β]	3.4	197	13.3 [6.4]‡	.251	-.074	209 (11)	207 (6)
G [β]	2.7	297	13.7 [6.6]‡	.252	-.069	209 (9)	209 (6)

* The estimate of the error in the last place is enclosed in parentheses.

† For EXAFS, A_i should be proportional to N_i/R_i^2. The value of N is normalized so that N = 8 for peak 1 in the 3-shell fit of RbN_3. See the text and Table V-V for further explanation.

‡ These two values are corrected values. The value of N in brackets was normalized so that sample G with the short-k-range analysis gave the same N as the long k-range analysis.

Footnotes for Table V-IV, continued

α The k-range used was k = 3.8 to 9.0 1/Å.

β The k-range used was k = 3.8 to 6.0 1/Å.

Table V-V

EXAFS FITTING RESULTS FOR RbN_3

EXAFS Results: A Three Shell Fit on RbN_3 *

	Peak 1	Peak 2	Peak 3
Atom Type	N	N	Rb
σ_i ($Å^2$)	-0.0674	-0.0522	+0.0047
A_i †	0.1495	0.0779	0.001452
$N_i = \frac{A_i R_i^2}{A_1 R_1^2} * 8$ †	8 †	6.2	0.12
R_i (Å)	3.01	3.78	3.85

Crystal Structure Results §

	Radial Distance				
	1	2	3	4	5
Atom Type	N	N	Rb	N	Rb
N_i	8	8	2	2	4
R_i (Å) ‡	3.10 (3)	3.67 (3)	3.76 (1)	4.07 (3)	4.46 (2)

* The k-range used was k = 3.8 to 9.0 1/Å and E_o= 15206 eV.

† For EXAFS, A should be proportional to N_i/R_i^2. The value of N is normalized so that N_1 = 8 for peak 1.

§ See Reference 12.

‡ The estimate of the error in the last place is enclosed in parentheses.

Table V-VI

CORRELATION OF PEAK HEIGHT AND
EDGE WIDTH WITH CONDUCTIVITY

Conductivity, σ	HIGH	LOW
Peak Height, H_p †	1.21 to 1.24	1.30
Edge Width, Δ_p (eV) †	5.7 to 5.9	5.2 to 5.4
Samples	E, F(197K)	G, H, F(228)

* The conductivity estimates were made from the conductivity and phase separation data in Figures V-4 and 5.

† The values of H_p and Δ_p listed in this table cover the range of values listed in Table VI for samples E, F, G and H.

Figure Captions
Chapter V

V-1 Sample dewar and sample cells used for $Rb-NH_3$ experiments.

V-2 $1/\mu$ (inverse of absorption coefficient as a function of $R = [NH_3]/[M]$ for metal-ammonia solutions and for pyrex glass as a function of Z.

V-3 Conductivity as function of temperature for $Rb-NH_3$ solutions with (a) C = 7 MPM and (b) C = 5 MPM. Note that EXAFS sample D has a concentration of 7 MPM.

V-4 Conductivity as a function of concentration for several different metal-ammonia solutions. The diamonds and circles are $Rb-NH_3$ data. The letters indicate the concentration of the samples which were used for XAS measurements.

V-5 Phase separation diagram (solid line) and its measured points (triangles). The letters and arrows indicate the concentration and temperature at which XAS experiments were performed.

V-6 Rb K-shell absorbance of a representative $RbNH_3$ sample.

V-7 Normalized K-shell absorbance of a representative $RbNH_3$ sample.

V-8 Normalized K-shell absorbance and its first and second derivatives for a representative $RbNH_3$ sample.

V-9 Second derivative of the normalized K-shell absorbance for samples E, F, G and H at high temperature (T) and low temperature (T').

V-10 Second derivative of the normalized K-shell absorbance for sample D at three different temperatures.

V-11 The major inflection point, E_I, as a function of temperature for sample D.

V-12 $Log_{10}(D_M)$ of $RbNH_3$ solutions as a function of 1/T data (diamonds) for sample D with the fit (solid line) of Table V-II are plotted.

V-13 $Log_{10}(D_M)$ of $RbNH_3$ solutions as a function of 1/T data (diamonds) for sample C with the fit (solid line) of Table V-II are plotted.

V-14 Change in D_M for $RbNH_3$ solutions as a function of temperature. For each sample, its highest temperature run was defined as 0.0%.

V-15 Peak Height, H_P, of $RbNH_3$ solutions as a function of temperature.

V-16 Edge Width, Δ_P, as a function of temperature for $RbNH_3$ solutions.

V-17 Normalized K-shell absorption of a $RbNH_3$ sample with the first post-edge background strip overplotted.

V-18 Data (dots) and background strip (line) for a representative $RbNH_3$ data file. The EXAFS was fit simultaneously with the background and one EXAFS shell.

V-19 Data (dots) and fit (line) for the fit which included background stripping. See Figure V-18.

V-20 $k^2\chi(k)$ plot of EXAFS data for six $RbNH_3$ samples.

V-21 $|\phi_3(R)|$ plot of six $RbNH_3$ samples.

V-22 $k^3\chi(k)$ plot of $RbNH_3$ EXAFS data (dots) and the fit (solid line) with the Debeye Waller term, σ, included.

V-23 Error contour plot for the fit in Figure V-22. The contour for a 100% increase in error is drawn.

V-24 $k^{-3}\chi_T(k)$ plot of $RbNH_3$ EXAFS data (dots) and the fit (solid line). $\chi_T(k)$ is the EXAFS data with both the complete amplitude and theoretical phase function removed.

V-25 Error contour plot for the fit in Figure V-24. The contours for 100%, and 1000%, increase in error are drawn.

V-26 100% increase amplitude removed error contour plots for three high signal-to-noise Rb-NH_3 samples. The center of the contour is the best fit value and the contour provides an

estimate of the reliability of the data.

V-27 $|\phi_3(R)|$ and $|\phi_1(R)|$ plots of EXAFS data for $RbNH_3$.

V-28 $k^3\chi(k)$ plot of the filtered data (dots) between 0.5 Å and 4.0 Å and fit (solid line) with the Debeye Waller term, σ, included. The fit was done using three scattering shells N, N and Rb.

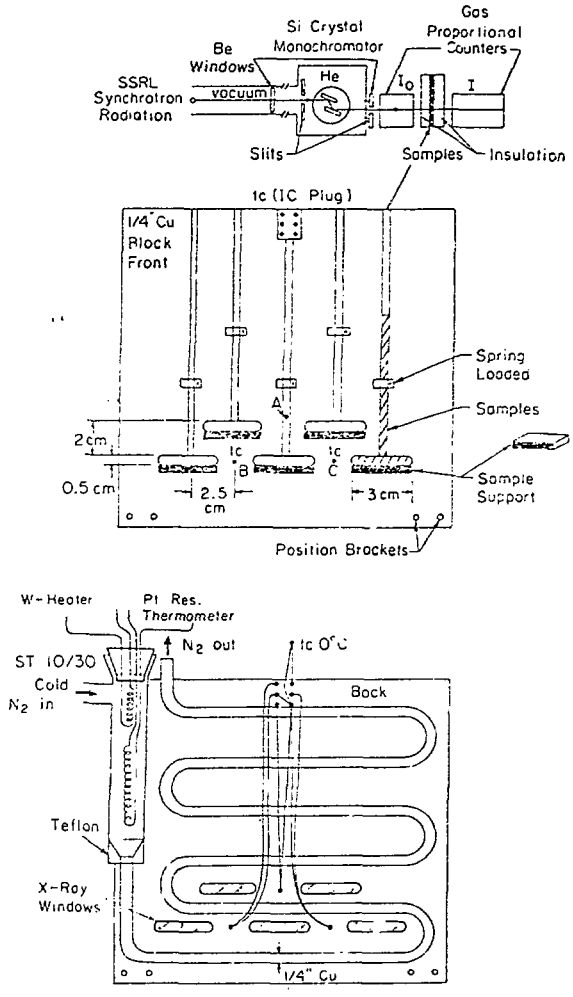
Gas
Proportional
Counters
Si Crystal
Monochromator
Be
Windows
He
SSRL
Synchrotron
Radiation
vacuum
I_0
I
Slits
Samples
Insulation
tc (TC Plug)
1/4" Cu
Block
Front
Spring
Loaded
Samples
A
2cm
tc
B
tc
C
0.5 cm
2.5
cm
3cm
Sample
Support
Position Brackets
W-Heater
Pt Res.
Thermometer
N_2 out
tc 0°C
ST 10/30
Cold
N_2 in
Back
Teflon
X-Ray
Windows
1/4" Cu

Figure V-1

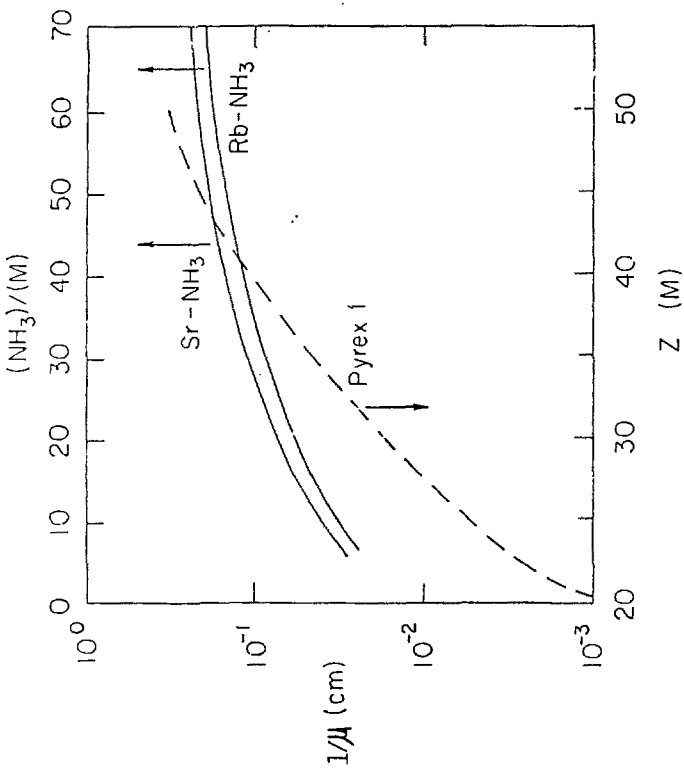
(NH3)/(M)
0
10
20
30
40
50
60
70
Sr-NH3
Rb-NH3
Pyrex I
1/μ (cm)
10^0
10^-1
10^-2
10^-3
Z (M)
20
30
40
50

Figure V-2

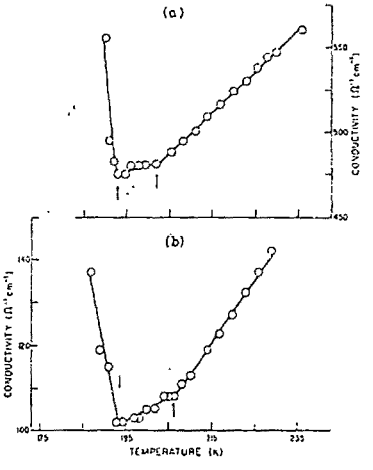
(a)
CONDUCTIVITY (Ω⁻¹cm⁻¹)
350
300
250
(b)
CONDUCTIVITY (Ω⁻¹cm⁻¹)
140
120
100
175
195
215
235
TEMPERATURE (K)

Figure V-3

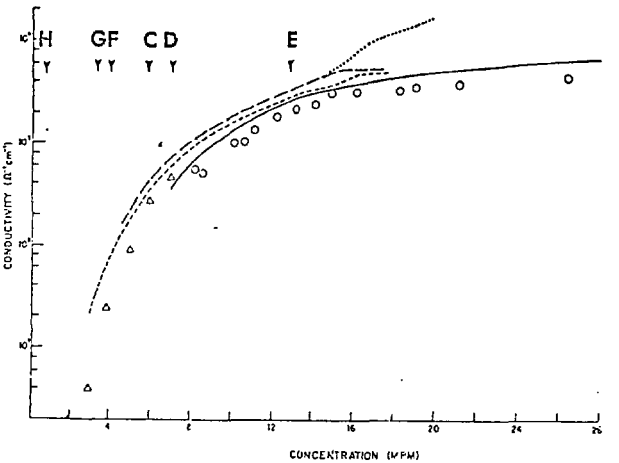

Figure V-4

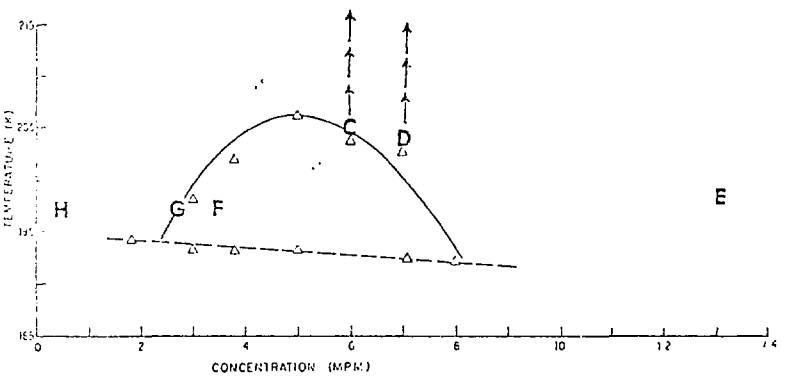

Figure V-5

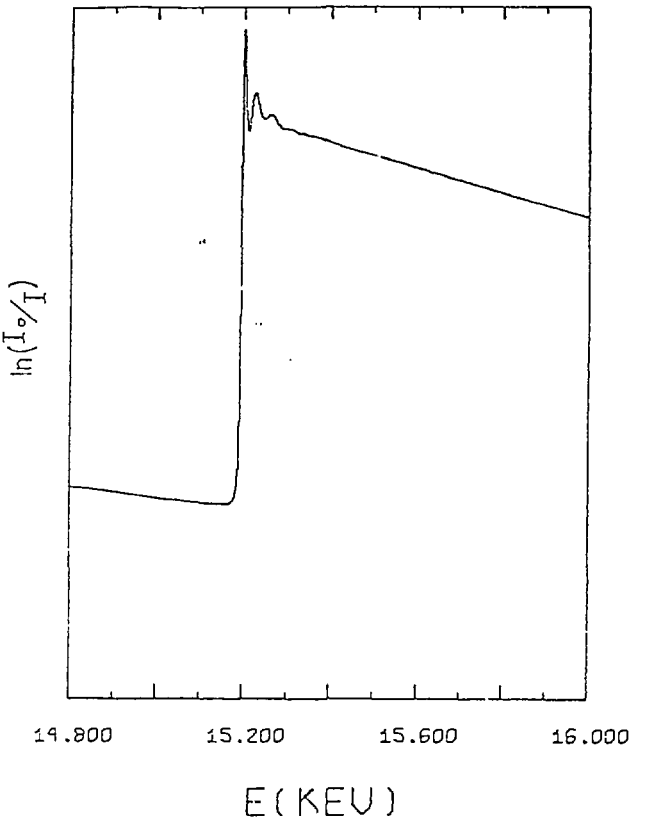

Figure V-6

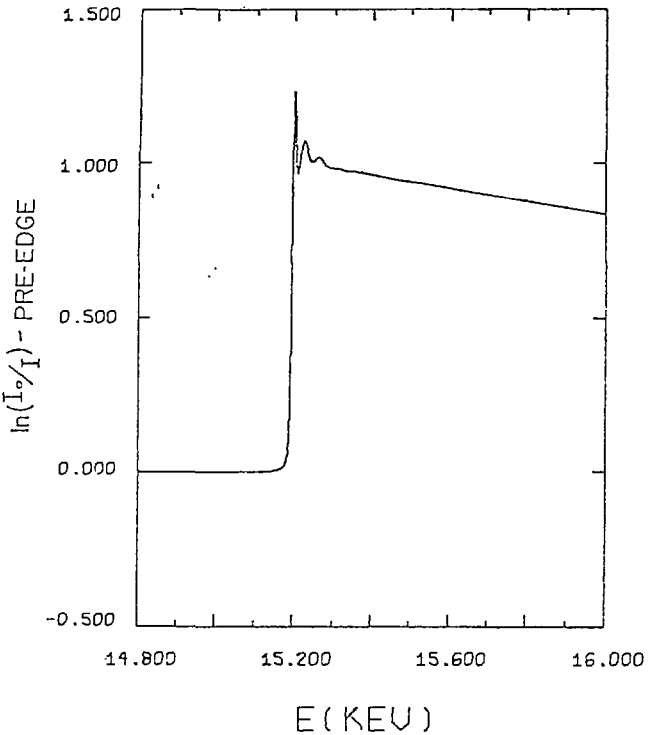
1.500
1.000
0.500
0.000
-0.500
ln(I°/I) - PRE-EDGE
14.800
15.200
15.600
16.000
E(KEV)

Figure V-7

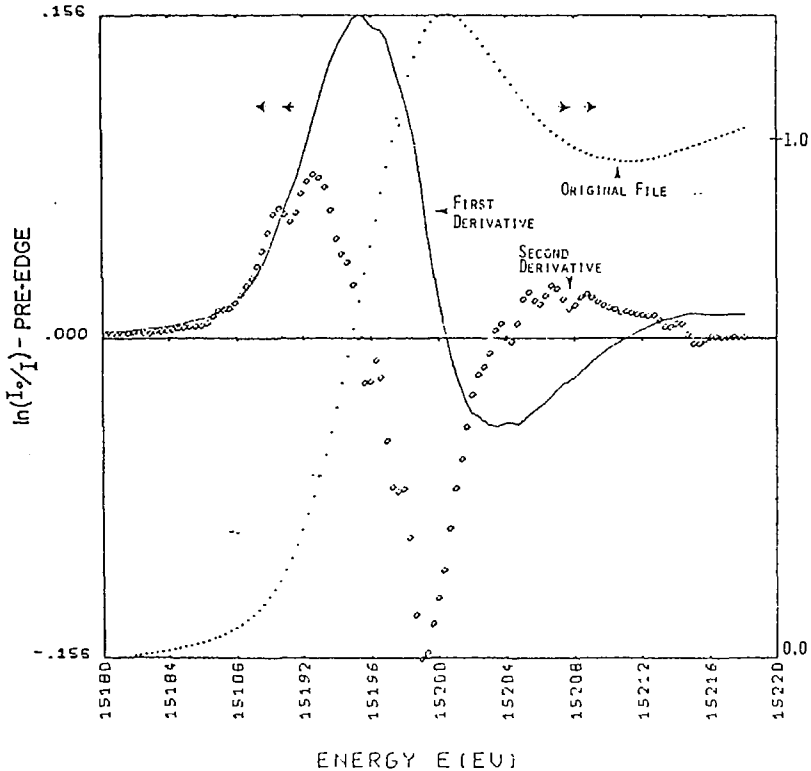
.156
.000
-.156
1.0
0.0
ln(Io/I) - PRE-EDGE
ORIGINAL FILE
FIRST DERIVATIVE
SECOND DERIVATIVE
15180
15184
15188
15192
15196
15200
15204
15208
15212
15216
15220
ENERGY E(EV)

Figure V-8

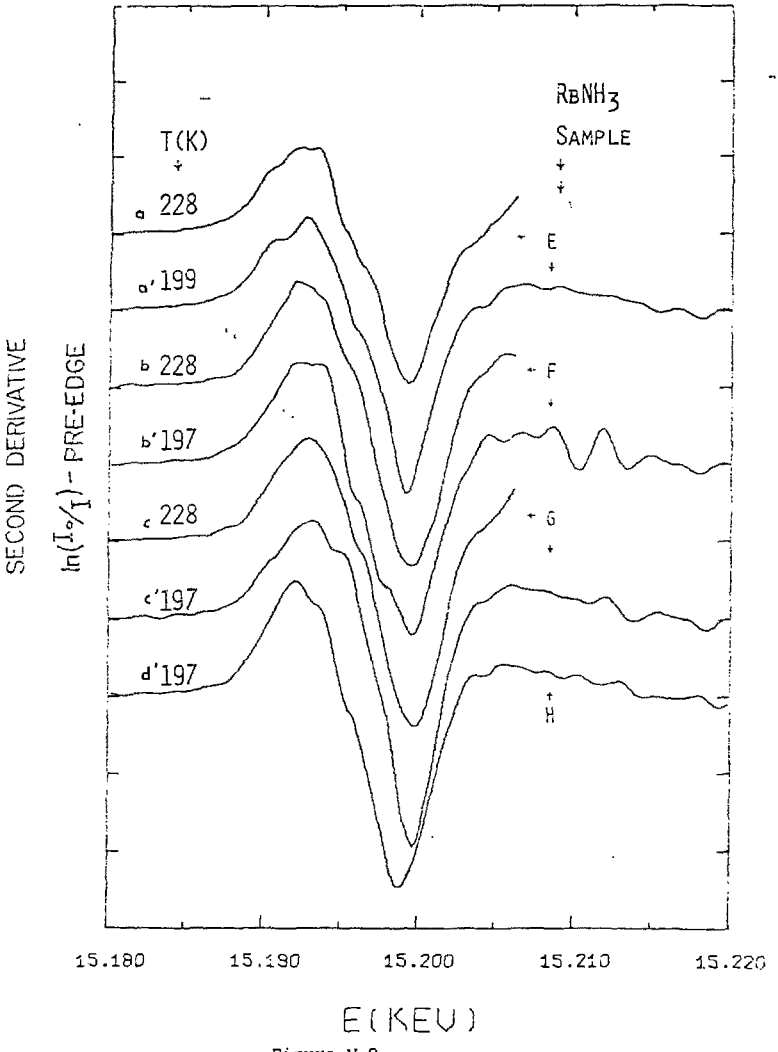
RbNH3
SAMPLE
T(K)
a 228
a' 199
b 228
b' 197
c 228
c' 197
d' 197
E
F
G
H
SECOND DERIVATIVE
ln(I0/I) - PRE-EDGE
15.180
15.190
15.200
15.210
15.220
E(KEV)

Figure V-9

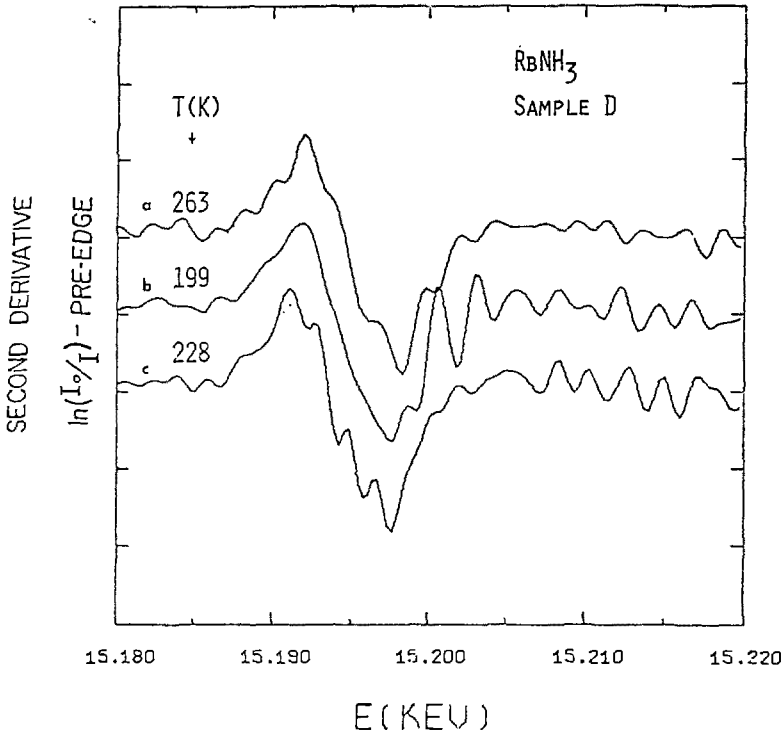
RBNH3
SAMPLE D
T(K)
a 263
b 199
c 228
SECOND DERIVATIVE
ln(Io/I) - PRE-EDGE
15.180
15.190
15.200
15.210
15.220
E(KEV)

Figure V-10

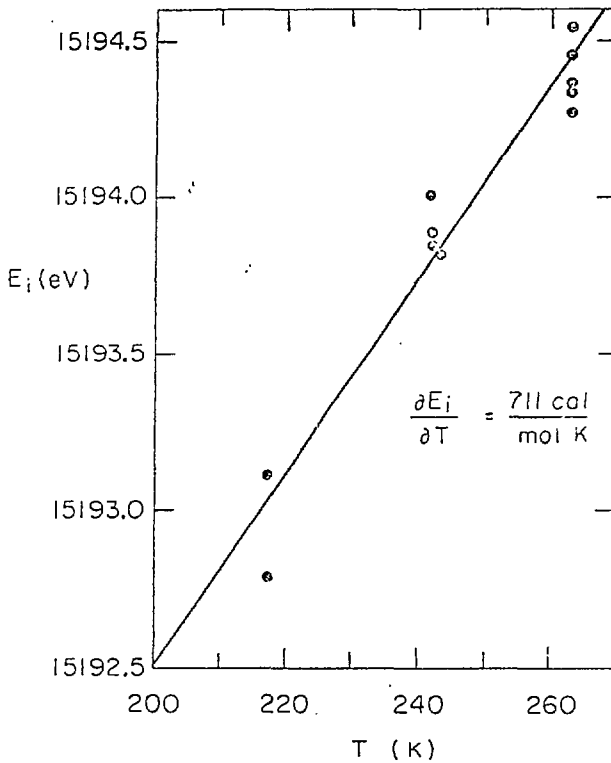
15194.5
15194.0
15193.5
15193.0
15192.5
E_i (eV)
$\frac{\partial E_i}{\partial T} = \frac{711\ cal}{mol\ K}$
200
220
240
260
T (K)

Figure V-11

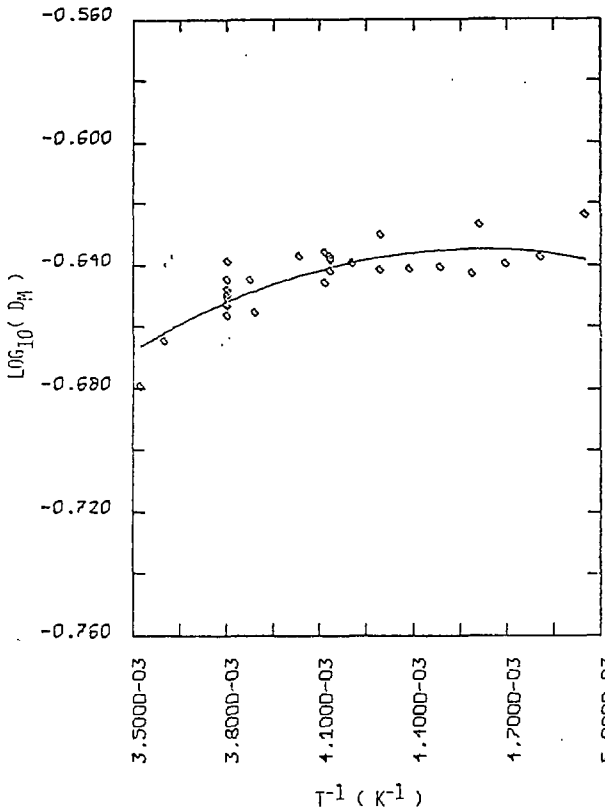
-0.560
-0.600
-0.640
-0.680
-0.720
-0.760
LOG10(DM)
3.5000-03
3.8000-03
4.1000-03
4.1000-03
4.7000-03
5.0000-03
T-1 (K-1)

Figure V-12

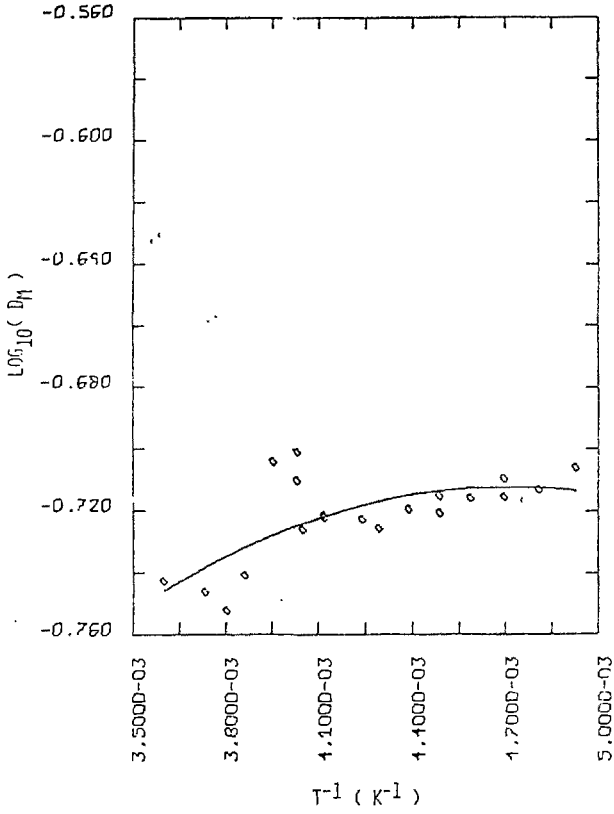
-0.560
-0.600
-0.640
-0.680
-0.720
-0.760
LOG10(DM)
3.5000-03
3.8000-03
4.1000-03
4.4000-03
4.7000-03
5.0000-03
T-1 (K-1)

Figure V-13

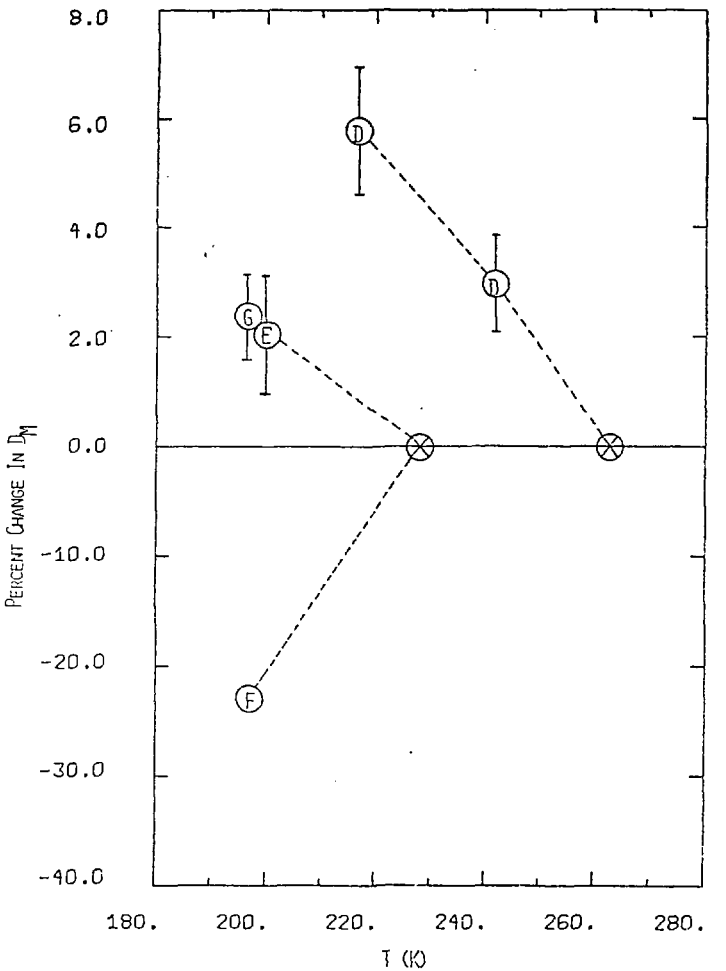
8.0
6.0
4.0
2.0
0.0
-10.0
-20.0
-30.0
-40.0
PERCENT CHANGE IN D_M
180.
200.
220.
240.
260.
280.
T (K)
D
D
G
E
F

Figure V-14

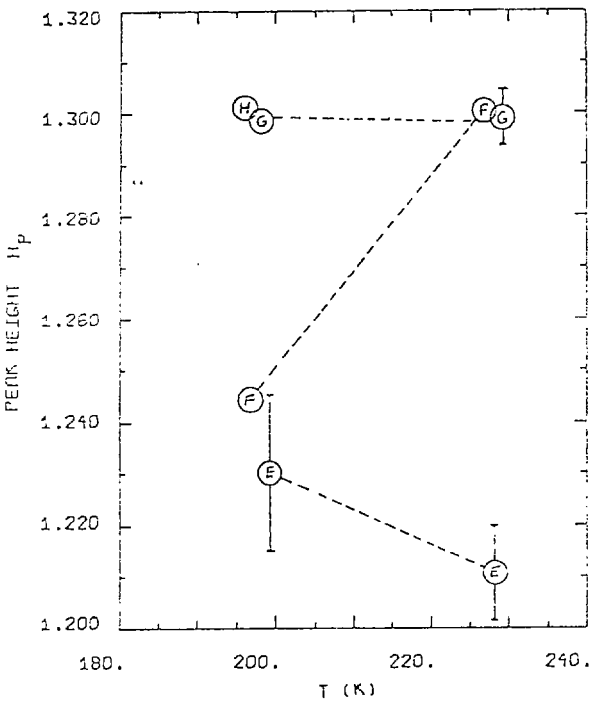
1.320
1.300
1.280
1.260
1.240
1.220
1.200
PEAK HEIGHT H_p
180.
200.
220.
240.
T (K)
H
G
F
G
F
E
E

Figure V-15

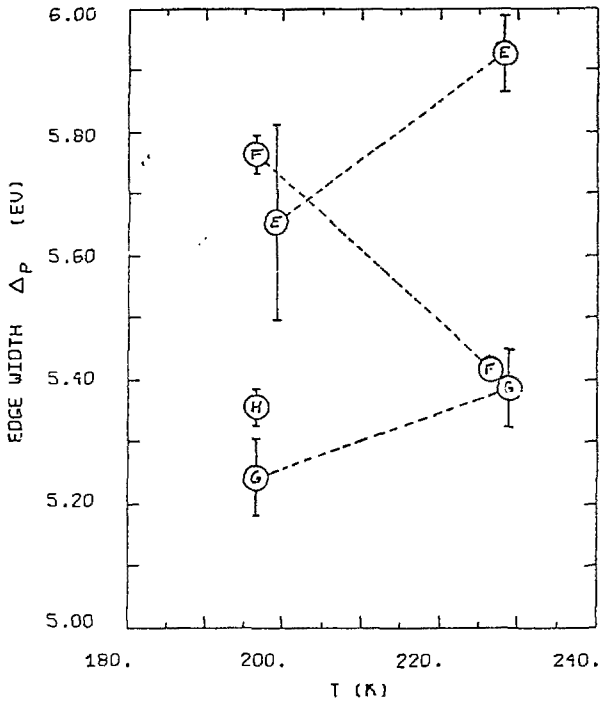
6.00
5.80
5.60
5.40
5.20
5.00
EDGE WIDTH Δ_P (EV)
180.
200.
220.
240.
T (K)
E
F
E
F
G
H
G

Figure V-16

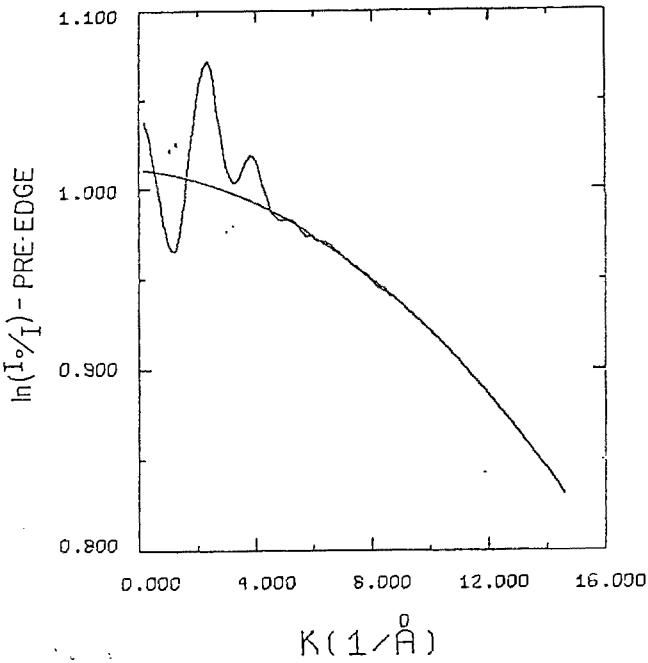
1.100
1.000
0.900
0.800
ln(Io/I) - PRE-EDGE
0.000
4.000
8.000
12.000
16.000
K(1/Å)

Figure V-17

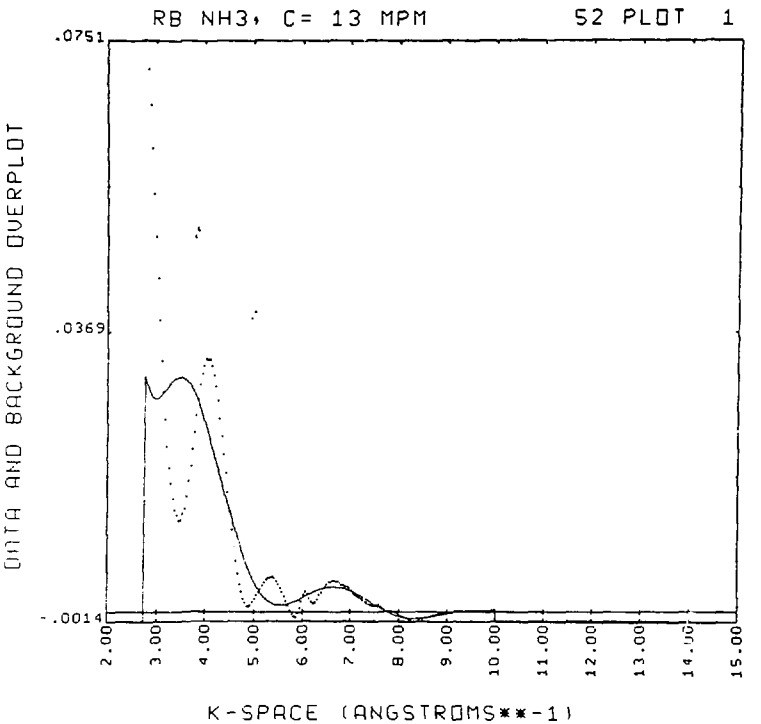

XBL 798-10748

Figure V-18

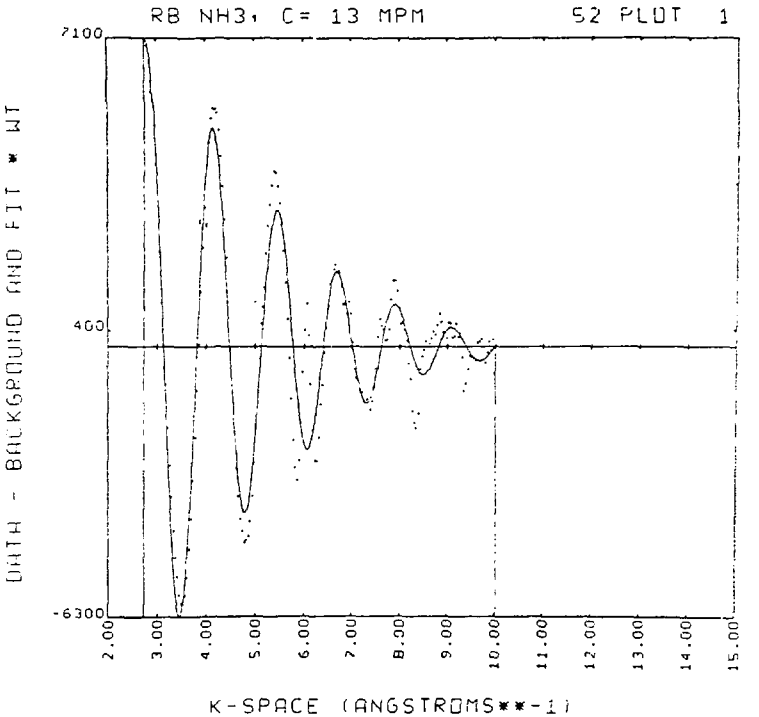

XBL 798-10749

Figure V-19

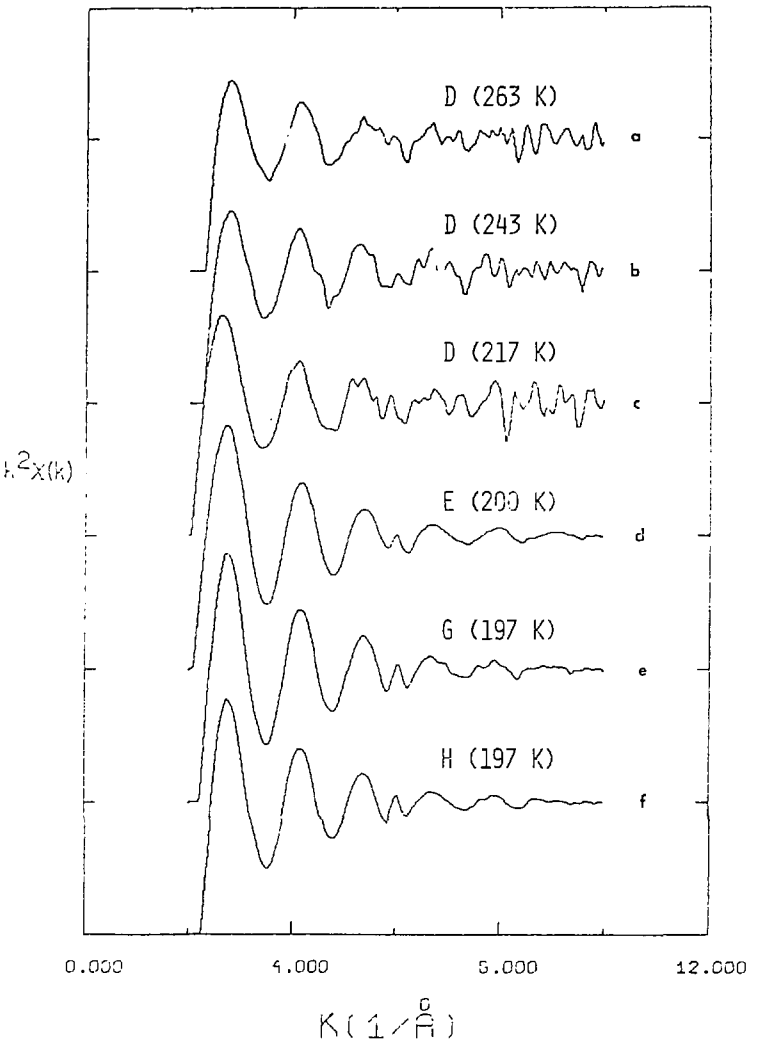
D (263 K)
a
D (243 K)
b
D (217 K)
c
E (200 K)
d
G (197 K)
e
H (197 K)
f
k²χ(k)
0.000
4.000
8.000
12.000
K(1/Å)

Figure V-20

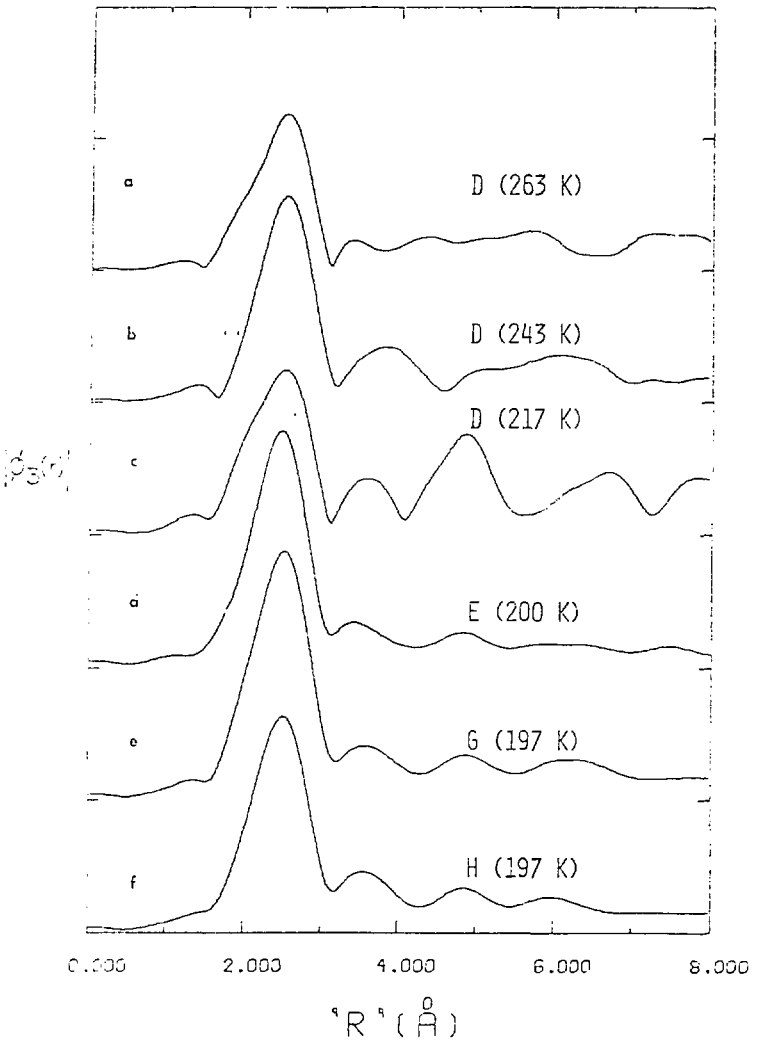
a
D (263 K)
b
D (243 K)
c
D (217 K)
d
E (200 K)
e
G (197 K)
f
H (197 K)
0.000
2.000
4.000
6.000
8.000
"R" (Å)

Figure V-21

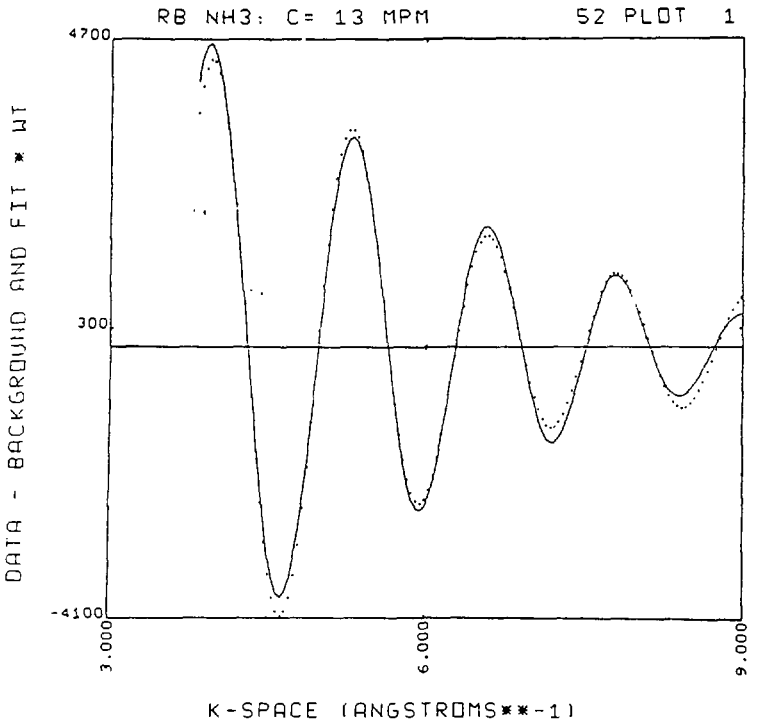

XBL 798-10750

Figure V-22

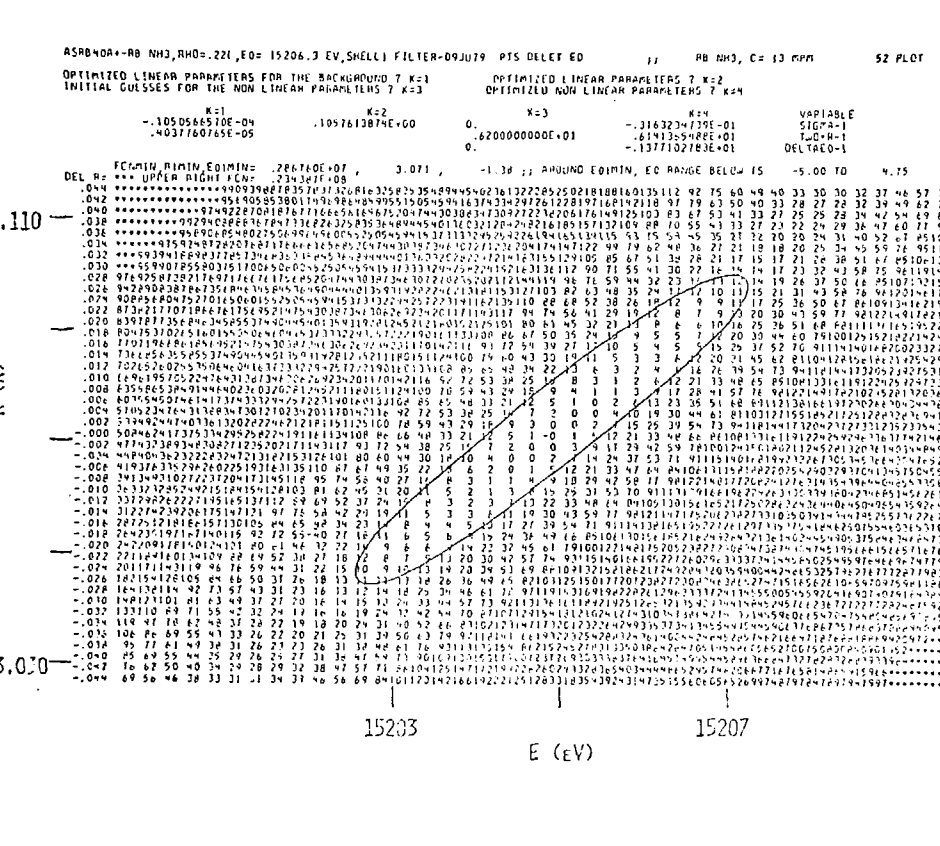
ASR940A-RB NH3,RHO=.221,E0= 15206.3 EV,SHELL1 FILTER-09JU79 PTS DELET ED
RB NH3, C= 13 DPM
52 PLOT 1
OPTIMIZED LINEAR PARAMETERS FOR THE BACKGROUND 7 K=1
INITIAL GUESSES FOR THE NON LINEAR PARAMETERS 7 K=3
OPTIMIZED LINEAR PARAMETERS 7 K=2
OPTIMIZED NON LINEAR PARAMETERS 7 K=4
K=1
K=2
K=3
K=4
VARIABLE
SIGMA-1
DELTAE0-1
3.110
3.000
R (A)
E (EV)
15203
15207

Figure V-23

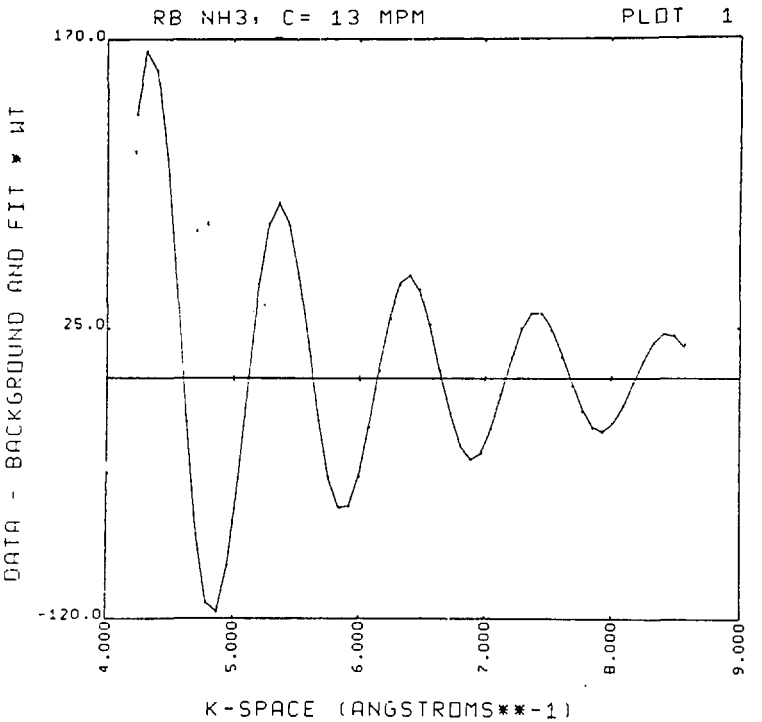

XBL 797-10746

Figure V-24

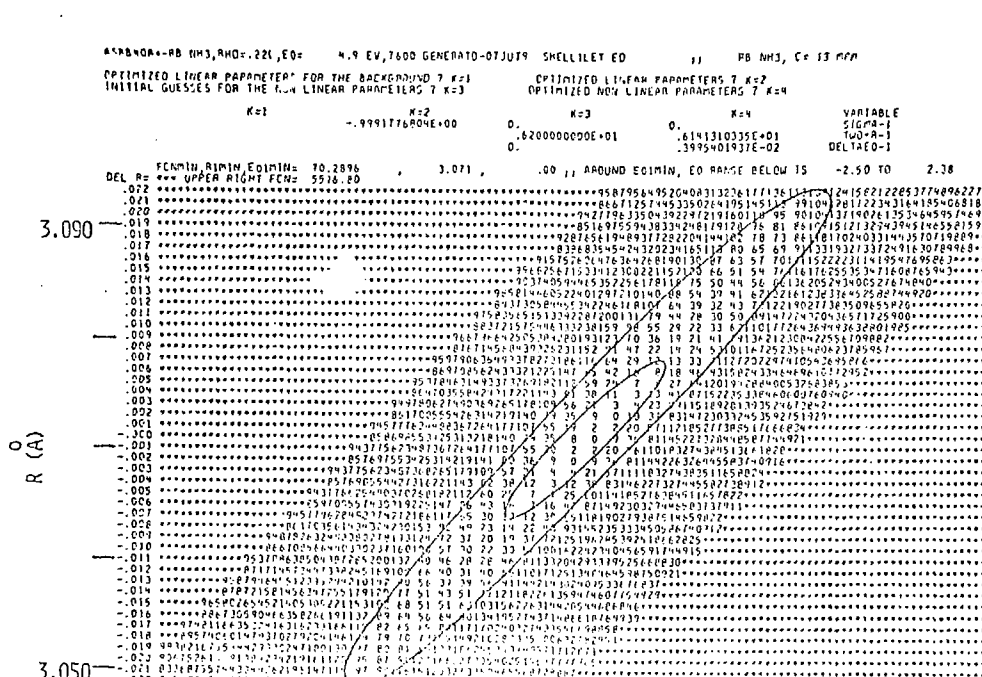
OPTIMIZED LINEAR PARAMETERS FOR THE BACKGROUND 7 K=1
INITIAL GUESSES FOR THE NON LINEAR PARAMETERS 7 K=3
OPTIMIZED LINEAR PARAMETERS 7 K=2
OPTIMIZED NON LINEAR PARAMETERS 7 K=4
K=1
K=2
K=3
K=4
VARIABLE
SIGMA-1
TAU-A-1
DELTAEO-1
FCNMIN,RIMIN,EDIMIN= 70.2896
3.071
.00
AROUND EDIMIN, EO RANGE BELOW IS -2.50 TO 2.38
DEL R= *** UPPER RIGHT FCN= 5516.80
3.090
3.050
R (A)
15204
15206
E (eV)

Figure V-25

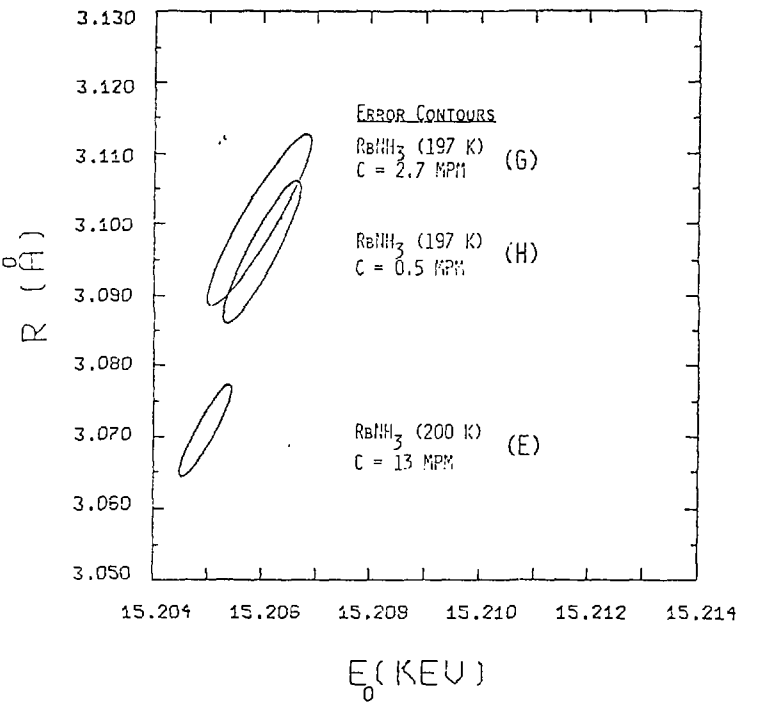
3.130
3.120
3.110
3.100
3.090
3.080
3.070
3.060
3.050
R (Å)
ERROR CONTOURS
RbNH3 (197 K)
C = 2.7 MPM
(G)
RbNH3 (197 K)
C = 0.5 MPM
(H)
RbNH3 (200 K)
C = 13 MPM
(E)
15.204
15.206
15.208
15.210
15.212
15.214
E0 (KEV)

Figure V-26

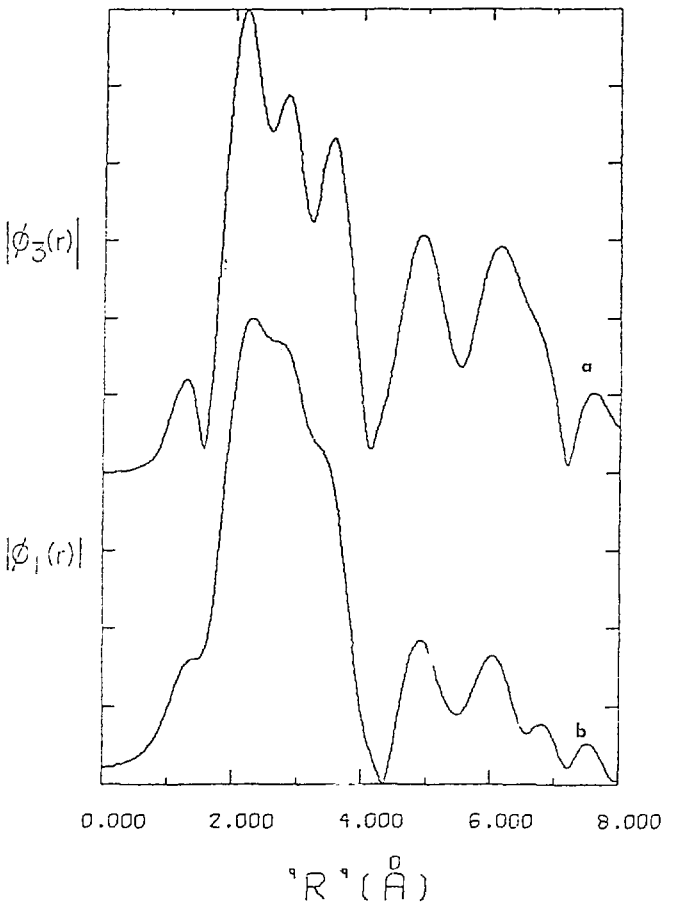

Figure V-27

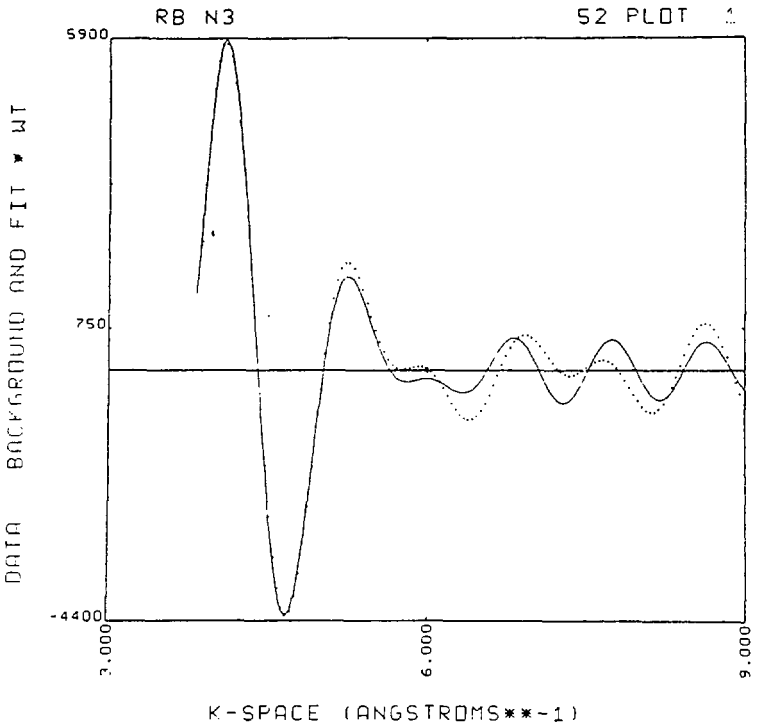

XBL 798-10747

Figure V-28

References
Chapter V

1. J. V. Acrivos and K. S. Pitzer; J. Phys. Chem. (1962) 66, 1693-1698.

2. W. H. McMaster, N. Kerr Del Grande, J. H. Mullet and J. H. Hubbell; Compilation of X-Ray Cross Sections, UCRL-50174, Sec. II Rev. I, Nat'l. Technical Information Service, Springfield, Virginia (1969).

3. A. C. Sharp, et al.; Phys. Rev. A (1971) 4, 414.

4. C. E. Moore; Atomic Energy Levels, Vol. II (1952) National Bureau of Standards (U.S.) Circular 467.

5. L. G. Parratt, Phys. Rev. (1939) 56, 295; F. K. Richtmyer, C. W. Barnes and E. Ramberg, Phys. Rev. (1934) 46, 843.

6. J. C. Thompson; unpublished data.

7. J. C. Thompson; Electrons in Liquid Ammonia, Clarendon Press, Oxford, 1976.

8. E.A. Stern, Steve M. Heald and B. Bunker; Phys Rev. Lett. (1979) 42, 1372-1375.

9. P. K. Teo and P. A. Lee, J. Am. Chem. Soc. (1979) 101, 2815.

10. J. H. Hunter; Ph. D. Thesis, Stanford University (1977).

11. [illegible] Kirby; Ph. D. Thesis, University of California, Berkeley (in preparation).

12. A. M. Muller, Z. anorg. allg. Chem (1972) 392, 159-166.